MATERIALS-AFFECTED MANUFACTURING: SIMULATING THE MICROSTRUCTURE EVOLUTION OF METAL ALLOYS THROUGH PROCESSING

A Dissertation
Presented to
The Academic Faculty

by

Eric Hoar

In Partial Fulfillment
of the Requirements for the Degree
Doctor of Philosophy in the
School of Materials Science and Engineering

Georgia Institute of Technology
August 2020

MATERIALS-AFFECTED MANUFACTURING: SIMULATING THE MICROSTRUCUTRE EVOLUITON OF METAL ALLOYS THROUGH PROCESSING

Approved by:

Dr. Hamid Garmestani, Advisor
School of Materials Science and Engineering
Georgia Institute of Technology

Dr. Steven Liang
George W. Woodruff
School of Mechanical Engineering
Georgia Institute of Technology

Dr. Chaitanya Deo
George W. Woodruff
School of Mechanical Engineering
Georgia Institute of Technology

Dr. Surya Kalidindi
George W. Woodruff
School of Mechanical Engineering
Georgia Institute of Technology

Dr. Naresh Thadhani
School of Materials Science and Engineering
Georgia Institute of Technology

Date Approved: [July 17, 2020]

To My Family and Friends

ACKNOWLEDGEMENTS

I would like to thank my advisor, Hamid Garmestani, who supported my research throughout my time at Georgia Tech. I would also like to thank Dr. Mario Affatigato, Dr. Steve Feller, and Dr. Ugur Akun my undergraduate professors who opened my eyes to the joys of research and encouraged me to explore different research avenues. I also wish to thank Dr. Steven Liang and Dr. Chaitanya Deo who assisted in advising me in my research. Also, I am grateful for the experimental work performed by Dr. Shibayan Roy and Souvik Sahoo (Indian Institute of Technology Kharagpur) which provided much needed microstructural images as well as the assistance of Mostafa Mahdavi and Dr. Jason Allen for their consultation and support.

I am thankful for the support of the National Science Foundation Graduate Research Fellowship Program (NSF DGE-1650044) and the Boeing Company (Co-PIs Dr. Steven Liang and Dr. Hamid Garmestani). Any opinions, findings, conclusions or recommendations expressed here are those of the author and do not necessarily reflect the views of the NSF or the Boeing Company.

Lastly, I am would like to thank my friends and family who have supported and encouraged me during the completion of my Ph.D.

TABLE OF CONTENTS

LIST OF TABLES

LIST OF FIGURES

SUMMARY

Three microstructural evolution models are developed and presented which utilize different processing techniques, microstructural features, and modeling technique for forward or inverse modeling. The first model is an inverse model capable of predicting the initial microstructure required to obtain a desired final microstructure for use in nuclear forensics applications. This inverse model describes the microstructure evolution of a monotectoid Zr-18wt.%Nb alloy by specifying the crystallographic orientation of the bcc β-phase ZrNb. By modeling the evolution of the crystallographic orientation the model attempts to provide information on how the material was processed and a framework which allows for the optimization of the mechanical material properties. The second model is a forward model which utilizes two-point correlation functions to describe the phase distribution of the dual phase Ti-6Al-4V alloy in order to predict the final microstructure obtained after a known initial microstructure undergoes a specified processing procedure. This model uses statistical continuum theory to describe the deformation of the two-point correlation functions and reconstructs the deformed statistics by systematic deformation of the initial two-point correlation function. The last model is an inverse model which predicts the initial microstructure required to obtain a desired final microstructure using the two-point correlation functions described in the second model. This model attempts to provide a computational model capable of providing optimization of material microstructure and thus mechanical properties for industrial applications. Ultimately, the goal of these models is to reduce the industrial requirement of trial-and-error experiments

for the development of new processing procedures and provide an avenue for the development of these new procedures through computational simulations.

CHAPTER 1. INTRODUCTION

Modeling efforts cover all realms of research and length scales from the atomic to the galactic. As computational resources have become cheaper and more powerful, so too have modeling efforts become more detailed in an attempt to get as close to reality as possible. It is often seen that as models become more and more detailed the time required to run such models also increases, at best linearly and at worst exponentially. However, applications for in-line operations (i.e. optimization of additive manufacturing processes) which require fast responses cannot wait for these long simulation times. For material science modeling, the amount of microstructural information modeled through the simulations tends to have a direct impact on the computational time required. The exception to this rule comes in the form of statistical functions; these allow for the microstructure to be defined in a mathematical framework which can greatly reduce the computational time.

The first chapter of this work will provide important information for the understanding of the methodologies and ideas presented here. This chapter will expand upon microstructure evolution modeling as well as provide introductory information into crystallographic orientation and two-point correlation functions.

In chapter two an inverse model for the prediction of crystallographic orientation will be presented for a nuclear forensics application. The model will be applied to a hot-rolled and intermittently annealed Zr-Nb alloy at the monotectoid composition. Due to the annealing stage of the processing procedure a novel recrystallization subtraction methodology is utilized in conjuncture with Fourier transformations to predict the

orientation evolution. Qualitative and quantitative error analyses are performed to illustrate the accuracy of the model and to provide validation of the methodologies utilized.

In chapter three, the phase distribution of a dual-phase Ti-6Al-4V alloy will be described using two-point correlation functions and a model is developed to describe the evolution of the correlation functions. The model developed here expands on a previous statistical continuum model to describe the evolution of the full two-point statistics map as a function of strain. The model is then applied to isothermal compression in a dual-phase Ti-6Al-4V alloy which have been deformed at various strain rates. An error analysis is performed to describe the accuracy of the model and illustrate the effect of representative statistics on modeling efforts.

In chapter 4, an inverse model is developed for the prediction of the initial two-point statistics required to obtain a desired final set of statistics. The model is developed following the ideas of the existence of a microstructural hull for two-point statistics. This inverse model is applied to a dual-phase Ti-6Al-4V alloy deformed using the model presented in chapter three. An error analysis is performed to describe the accuracy of the inverse model and specify the avenues available for future work in this area.

Lastly, chapter five provides a summarization of the conclusions obtained for each of the models presented in this work. A summarization of the future work for each chapter is also provided in chapter five. It is the goal of this work to produce models which simulate the evolution of microstructural statistics, to provide accurate reporting of the deformation microstructure with faster computational times, and to reduce the dependence on finite element models for microstructure evolution.

1.1 Microstructure Modeling

Microstructure evolution modeling is an umbrella term which encompasses both forward and inverse models. Forward models are models which deform a known initial microstructure using a specific set of processing conditions to predict the final microstructure after processing. **Figure 1** illustrates a schematic which describes the forward model methodology.

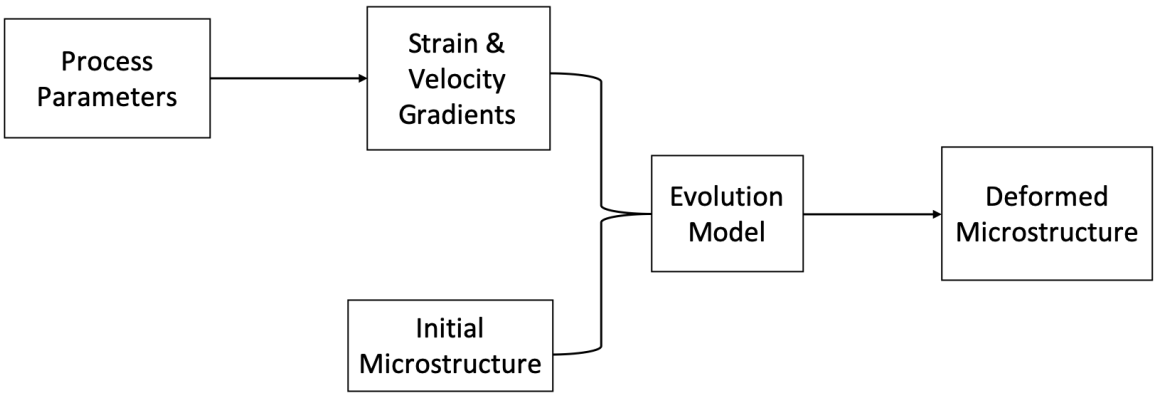

Figure 1: Schematic of the forward model methodology for microstructure evolution models.

Forward models encompass most of the past research conducted into microstructure evolution modeling. The Potts model, the JMAK equation, the viscoplastic self-consistent (VPSC) model, and finite element models are all examples of forward models which are capable of predicting the evolution of different microstructural features[1-4]. Forward models are defined as one-to-one models. This means that a single unique solution is obtained for every set of initial microstructure and processing conditions. This is not the case for inverse models.

Inverse models follow the opposite methodology of the forward models. An inverse model is defined as a model which predicts the initial microstructure and processing conditions that are required to obtain a desired final microstructure. **Figure 2** shows a schematic of the inverse model methodology.

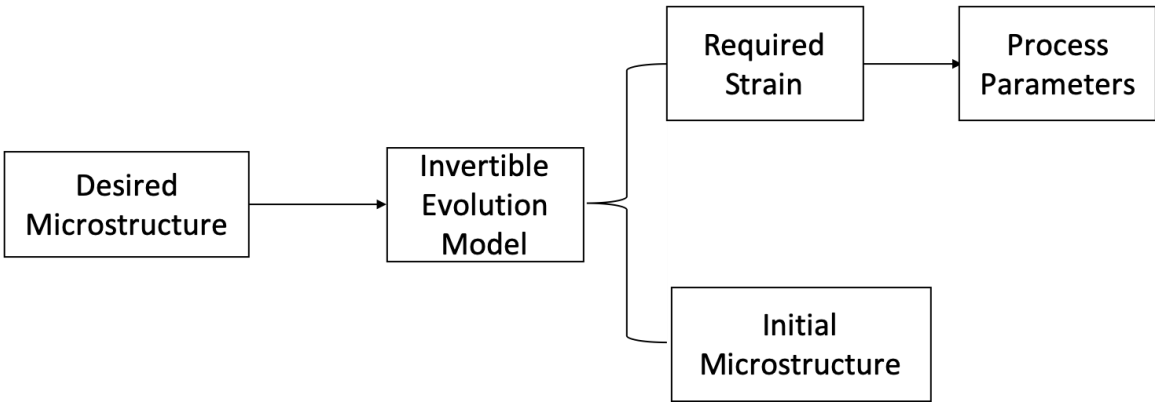

Figure 2: Schematic of the inverse model methodology for microstructure evolution models.

Research into inverse models for microstructure prediction has increased in the past twenty years. This increase in research interest is partially due to the large impact that such inverse models have for both industrial and forensics applications. Currently, in industrial settings, new processing procedures are developed using either trial-and-error based experiments or forward model techniques. However, these techniques do not allow for the optimization of material microstructure or properties. Inverse models can be utilized to predict the initial microstructure and processing conditions needed to obtain a desired final microstructure. This definition allows for the optimization of both material microstructure and properties in a way that forward models are unable to do. It is important to note that while forward models exhibit a one-to-one relationship between initial and final microstructures, inverse models do not exhibit this relationship. This is to be expected as

multiple different initial microstructures can reach the same final state given different processing conditions. This means that the results of an inverse model will be viable solutions but will not be unique.

1.2 Crystallographic Orientation: A Microstructural Feature

A material's microstructure is described based on the feature of interest. These microstructural features range from grain size distributions, to volume fraction of phases and grain morphology[5-7]. One such microstructural feature is the orientation of each crystal in a material called the crystallographic orientation. Crystalline materials, like Ti-6Al-4V or AA7075, are made up of regions of constant lattice orientation called grains. Crystallographic orientation is the grain's orientation when compared to a reference frame and is described using three angles. In 1776, Leonhard Euler introduced the idea that the orientation of a rigid body, with respect to a reference frame, can be described as a set of three angles which were later termed Euler angles. H.J. Bunge applied these Euler angles to describe the orientation of each grain in a crystalline microstructure. **Figure 3** describes the process of transforming a reference frame into the grain frame using Bunge's description of Euler angles $(\varphi_1, \phi, \varphi_2)$ [8].

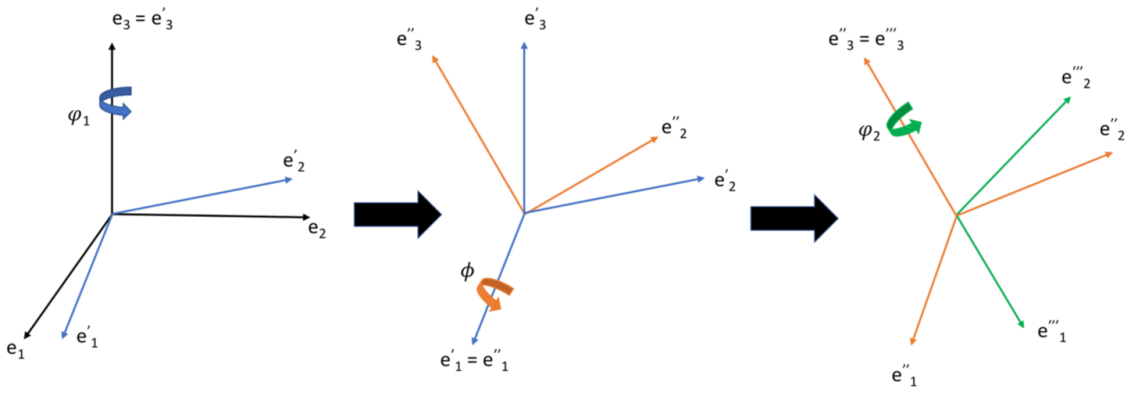

Figure 3: Graphical representation of the Bunge description of Euler angles.

There are four different Euler angle conventions used by the crystallographic orientation community which are attributed to Bunge, Roe, Canova and Kocks. The Canova representation is a direct inverse of the Bunge description. **Figure 4** describes the Kocks and Roe descriptions of the Euler angles[9,10].

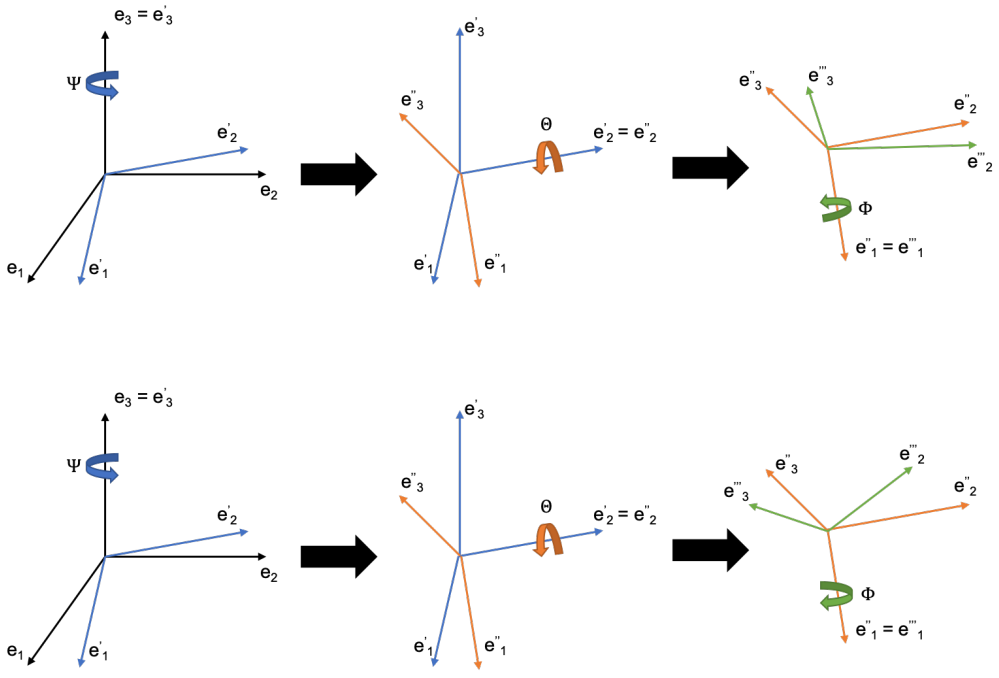

Figure 4: Graphical representation of the Kocks (top) and Roe (bottom) descriptions of Euler angles.

In the crystallographic orientation community, the Bunge description is most commonly used and will therefore be used in this work. Crystallographic orientation can be used to describe microstructural information (preferred vs random orientation) and has been shown to have a large impact on the mechanical properties of polycrystalline materials. Therefore, crystallographic orientation is a microstructural feature of interest for modeling microstructure evolution due to processing.

Crystallographic orientation can be mathematically described using a probability distribution function called the orientation distribution function (ODF). The ODF is a probability distribution function across Euler space (the 3D space described by ϕ_1, ϕ, and φ_2) which specifies the probability of a grain having an orientation, g, where $g = (\varphi_1, \phi, \varphi_2)$. Equation 1 describes the calculation of the ODF mathematically using a counting method which counts how many randomly chosen points have the chosen orientation vs the total number of chosen points.

$$\frac{dV}{V} = f(g)dg \tag{1}$$

The intensity of the ODF is in terms of 'times random' because the ODF is normalized with respect to a random microstructure. This means that when the intensity of the ODF is greater than 1 the material is said to be textured and when the intensity is 1 the material is said to have a random texture.

1.3 Two-Point Correlation Functions

Two-point correlation functions are a subset of N-point correlation functions which use vectors to describe the distance between microstructural features of interest. Two-point correlation functions therefore describe the probability of finding a vector, $\vec{\boldsymbol{r}}$, for which the head of the vector lies in feature i and the tail lies in feature j, where $i, j = 1, 2, \ldots, n$ and n is the total number of distinct features[11]. There are two forms that the two-point correlation function can take, these are the autocorrelation (when $i = j$) and the cross-correlation (when $i \neq j$). A key characteristic for two-point correlation functions is that when $|\vec{\boldsymbol{r}}| = 0$ the two-point correlation function collapses to the one-point correlation function. One-point correlation functions are similar to two-point correlation functions, but instead of throwing vectors the one-point correlation function counts singular points. This means that the ODF is a one-point correlation function for crystallographic orientation, while volume fraction of phases is the one-point correlation function for multi-phase materials. The simplest form of the two-point correlation function is used to describe a two-phase isotropic material. For isotropic cases, the two-point correlation function is considered to be constant for all θ values, and as such the correlation functions are a function only of the magnitude of $\vec{\boldsymbol{r}}$. In 1974, P. Corson developed an empirical equation for calculating the two-point correlation function for isotropic two-phase materials[12,13]. This equation became known as Corson's equation and is mathematically defined by equation 2.

$$P_{ij}(r) = \alpha_{ij} + \beta_{ij} e^{-c_{ij} r^{n_{ij}}} \tag{2}$$

In equation 2, α_{ij} and β_{ij} are constants which are calculated from the volume fraction of each phase, c_{ij} and n_{ij} are empirically calculated from experimental images, and r is the distance between the two points. Furthermore, the limiting conditions (when $r = 0$ and $r \to \infty$) are defined for each of the four correlation functions in **Table 1**[13]. When successfully calibrated following the limiting conditions in **Table 1**, Corson's equation provides a methodology for describing the two-point statistics of an isotropic microstructure mathematically. Thus, by evolving the Corson's equation description, the two-point statistics are evolved as well.

Table 1: Limiting conditions and resultant coefficients for Corson's equation.

	Boundary Conditions		Resultant Coefficients	
P_{ij}	$r = 0$	$r \to \infty$	α_{ij}	β_{ij}
P_{11}	V_1	V_1^2	V_1^2	V_1V_2
P_{12}	0	V_1V_2	V_1V_2	$-V_1V_2$
P_{21}	0	V_1V_2	V_1V_2	$-V_1V_2$
P_{22}	V_2	V_2^2	V_2^2	V_1V_2

CHAPTER 2. TEXTURE MODELING FOR NUCLEAR FORENSICS APPLICATIONS

2.1 Introduction to Nuclear Forensics

The field of nuclear forensics focuses on the investigation of interdicted nuclear material for the goal of identifying the originating region, facility or nation. These investigations often revolve around the identification of isotope balances, radio-chronometric age, and physical macroscopic structural features[14]. While each individual characteristic has a role to play in the identification of the location of origin, it is normally only investigations which obtain results from multiple characteristics that are able to provide a strong declaration of the origin location. However, obtaining multiple characteristics and the corresponding analysis of each type of characteristic are time consuming approaches which could be detrimental to an investigation in which time is of the essence. For this reason, the identification of a singular characteristic which can provide a quick and accurate identification of the origin of interdicted material is of great interest to the nuclear forensics community. Crystallographic orientation can provide this, as texture is highly dependent on the processing procedure employed. Therefore, through the modeling of the evolution of texture it is possible to identify the processing procedure used for the creation of the interdicted material and thus the location of origin.

2.2 Hot Rolling and Monotectoid BCC Zr-Nb

Zr-rich Zr-Nb alloys have multiple uses in the biomedical industry for prosthetic implants[15-17], and in the nuclear energy industry as cladding material[18-20]. Zr-Nb alloys

consist of two main equilibrium crystallographic phases, a high temperature β-phase and a room temperature α-phase. The high temperature β-phase exhibits a body-centered cubic (bcc) lattice structure that has a random solid solution mixing of Zr and Nb atoms[21]. The room temperature α-phase exhibits a Zr-rich hexagonally close-packed (hcp) structure. The monotectoid composition of 18.8w% Nb was chosen as a surrogate for the monotectoid U-Nb alloy commonly used in nuclear applications[21,22]. At this monotectoid composition, a phase transformation occurs at 620 ± 10°C where the bcc β-ZrNb phase transforms into the hcp α-ZrNb phase and a bcc β-Nb phase, which resembles a Zr depleted β-ZrNb structure[23]. The β-phase has also been observed to transform into the non-equilibrium trigonal ω-phase, common to Zr and Ti systems, at Nb compositions below the monotectoid composition[24-26]. For the nuclear forensics application studied here, the monotectoid Zr-Nb material was processed using a hot rolling technique at a temperature of 1000°C. The processing temperature used is well above the monotectoid transition temperature; as such most deformation will be evident in the β-ZrNb. Therefore, the microstructure analysis presented here is focused on the texture evolution of the β-ZrNb phase only, as the low-temperature phases will not form in large enough quantities to accurately analyze.

The thermo-mechanical processing procedure employed involved successively annealing and hot rolling the ZrNb samples to increasing levels of height reduction. The evolution of crystallographic texture was captured through intermittent X-Ray diffraction (XRD) based texture measurements. The ZrNb sample pucks, with an approximate height of 5mm and diameter of 18mm at the start, were sectioned from a rod obtained from AMES Laboratory. The ZrNb rod was fabricated from pure Zr and Nb chunk material which had

been triple-arc melted into small pieces and then drop-cast into a single rod using a water-cooled copper hearth. The exact composition of the rod, as reported by AMES, was 18.271w% Nb corresponding to the monotectoid composition of the ZrNb system[27]. Five pucks were sectioned from the rod, and were lightly polished to remove deformation caused by the sectioning process.

One puck was set aside to be the reference "as-cast" sample representing the initial microstructural state of the system. The remaining four pucks were subjected to the hot rolling procedure. This procedure involved first heating the sample at 1000°C for five minutes, then quickly moving the sample from the furnace to the roller where an approximate 2% height reduction was performed. After the 2% rolling pass was completed, height measurements were taken and the sample was returned to the furnace to begin the next rolling step. This process was repeated several times for each of the four pucks until the total height reduction designated for each puck was reached. These designated height reductions were 10%, 20%, 30% and 40% total reduction. As each sample reached its designated reduction in height, the sample then underwent a final five minute anneal at 1000°C and room temperature water quenching. The furnace used to heat the samples was an MTI Corp GSL-1700s60 high temperature vacuum/gas tube furnace fitted with an alumina tube. A large General Electric Motors 1960s rolling mill was used to perform each of the rolling steps.

Each sample, including the as-cast sample that was set aside, was polished using an Allied High Tech MetPrep 4TM auto-polisher to a 1200 grit (P-4000) final polish for XRD characterization. This was done to remove any oxides that may have formed on the surface of the samples during annealing. Absolute X-Ray scans were first performed using a

PANalytical Empyrean diffractometer equipped with Cu Kα X-Rays, over a 20-120° 2θ range to analyze and verify that the annealing stages were hindering the formation of α-phase ZrNb grains. Once the phases and bcc peaks were identified, the samples were moved to a PANalytical X'Pert3 MRD diffractometer equipped with a Chi-Phi-Z stage and Cu Kα X-Rays to perform texture measurements on the bcc β-phase. Of the several β-phase peaks identified, accurate raw pole figures were measured for the {002}, {112}, {222} and {123} reflections. These peaks were selected based on a criteria of strong peak intensity, minimal overlap with secondary α-phase peaks, and with spectral peaks produced by unfiltered source X-rays. Texture analysis and figure creation was performed using the MTEX software package for MATLAB[28].

2.3 Mathematical Theory

The purpose of the inverse model is to create a relationship between the orientation distribution functions at two different stages of a processing procedure. To do this, the ODF is mathematically described as a transformation of a set of orthogonal basis functions using a set of coefficients called the texture coefficients. Traditionally, the ODF has been defined using the generalized spherical harmonic functions as shown by Bunge[8] in equation 3.

$$f(g,\eta) = \sum_{l=0}^{\infty} \sum_{m=0}^{M(l)} \sum_{n=0}^{N(l)} F_l^{mn}(\eta) \dot{\dot{T}}_l^{mn}(g) \tag{3}$$

Here, $\dot{\dot{T}}_l^{mn}(g)$ describes the symmetric generalized spherical harmonics while $F_l^{mn}(\eta)$ are the texture coefficients and $g = (\varphi_1, \phi, \varphi_2)$ is the Bunge convention for describing Euler

angles. To describe the evolution of Euler space due to an imposed strain-rate, Clement and Coulomb[29] developed a conservation equation described by equation 4.

$$\frac{\partial f(g,\eta)}{\partial \eta} + \frac{1}{sin\phi} div[f(g,\eta) sin\phi R(g)] = 0 \tag{4}$$

Using the generalized spherical harmonics description for the ODF Bunge et al.[30] expanded equation 4 to obtain a general linear relationship between the texture coefficients of two ODFs specified by equation 5.

$$\frac{\partial F_l^{mn}(\eta)}{\partial \eta} = \sum_{\lambda,\sigma,\rho} A_{l\lambda}^{mn\sigma\rho} F_\lambda^{\sigma\rho}(\eta) \tag{5}$$

Li et al.[31] then performed an integration on this linear relationship to obtain an equation which describes the texture coefficient evolution as a function of strain and processing conditions.

$$F(\eta) = e^{A(\eta-\eta_0)} F(\eta_0) \tag{6}$$

In equation 6, A is the process path function which describes the material response to the imposed processing procedure. Meanwhile, η and η_0 correspond to the strain associated with the final microstructure and initial microstructure respectively. Fundamentally, equation 6 is a relationship that directly connects the texture components of microstructures with different strains to each other using the process path function. The process path model has been utilized for different material systems and processing conditions to predict the texture coefficients for path optimization[32-36]. However, algorithms and models

employing the use of generalized spherical harmonics tend to be computationally inefficient. In order to combat this issue, a new definition for the ODF is created using a Fourier transformation method as shown by equation 7.

$$f(g,\eta) = \sum_{n} \chi_n e^{2\pi i\left(\frac{n}{T}\right)x} = \sum_{n} \chi_n * E \tag{7}$$

Here, χ_n are the texture coefficients associated with the Fourier transformation and are similar to the texture coefficients in equation 3. Furthermore, E is a replacement for the Fourier basis functions similar to $\dot{\ddot{T}}_l^{mn}$ for the generalized spherical harmonics. By following the work done by Bunge et al.[30], a new form of equation 6 can be identified using Fourier transformation. To do this, equation 4 is simplified for the conservation of matter in a volume element of Euler space to obtain equation 8.

$$\frac{\partial f(g,\eta)}{\partial t} + div[f(g,\eta)R(g)] + ctg\phi f(g,n)R(g) = 0 \tag{8}$$

Equation 7 is then substituted into equation 8 to obtain:

$$\sum \frac{d\chi_n(\eta)}{d\eta} E(g) + \sum \chi_n(\eta)[div\big(E(g)R(g)\big) + ctg\phi E(g)R(g)] = 0 \tag{9}$$

Continuing to follow the work by Bunge et al.,[30] the second summation in equation 9 can be defined as a Fourier transformation as shown by equation 10.

$$\sum \chi_n(\eta)[div\big(E(g)R(g)\big) + ctg\phi E(g)R(g)] = \sum A\chi_m \tag{10}$$

Thus, a new general linear relationship is obtained between the Fourier texture coefficients as described by equation 11.

$$\frac{d\chi_n(\eta)}{d\eta} = \sum A\,\chi_\eta \tag{11}$$

Lastly, equation 11 is integrated following the work of Li et al.[31] to obtain equation 12 which is called the conservation of crystallites.

$$\chi_n(\eta) = e^{A(\eta-\eta_0)}\chi_n(\eta_0) \tag{12}$$

Equation 12 is of the same form as equation 6, where A is the process path function associated with the material response to the imposed processing procedure. However, the process path function in equation 12 is associated with a Fourier definition for the ODF. Therefore, equation 12 is an invertible model which has the capability to predict the evolution of the texture coefficients due to a known processing. The key to using equation 12 for an inverse model is to first identify the process path function using known experimental data. To do this, equation 12 is rewritten to obtain equation 13.

$$A = \frac{\ln[\chi(\eta) * \chi_0^{-1}(\eta)]}{\eta - \eta_0} \tag{13}$$

Equation 13 defines the process path function as a function of the texture coefficients and the associated strain values. To calculate the process path function, two ODFs are experimentally obtained from two samples with known strain values. The ODF corresponding to the lower strain value is considered to be the "initial" ODF, while the

larger strain value corresponds to the "final" microstructure. Once two experimentally measured ODFs with known strain values are obtained, all the information is known to allow the calculation of the process path function between the two strains. However, as with all experimentally driven models, the more data points that are used to calculate the process path function, the greater the accuracy of the model.

For this application, the process path function was calculated using the texture coefficients of the 0%, 20%, 30% and 40% reduced samples. A more in-depth look at the method for calculating the process path function using four data points will be presented in section 2.4. The calculated process path function was then saved to be used as an input in future inverse simulations. Once the process path function is known, equation 12 can be rewritten again to describe the initial texture coefficients as a function of the process path function and the final texture coefficients as described by equation 14.

$$\chi_0(\eta) = \chi(\eta)\left[e^{A(\eta-\eta_0)}\right]^{-1} \tag{14}$$

It is important to note that this model is used for processing conditions that do not include recrystallization or phase transformations. This is due to the fact that this model assumes that there is a continuous path which can be followed from the initial microstructure to the final microstructure as a function of strain. However, recrystallization and phase transformations are discontinuous processes and, as such, break this assumption. In this application, any phase transformations are hindered by water quenching after the final annealing stage. However, the thermo-mechanical nature of the processing procedure means that recrystallization occurs throughout processing. In order to limit the effect of recrystallization, the experimentally measured ODFs were considered to be a combination

of a deformation ODF, $f_{def}(g,\eta)$, and a recrystallization ODF, $f_R(g)$, as described by equation 15.

$$f_{exp}(g,\eta) = f_{def}(g,\eta) + \nu_R(\eta) f_{recry}(g) \tag{15}$$

The recrystallization ODF was calculated by measuring the difference in the ODF of the 10% reduced sample and a separate sample which was rolled to 10% reduction and immediately quenched without a final annealing step. The experimentally measured ODF of the non-annealed sample was then subtracted from the ODF of the sample that underwent the final annealing stage using the MTEX package for MATLAB. **Figure 5** shows the $\varphi_2 = 0°$ and $\varphi_2 = 45°$ sections of the recrystallization ODF that was calculated in this way.

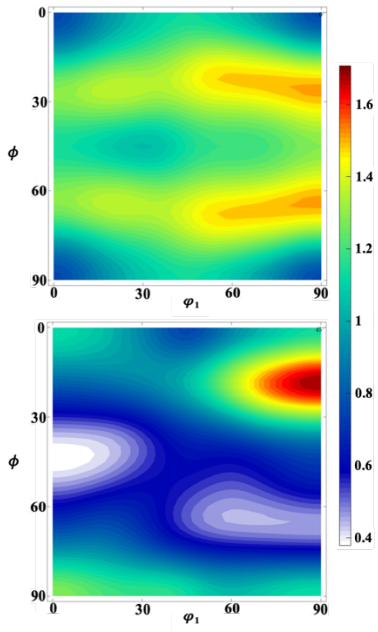

Figure 5: φ_2=0° (top) and φ_2=45° (bottom) sections of the calculated recrystallization ODF caused by the annealing process after 10% deformation.

Figure 5 identifies that there is a strong texture at $g = (90°, 15°, 45°)$ as well as two texture fibers in the $\varphi_2 = 0°$ section at $\phi = 25°$ and $65°$. The $v_R(\eta)$ term in equation 15 is a weighting term used to represent the effect of more annealing steps on the strength of the recrystallization ODF. The $v_R(\eta)$ term was calculated by dividing the number of annealing steps that occurred by the number of annealing steps that occurred for the 10% reduced sample. **Table 2** shows the value of $v_R(\eta)$ for each of the samples.

Table 2: Recrystallization weights for each of the rolled samples.

Height Reduction	$v_R(\eta)$ value
10%	1
20%	2.2
30%	3.2
40%	4.2

Furthermore, since the pucks are heated to $1000°C$ for five minutes prior to any deformation, the 0% reduced ODF was obtained by heating the as-received ZrNb puck to $1000°C$ for five minutes followed by water quenching. This was done in order to more accurately define the initial microstructure since the recrystallization will affect the resulting deformation evolution. **Figure 6** shows the $\varphi_2 = 0°$ and $\varphi_2 = 45°$ ODF sections for the annealed 0% reduced sample.

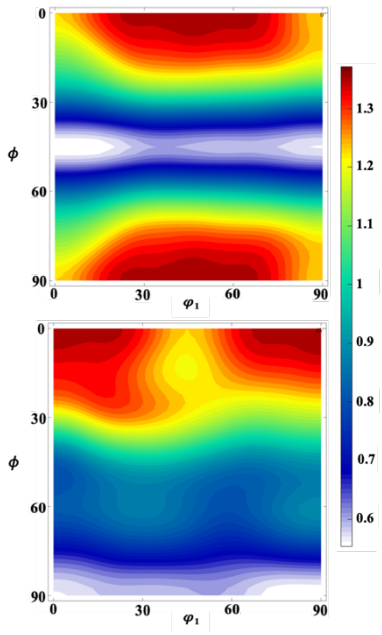

Figure 6: φ_2=0° (top) and φ_2=45° (bottom) sections of the experimentally measured ODF for the annealed 0% reduced sample.

2.4 Texture Prediction Results

The texture analysis presented in this work is focused on identifying the texture evolution of the bcc β-ZrNb phase. Therefore, it was necessary to design an experimental processing procedure which preserved the dominance of the β-phase and suppressed the formation of other secondary phases, which could alter the texture evolution behavior. The hot rolling and annealing temperature of $1000°C$ was chosen for this purpose as it is well above the monotectoid transformation temperature. The final five minute annealing and quenching step at the end of each rolling cycle also helped to increase the formation of the β-phase and subdue any α precipitation. To verify the hindrance of the α-phase precipitation, an X-ray diffraction phase analysis was performed.

Figure 7 shows the XRD profile of the 0% reduced sample alongside the XRD profile of the 40% reduced sample. The strongest peaks visible in each plot correspond to the β-phase suggesting that throughout the processing procedure the β-phase successfully dominated all other phases. The formation of α-phase grains was not suppressed completely as the spectra of the 40% reduced sample shows evidence of very small peaks that correspond to the existence of α-phase grains. This small fraction of α-phase was found to have precipitated in sparse quantities along some grain boundaries[37].

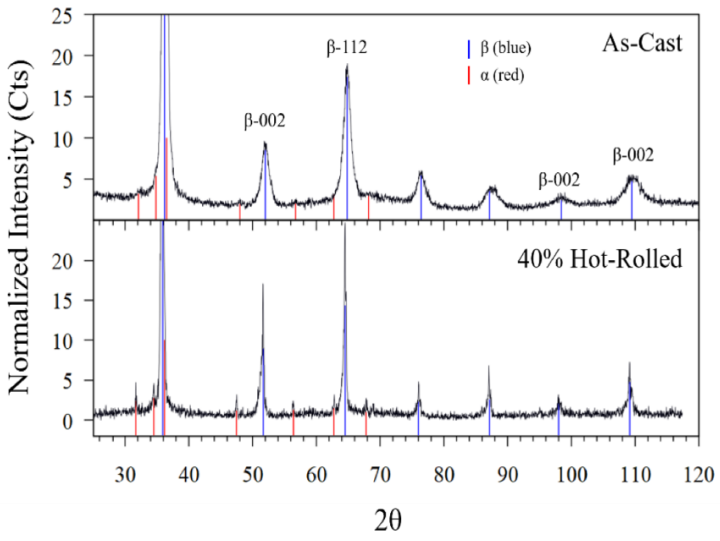

Figure 7: XRD profiles of the initial as-cast sample puck and the 40% reduced puck. Both profiles show that the samples were almost totally dominated by β-Zr-Nb phase (peaks denoted by blue lines). The 40% Hot Rolled profile does, however, show the formation of very small amount of α-Zr-Nb precipitates (peaks denoted by red lines). The Y-range (intensity) of these plots has been truncated so that the α-phase peaks would be visible. Only the large β-(011) peak at 36° 2θ was cut off, at approximately 35% of its total height in each profile.

In order to maintain the focus and discussion on the development and analysis of the inverse model for texture prediction, a full analysis of the β-phase texture evolution is not given here, but is provided by Startt et al.[37] in which the texture of a single ZrNb

sample puck, subjected to the same thermo-mechanical processing, was measured both locally at the surface using electron backscatter diffraction (EBSD) and globally using XRD. From this analysis, the most dominant and important texture components were determined and analyzed. These are summarized in **Figure 8** which depicts schematics of the $\varphi_2 = 0°$ and $\varphi_2 = 45°$ ODF sections. The most dominant texture components in this system are the γ-fiber, marked by the green line in the $\varphi_2 = 45°$ section, and the {001}<100> (cube) and {001}<110> (rotated cube) components, denoted by the blue and red dots in the $\varphi_2 = 0°$ section respectively.

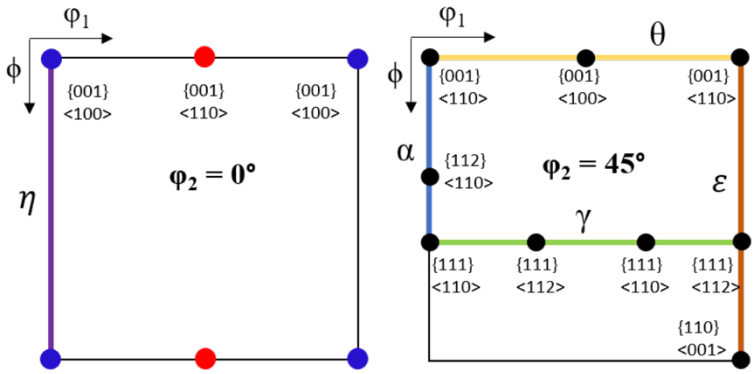

Figure 8: Schematic of the texture components commonly found in the φ_2=0° (left) and φ_2=45° (right) sections of a hot rolled bcc crystal[37].

As specified previously, the calculation of the process path function was performed using the ODFs of the 0%, 20%, 30% and 40% reduced samples. This was done by calculating three separate path functions, $A_{0->20}$, $A_{20->30}$, and $A_{30->40}$. Since the path function is calculated here using an experimentally driven method, these path functions are most accurate between the two samples specified. For example, the $A_{0->20}$ path function is most accurate when calculating for reductions between 0% and 20%. In order to obtain a

more generic path function which would be accurate for all reductions from 0% to 40%, a multi-step calculation using equation 12 was performed and is described by equation 16.

$$F_f(\eta_{40}) = e^{A(\eta_{40}-\eta_{30})}\left[e^{A(\eta_{30}-\eta_{20})}\left(e^{A(\eta_{20}-\eta_0)}\right)\right]F(\eta_0) = e^{A(\eta_{40}-\eta_0)}F(\eta_0) \quad (16)$$

Simplifying equation 16 and rewriting allows for the description of the general process path function, A, as a function of the specific path functions calculated using the experimentally measured ODFs described by equation 17.

$$A = \frac{[A_{30\rightarrow40}(\eta_{40}-\eta_{30}) + A_{20\rightarrow30}(\eta_{30}-\eta_{20}) + A_{0\rightarrow20}(\eta_{20}-\eta_0]}{\eta_{40}-\eta_0} \quad (17)$$

In equation 17, A is now a generic path function which is expected to be accurate for all height reductions between 0% and 40%. The multi-step process used to obtain equation 17 does not limit itself to three steps, and as such can be easily expanded to include as many steps as necessary as long as the data is available. Since this is an experimentally driven model, as the number of data points used to calculate the generic path function increases then the accuracy of the model is expected to increase as well.

Once the general process path function was calculated, it was saved as an input to be loaded into the inverse model for future simulations. This was done to show that the processing path function does not have to be recalculated for every inverse simulation. **Table 3** specifies the variables involved in each simulation that was performed using the inverse model that has been described.

Table 3: Specification of simulation variables for each inverse model simulation performed.

Simulation Number	Final Texture Coefficients	$\eta_f - \eta_0$	Simulated Initial Texture Coefficients
1	40% reduced	40 – 10 = 30	10% reduced
2	40% reduced	40 – 20 = 20	20% reduced
3	40% reduced	40 – 30 = 10	30% reduced
4	30% reduced	30 – 10 = 20	10% reduced
5	30% reduced	30 – 20 = 10	20% reduced
6	20% reduced	20 – 10 = 10	10% reduced

Figures 9 through **11** use the texture coefficients of the 40% reduced sample (**Figure 9**), 30% reduced sample (**Figure 10**) and 20% reduced sample (**Figure 11**) as the final texture coefficients in equation 12 to predict the 10% reduced ODF. For each of these figures the simulated 10% reduced ODF is compared to the experimentally measured ODF of the 10% reduced sample to provide insight into the accuracy of the inverse model.

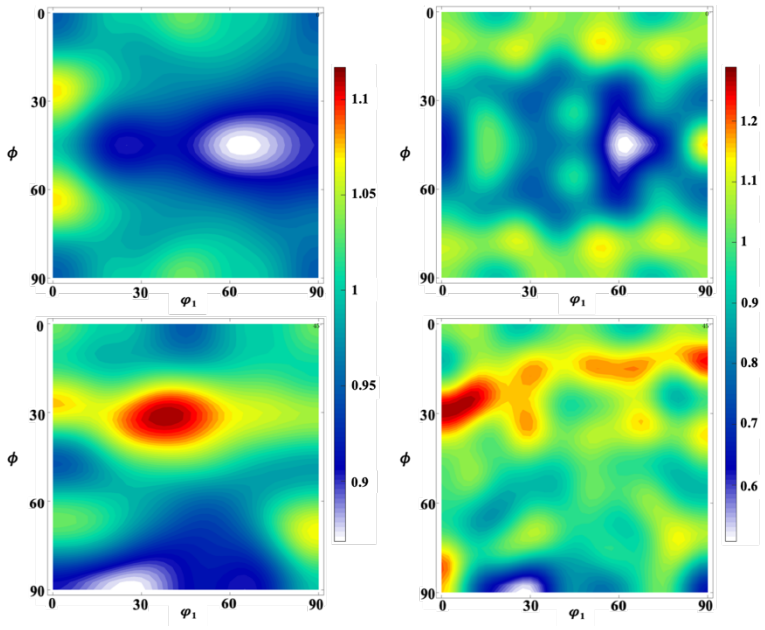

Figure 9: φ_2 = 0° (top) and 45° (bottom) sections of the experimentally measured ODF for the sample rolled to 10% reduction (left) and the simulated ODF (right) following the parameters for simulation 1 in Table 3.

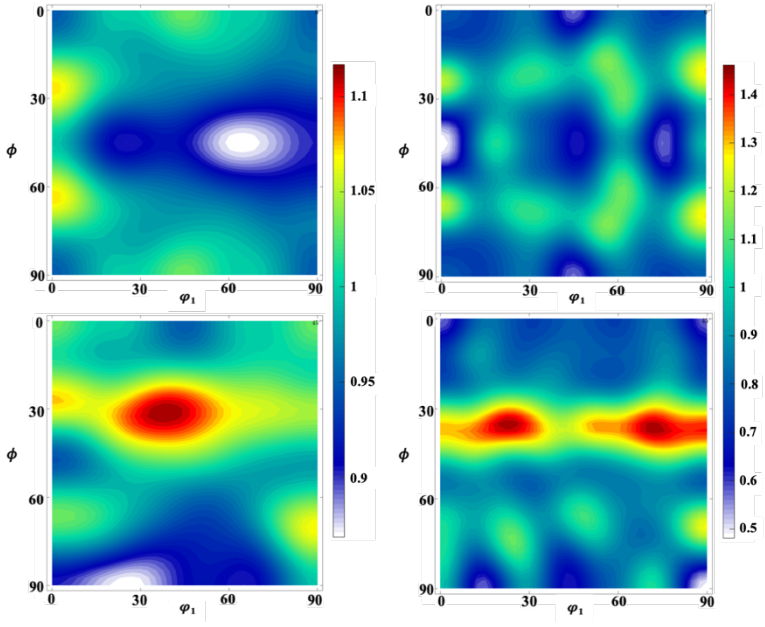

Figure 10: φ_2 = 0° (top) 45° (bottom) sections of the experimentally measured ODF for the sample rolled to 10% reduction (left) and the simulated ODF (right) following the parameters for simulation 4 in Table 3.

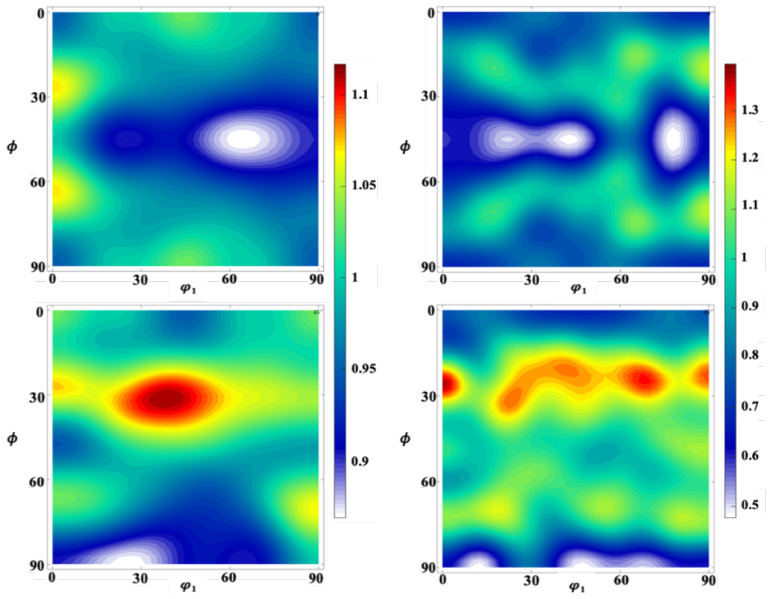

Figure 11: $\varphi_2 = 0°$ (top) and $\varphi_2 = 45°$ (bottom) sections of the experimentally measured ODF for the sample rolled to 10% reduction (left) and the simulated ODF (right) following the parameters for simulation 6 in Table 3.

Figures 9 through **11** illustrate three simulations which all attempt to predict the same initial microstructure using different final microstructures. These figures show that inverse model is capable of accurately predicting the texture of the initial microstructure. In each figure, the dual fibers identified in the $\varphi_2 = 0°$ section of the experimental ODF are evident in the $\varphi_2 = 0°$ section of the simulated ODF. Furthermore, the strongest intensity fiber in the $\varphi_2 = 45°$ section of each simulated ODF corresponds very well to the $\phi = \sim 30°$ fiber in the $\varphi_2 = 45°$ section of the experimental ODF. The largest errors evident in the simulations shown by **Figures 9** through **11** can be seen when looking at the location of the highest intensity peaks. For example, in **Figure 9** the location of the highest intensity peak in the simulated ODF is at $g = (0°, 30°, 45°)$ while in the experimental ODF it is at $g = (40°, 30°, 45°)$, roughly. The $g = (0°, 30°, 45°)$ peak can also be found as a peak of high intensity in the recrystallization ODF illustrated by **Figure 5**. It is expected

that the cause for the shift in the highest intensity peak is due to an inaccurate calculation for the intensity of the recrystallization ODF for the 40% reduced sample. However, the location of the fibers associated with the experimental ODF can be easily seen in the simulated ODFs, and therefore it is expected that the errors will decrease with more experimental data points and a better prediction for the recrystallization ODF at different strain values.

Figures 12 and **13** compare the experimentally measured ODF of the 20% reduced sample to the predicted 20% reduced ODF using the texture coefficients of the 40% and 30% reduced ODFs respectively (simulations 2 and 5).

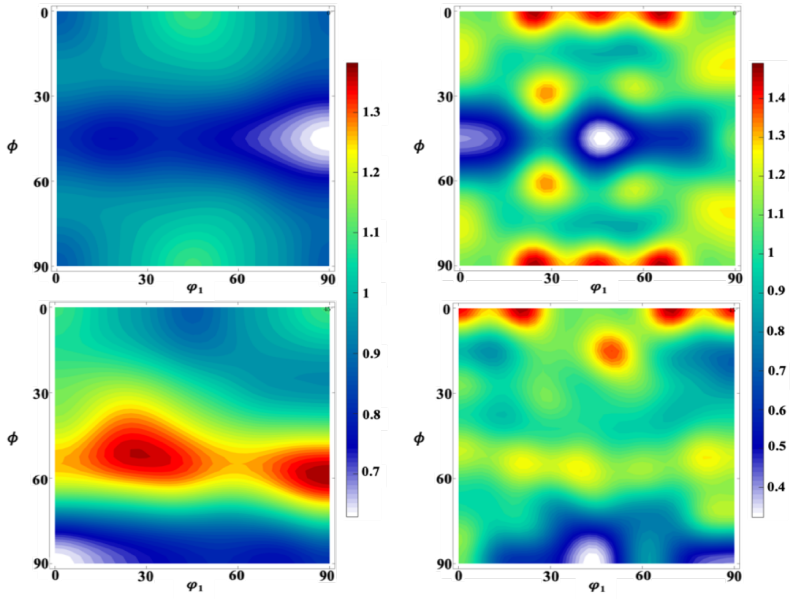

Figure 12: $\varphi_2 = 0°$ (top) and $\varphi_2 = 45°$ (bottom) sections of the experimentally measured ODF for the sample rolled to 20% reduction (left) and the simulated ODF (right) following the parameters for simulation 2 in Table 3.

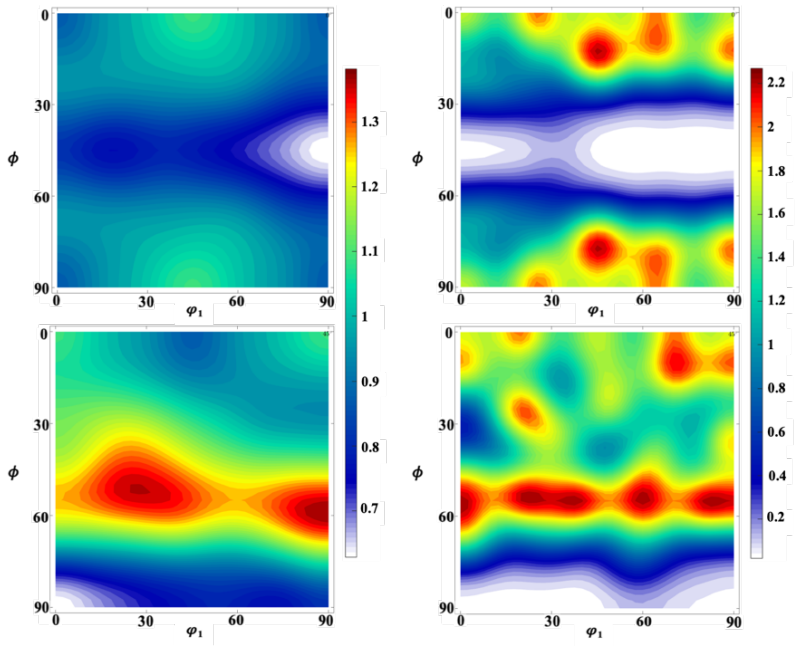

Figure 13: φ_2 = 0° (top) and φ_2 = 45° (bottom) sections of the experimentally measured ODF for the sample rolled to 20% reduction (left) and the simulated ODF (right) following the parameters for simulation 5 in Table 3.

Figures 12 and **13** provide similar insight into the accuracy of the inverse model as **Figures 9** through **11**. From **Figures 12** and **13** it is evident that the location of the γ-fiber, as well as the cube and rotated-cube components (identified in **Figure 8**) are predicted accurately using the inverse model. However, for these simulations, the cube and rotated-cube components are simulated as decomposed when compared to the experimental results and in **Figure 12** the intensity of the γ-fiber is lower than in the experimental ODF. For both of these locations of error it is expected that the error will increase with better prediction of the recrystallization ODFs and with more experimental data points available for calibrating the process path function.

Lastly, **Figure 14** compares the experimentally measured and simulated ODFs associated with simulation 5 in **Table 3**.

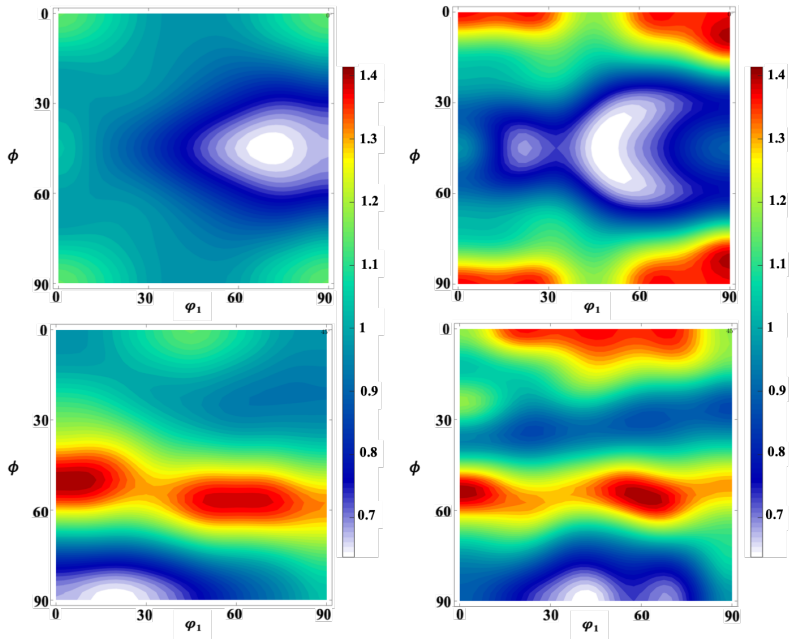

Figure 14: $\varphi_2 = 0°$ (top) and $\varphi_2 = 45°$ (bottom) sections of the experimentally measured ODF for the sample rolled to 30% reduction (left) and the simulated ODF (right) following the simulation parameters for simulation 3 in Table 3.

In **Figure 14**, both the location and intensity of the γ-fiber, as well as the location of the cube and rotated-cube components are accurately simulated when compared to the same features in the experimental ODF. While the intensity of the cube and rotated-cube components are overestimated, this simulation results in a strong representation of the accuracy of the inverse model.

It is important to note that **Figures 13** and **14** describe simulations in which both the final texture components and the simulated initial texture components were used in the calculation of the process path function. Therefore, these simulations specifically are capable of identifying the errors associated with the methods inherent in the simulation. Historically, the comparison of two ODFs has been performed qualitatively rather than quantitatively. A qualitative analysis was presented in this section and shows that the

inverse model is capable of accurately predicting the texture of the initial microstructure. In the next chapter, an avenue for a quantitative analysis for texture will be explored using the MTEX software package.

2.5 Discussion of Inverse Model Results

The results presented in section 2.4 are meant to illustrate the capabilities of the inverse model for texture prediction. These figures are used to describe the accuracy of the model and provide validation when compared to the experimentally measured ODFs. Analyses for identifying the differences between two ODFs are not a straightforward process and historically have been performed using qualitative rather than quantitative methods.

Matthies et al.[38] discussed the issue of quantitatively describing the difference between two ODFs and attempted to resolve it by defining an RP error which describes the accuracy of recalculated pole figures when compared to the original ODF. In this same vein, the MTEX package for MATLAB has developed functions which can help provide a more quantitative analysis for different ODFs. **Figures 15** and **16** illustrate the difference plots between the simulated and experimental ODFs for the simulations with the lowest error (**Figure 15**) and with the highest error (**Figure 16**). It is important to note that the difference plots were calculated by subtracting the experimentally measured ODF from the simulated ODF. Therefore the positive intensities in the difference plots are associated with overestimations while the negative intensities are associated with underestimations.

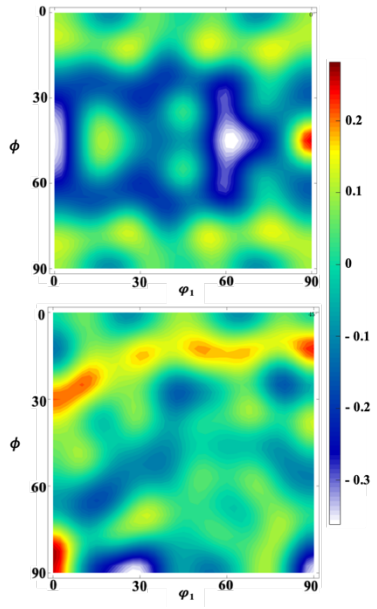

Figure 15: φ_2 = 0° (top) and φ_2 = 45° (bottom) sections of the ODF difference plot between the experimentally measured and simulated ODFs following the parameters associated with simulation 1.

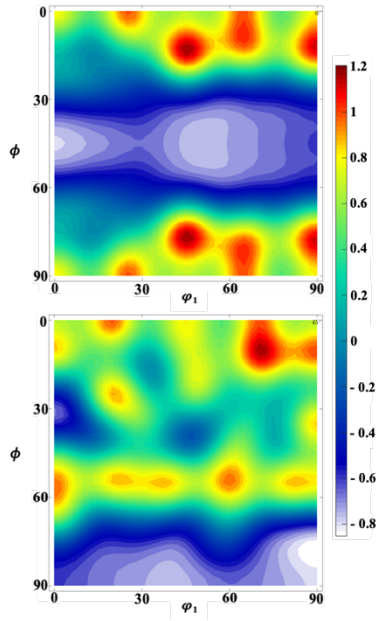

Figure 16: φ_2 = 0° (top) and φ_2 = 45° (bottom) sections of the ODF difference plot between the experimentally measured and simulated ODFs following the parameters for simulation 2.

To better understand the error associated between the simulated and experimental ODFs it may be beneficial to have a singular percentage value which can be linked to the accuracy of the model. This percentage was obtained by calculating the integrated error between the two ODFs and was calculated using the MTEX calcError function defined by equation 18.

$$error = 0.5 * \int abs(odf1 - odf2)dg \tag{18}$$

Table 4 shows the integrated error values calculated using calcError for each of the different simulations specified in **Table 3**.

Table 4: Integrated error values associated with each inverse model simulation.

Simulation	Integrated Error
Simulated 10% ODF from 40% reduced sample	4.26%
Simulated 10% ODF from 30% reduced sample	5.95%
Simulated 10% ODF from 20% reduced sample	5.34%
Simulated 20% ODF from 40% reduced sample	21.56%
Simulated 20% ODF from 30% reduced sample	7.71%
Simulated 30% ODF from 40% reduced sample	5.16%

The error analysis described in this section shows that the inverse model is capable of accurately predicting the initial ODF required to obtain a desired, final ODF when undergoing a specified deformation process.

2.6 Conclusion

An inverse model was developed and proposed which is capable of predicting the initial texture required to obtain a desired texture through processing. The model proposed is independent of material system and processing procedure and as such can be used for any polycrystalline system. This model differs slightly from the conservation of crystallites equation developed by Li et al.[31] due to its use of fast Fourier transformations, instead of generalized spherical harmonics, to describe the orientation distribution functions which results in a more efficient use of computational resources. The proposed process path function was calculated using experimental data and the simulation results for the inverse model were presented. The comparisons between the simulated and experimental ODFs show that the inverse model is capable of accurately calculating the texture of the initial microstructure. Functions developed as part of the MTEX software package were used to create difference plots and calculate the integrated error for each simulation to further illustrate this accuracy. The qualitative and quantitative error analyses show that the inverse model is accurately able to predict the initial microstructure required to obtain a known final microstructure through the hot rolling process.

The development of this model allows for the simulation of the orientation distribution function, a one-point correlation function. However, as more microstructural features become of interest, the ODF alone will be unable to contain all of the

microstructural statistics. To this end, both forward and inverse models will be presented here which utilize two-point correlation functions which allow for a much greater amount of microstructural data to be retained.

CHAPTER 3. DEFORMATION PREDICTION MODELING FOR TWO-PHASE MATERIALS: A FORWARD MODEL

3.1 Isothermal Compression and Ti-6Al-4V

Titanium and its alloys like Ti-6Al-4V are an attractive material choice in aerospace, chemical and biomedical industries due to such desirable properties like high specific strength, high corrosion resistance, biocompatibility, and ability to be used in high temperature applications[39-41]. Ti-6Al-4V is a two-phase alloy that contains a hexagonal close-packed (hcp) α-phase and a body-centered cubic (bcc) β-phase (~6 vol%) at room temperature. A coarse lamellar ($\alpha + \beta$)-colony microstructure usually prevails in castings which transforms to either fine lamellar or basket-weave (acicular α/β phases) microstructure after thermo-mechanical processing in the β-phase field, depending on the cooling rate[42,43]. Similarly, thermo-mechanical processing in the ($\alpha + \beta$)-phase field results in either completely equiaxed or bimodal (lamellar plus equiaxed α-grains) microstructures depending upon the processing conditions[44,45]. A Ti-6Al-4V alloy with nominal composition by wt% was induction skull melted in a graphite crucible at Flowserve Corporation in Dayton, Ohio. A detailed report of the composition of the as-cast material as measured using an inductively coupled plasma spectroscope can be obtained in the previous work of Roy et al[45,46].

The as-cast Ti-6Al-4V alloy was subjected to isothermal compression at a constant temperature of T = 750°C at strain rates of $10^{-3}\,s^{-1}, 10^{-2}\,s^{-1}, 10^{-1}\,s^{-1}, 1\,s^{-1}$, and $10\,s^{-1}$ up to a 50% height reduction (equivalent to a true strain of ~0.7). The compression

specimens were prepared from the as-cast ingot using electro discharge machining (EDM) in such a way that the compression axis remained parallel to the original ingot axis. The compression specimens were 9 mm in height and 6 mm in diameter prior to undergoing compression. Isothermal compression tests were carried out by Shibayan Roy and Souvik Sahoo (IIT Kharagpur) using a servo-hydraulic testing machine (DARTEC, Zwick/Roell GmbH, Germany) between two Ni-based super-alloy platens. A resistance heating split furnace with SiC heating elements was used for heating the platens and the specimens to the desired temperature (750°C). Before starting the tests, the specimens and platen were soaked for five minutes at the test temperature to ensure temperature uniformity. To confirm the temperature of the specimens, a chromel-alumel thermocouple was attached onto the specimen surface. The specimens were coated with borosilicate glass paste for lubrication against friction from the platen as well as for environmental protection (mainly for reducing Oxygen penetration and α-casing formation). Following the isothermal condition, the specimens were air-cooled to room temperature to ensure there was no significant change in the deformed microstructure (e.g. recrystallization) during cooling. Further details regarding the isothermal compression testing of Ti-6Al-4V can be obtained elsewhere[47-51].

Compression testing of any specimen generates different types of stresses (radial compressive, hoop tensile, and frictional shear) at different locations of the material[47]. As a result, the type and amount of deformation varies over the entire compression specimen, which in turn causes microstructural variation in different locations. Pure radial compressive stresses only prevail at the mid-thickness region of the compression specimen as shown in **Figure 17**. Therefore, to characterize the deformation microstructure formed

from pure compressive stresses the specimen was sectioned by IIT Kharagpur along the diameter in the z-direction (parallel to the compression direction). SEM observations were then made from the regions along the equatorial plane as shown in **Figure 17**. For this, the observation surface was polished by a standard metallographic technique using SiC emery papers up to 2000 grit, followed by polishing with diamond suspensions of 1μm and 0.25μm particle sizes. The polished surfaces were etched for 10 seconds using Kroll's reagent (2% HF + 6%HNO_3 + 92% distilled water). Microstructural observations from the various compressed specimens deformed at different strain rates were made by scanning electron microscope (Zeiss, Germany) in back scattered mode. More details regarding the sectioning of the compression specimens for microstructural characterization can be obtained elsewhere[47,50].

In an effort to cover a larger microstructure area, thereby increasing the statistical significance of the two-point statistics measured from the microstructural dataset, macro-montages were also created by stitching several SEM images captured via sequential, regulated, and controlled movement of the SEM stage in horizontal and vertical directions[45]. For each of the deformation conditions, two SEM macro-montages were made by stitching four SEM images taken in a 2x2 matrix. For the as-cast alloy, the SEM montage was the same as the montage shown by Roy et al[45].

The as-cast alloy was heat treated in a muffle furnace for five minutes at 750°C at a heating rate (5°C/min) identical to the split furnace (used in the compression tests) in an effort to produce the as-heated microstructure immediately before the tests were conducted. The heat treated specimen was then water quenched to preserve the high temperature microstructure with the exact α- and β-phase fraction before the compression tests. The

observation surface for SEM characterization was prepared following the standard metallographic preparation and etching as detailed above. The observation surface was chosen with the ingot axis (and in turn the compression axis) being parallel to it. This further ensures that the observation surfaces for the as-heated specimen and compression tested specimens are selected from identical locations in the original ingot.

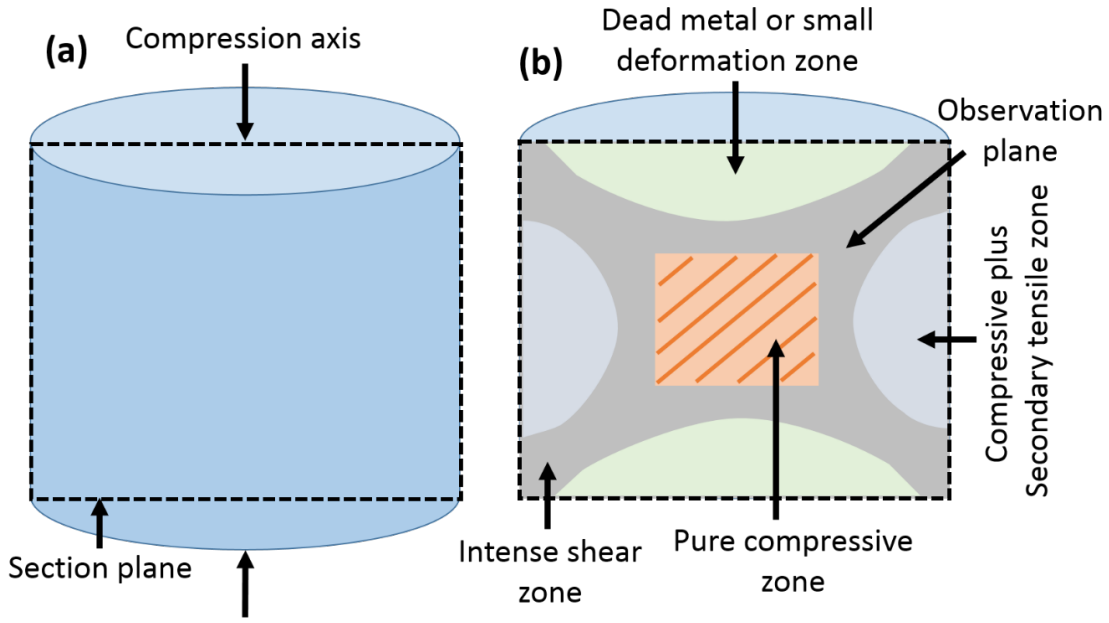

Figure 17: Schematic of (a) un-deformed compression specimens, and (b) sectioning scheme for microstructural characterization of compression tested specimen showing regions of different stresses. The hatched region at the mid-thickness, equatorial region represents the location for pure compressive stress (provided by Dr. Shibayan Roy, IITK).

A heat treated and water quenched Ti-6Al-4V alloy (**Figure 18**) shows a continuous grain boundary (GB) α-phase along prior β GB in the microstructure. In addition, lamellar α-phase nucleates beside the GB α-phase and grows inside the prior β grain. The remnant β-phase remains as thin lamellae between adjacent α lamella and forms an $(\alpha + \beta)$-colony microstructure[45]. After isothermal compression, most of these lamellar $(\alpha + \beta)$ colonies

straighten along the direction of hoop tensile stresses (perpendicular to the compression axis). Some of the ($\alpha + \beta$) colonies, plus the corresponding GB α-phase, which seem to be originally parallel to the compression axis show a kinked or bent morphology.

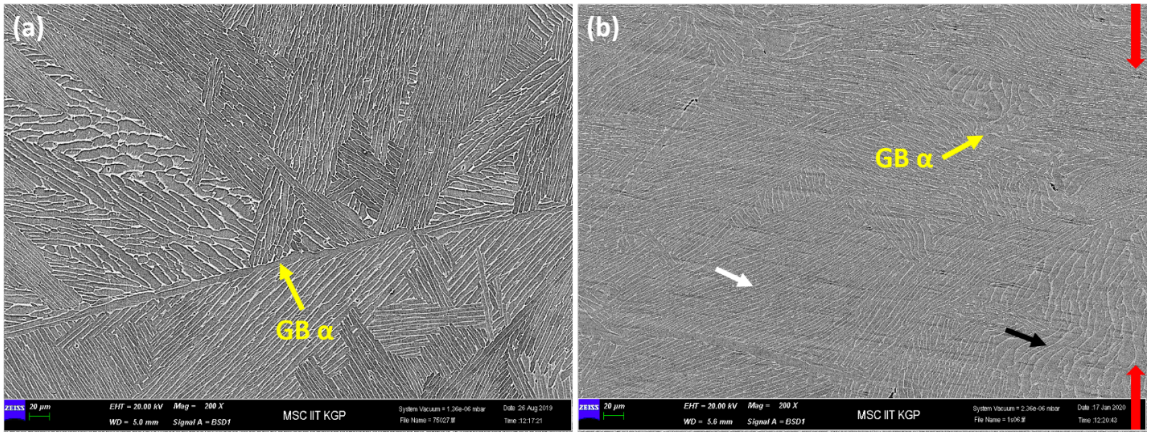

Figure 18: SEM images showing the microstructure of Ti-6Al-4V alloy in (a) heat treated and water quenched and (b) deformed (true strain rate 1 s-1) conditions. Compression direction is vertical and shown by the red arrow in (b). Important microstructural features are indicated in the respective micrographs. In (b), black and white arrows indicate kinked and straight lamellar ($\alpha + \beta$) colonies, respectively (provided by Dr. Shibayan Roy, IITK).

3.2 Statistical Continuum Theory

The model pursued here utilizes statistical continuum theory practices proposed by Garmestani et al.[52] to predict the microstructural evolution during deformation through the evolution of two-point statistics. In their work, Garmestani et al.[52] began with a power law steady-state creep equation for each phase that was first introduced by Hutchinson[53]. From this power law equation the Cauchy stress tensor was defined by equation 19.

$$T_{ij} = N_{ijkl} D_{kl} - p\delta_{ij} \tag{19}$$

In equation 19, N_{ijkl} is the fourth rank symmetric inelastic modulus tensor, D_{kl} is the strain rate tensor, and p is the hydrostatic pressure. Garmestani et al.[52] then introduced the velocity gradient, L_{kl}, which can be decomposed into the strain rate tensor and the rotation rate tensor, W_{kl}, as shown by equation 20.

$$L_{kl} = D_{kl} + W_{kl} \tag{20}$$

In this model, the rotation rate tensor is zero since the crystallographic orientation is not considered. Thus, equations for the calculation of the local velocity gradient of each phase are identified as equation 21 and equation 22.

$$\langle L^0(r)\rangle_{h_1} = \bar{L} + G(r-r') * \langle \widetilde{N}\big(L, h(r')\big)\rangle_{h_1}\bar{L} \tag{21}$$

$$\langle L^0(r)\rangle_{h_2} = \bar{L} + G(r-r') * \langle \widetilde{N}\big(L, h(r')\big)\rangle_{h_2}\bar{L} \tag{22}$$

In equations 21 and 22, $\langle L^0(r)\rangle_{h_1}$ and $\langle L^0(r)\rangle_{h_2}$ are the local velocity gradients for phase h_1 and phase h_2 respectively, $G(r-r')$ is the Green's function solution, $\bar{L}$ is the macroscopic homogeneous velocity gradient, and $\langle \widetilde{N}\big(L, h(r')\big)\rangle_{h_1}$and $\langle \widetilde{N}\big(L, h(r')\big)\rangle_{h_2}$ are the ensemble average of the polarized modulus for the velocity gradient, L, according to phase h for phases h_1 and h_2 respectively. The terms $\langle \widetilde{N}\big(L, h(r')\big)\rangle_{h_1}$and $\langle \widetilde{N}\big(L, h(r')\big)\rangle_{h_2}$ are calculated using equation 23 and equation 24.

$$\langle \widetilde{N}\big(L, h(r')\big)\rangle_{h_1} = f(r' \in h_1 \,|r \in h_1)\widetilde{N}^1(\bar{L}) + f(r' \in h_2 \,|r \in h_1)\widetilde{N}^2(\bar{L}) \tag{23}$$

$$\langle \widetilde{N}\big(L, h(r')\big)\rangle_{h_2} = f(r' \in h_1 \,|r \in h_2)\widetilde{N}^1(\bar{L}) + f(r' \in h_2 \,|r \in h_2)\widetilde{N}^2(\bar{L}) \tag{24}$$

In equations 23 and 24, $\widetilde{N}^1(\bar{L})$ and $\widetilde{N}^2(\bar{L})$ are the spatially dependent inelastic modulus for phase 1 and phase 2 respectively, and the terms of the form $f(r'\epsilon\, h_i \mid r\, \epsilon\, h_j)$ are the two-point statistics for the two phase material. In this work, phase 1 corresponds to the Ti-6Al-4V α-phase and phase 2 corresponds to the β-phase. **Figure 19** shows a microstructural image obtained using a scanning electron microscope (SEM) and the corresponding two-point statistics. Such SEM images are used to obtain the two-point statistics of the compression samples for comparison to the two-point statistics simulated using the pursued evolution model.

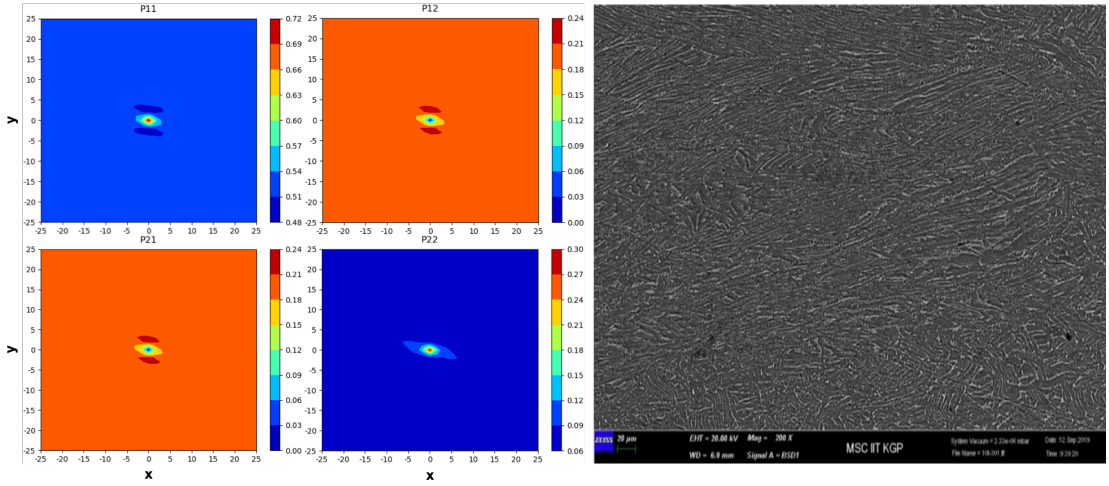

Figure 19: SEM image and corresponding two-point statistics of specimen deformed at strain rate of 10^{-3} s^{-1}.

Six SEM images were obtained for each of the isothermal compression conditions representing the deformation microstructures while ten SEM images were obtained from the undeformed as-heated specimen. The two-point statistics were calculated from each of these SEM images and averaged over the six SEM images for any given deformation condition or the ten SEM images for the as-heated material. This was performed using the open source pyMKS package developed by Kalidindi et al[54]. The averaged two-point

statistics were then used to calculate the local velocity gradients of each phase as described in equations 21-24. From the local velocity gradients, Lin et al.[55] show that the two-point statistics can be evolved using the parameters described in **Figure 20**.

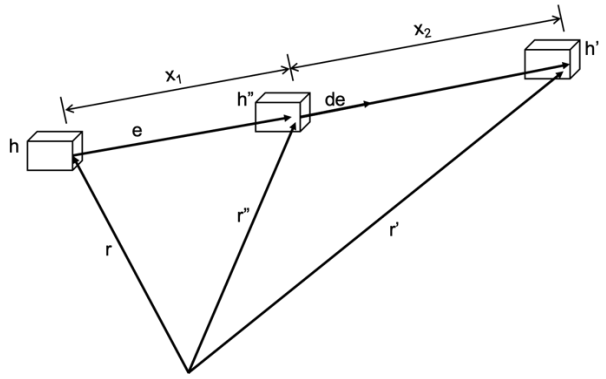

Figure 20: Definition of the evolution equation parameters from Lin et al. [55]

In **Figure 20**, r, r', and r" are vectors associated with the two-point statistics and e is a vector that originates from state h and terminates at state h'. The magnitudes of r, r', and r" each ranged from 0 (a single point) to 100 pixels. From this, Lin et al.[55] describe the rate of change of the deformation vector, e, using the equation 25.

$$\langle \dot{e} \rangle_{h,h'} = \int \langle L(r") \rangle_{h,h'} \, de \tag{25}$$

In equation 25, $\langle \dot{e} \rangle_{h,h'}$ is the rate of change of e and $\langle L(r") \rangle_{h,h'}$ is the local strain rate tensor for the vector r". The term $\langle L(r") \rangle_{h,h'}$ is calculated using equation 26.

$$\langle L(r") \rangle_{h,h'} = \int f_3(h", r" \mid h', r', h, r) \, \langle L(r") \rangle_{h"} \, dh" \tag{26}$$

In equation 26, $\langle L(r")\rangle_{h"}$ is the local strain rate for the vector $r"$ and phase $h"$ and $f_3(h", r" \mid h', r', h, r)$ is the three-point probability function where $r"$ belongs to the state $h"$, r' belongs to state h', and r belongs to state h. Equation 26 is then integrated to obtain equation 27.

$$\langle L(r")\rangle_{h,h'} = f_3(h_1, r" \mid h', r', h, r)\langle L(r")\rangle_{h_1} + f_3(h_2, r" \mid h', r', h, r)\langle L(r")\rangle_{h_2} \quad (27)$$

In equation 27, $f_3(h_1, r" \mid h', r', h, r)$ and $f_3(h_2, r" \mid h', r', h, r)$ are the three-point statistics where $r"$ is associated with phase h_1 (α-phase) and h_2 (β-phase) respectively. The three-point probability function was approximated using the two-point probability function with equation 28.

$$f_3(h", r" \mid h', r', h, r) \cong \frac{x_1}{x_1 + x_2} f_2(h", r" \mid h', r') + \frac{x_2}{x_1 + x_2} f_2(h", r" \mid h, r) \quad (28)$$

Here, x_1 and x_2 are equal to $|r" - r|$ and $|r" - r'|$ respectively. Furthermore, $\langle \dot{e} \rangle_{h,h'}$ can be integrated with respect to time as shown in equation 29 to identify the deformation, $\langle \Delta e \rangle_{h,h'}$.

$$\langle \Delta e \rangle_{h,h'} = \int_0^t \langle \dot{e} \rangle_{h,h'} dt \quad (29)$$

Lin et al.[55] showed that using this formulation allowed for the prediction of the evolution of two-point statistics in a single direction (e.g. a singular value of theta). To do this, Lin et al.[55] used this formulation to calculate the deformation using equation 29 and then added the deformation to the original vector lengths. In addition, Lin et al.[55] employed

the use of Corson's equation and calculated new values for the parameters c_{ij} and n_{ij} while assuming that the probabilities remain constant but their associated r value changes according to the deformation described by equation 2. From here, the model is expanded to describe the full map of the two-point statistics (i.e. all values of theta). The results shown here will model the deformation of all theta angles of two-point statistics for isothermal compression of a Ti-6Al-4V alloy at T = 750°C and strain rate $\dot{\varepsilon}$ = 10^{-3} s^{-1}, 10^{-2} s^{-1}, 10^{-1} s^{-1}, 1 s, 10 s^{-1}.

3.3 Two-Phase Two-Point Statistics Simulation Results

The results presented here encompass two different simulation types which are utilized to validate the proposed statistical model. Each simulation type utilizes the same deformed specimens. However, the method for obtaining the SEM images changes between the two types. The first method of validation uses six individual images for each sample, for which the two-point statistics were calculated for each image and then averaged over all images. **Figure 22** illustrates the two-point statistics calculated from the SEM images representing the microstructure of the as-heated specimen. Also shown is the representative SEM image for this deformation condition which was used to calculate the two-point statistics.

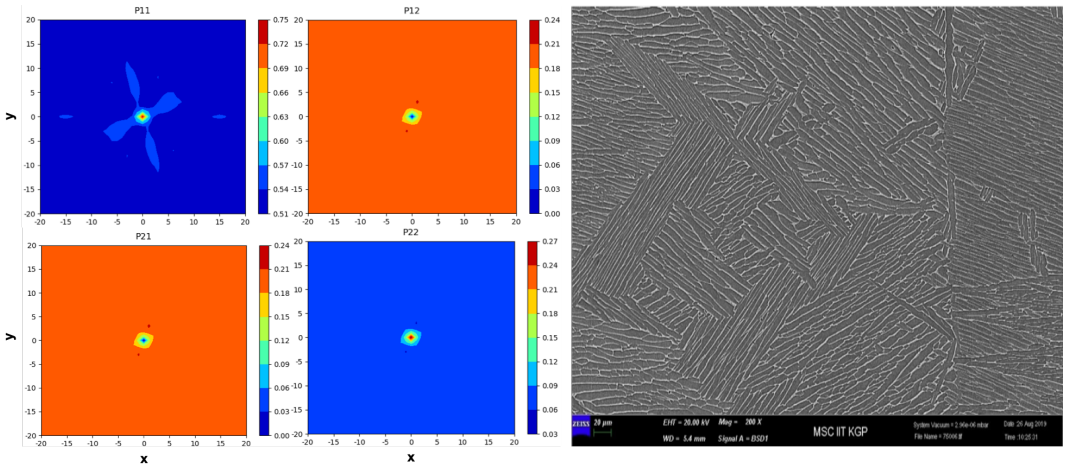

Figure 21: Two-point statistic plots for P11, P12, P21 and P22 matrix component and the corresponding SEM image obtained from the as-heated specimen.

Meanwhile, **Figures 22** and **23** compare the experimentally calculated P11 and P22 statistics from the deformed microstructure of the specimens compressed at different strain rates to the simulated two-point statistics. Each simulation was performed over a range of magnitudes for r from 0 to 100 pixels. However, for ease of viewing the plots of the two-point statistics results are focused on the central peak.

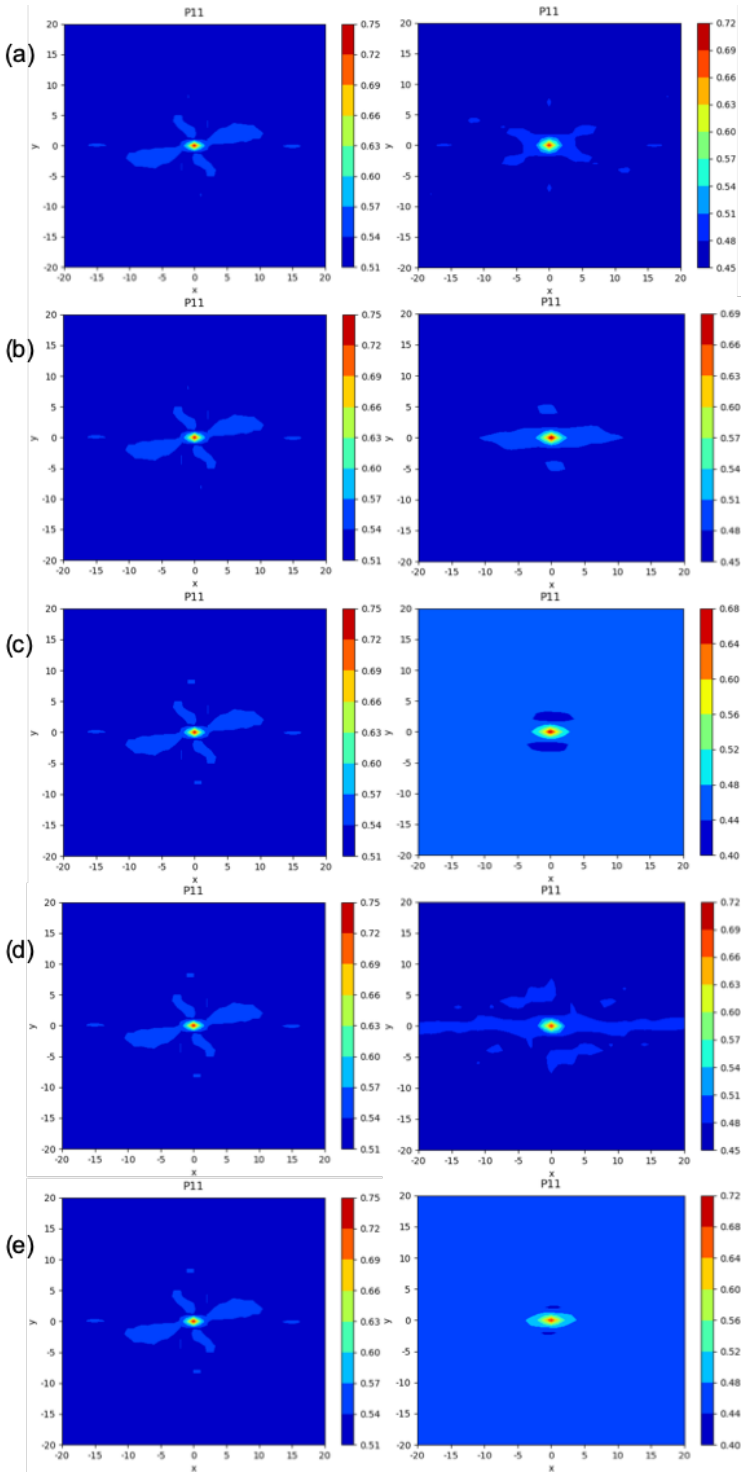

Figure 22: Comparison of the simulated (left) and experimental (right) P11 statistics from the deformed microstructures for each of the specimens compressed at different strain rates of (a) 10^{-3} s^{-1} (b) 10^{-2} s^{-1} (c) 10^{-1} s^{-1} (d) 1 s^{-1} (e) 10 s^{-1}.

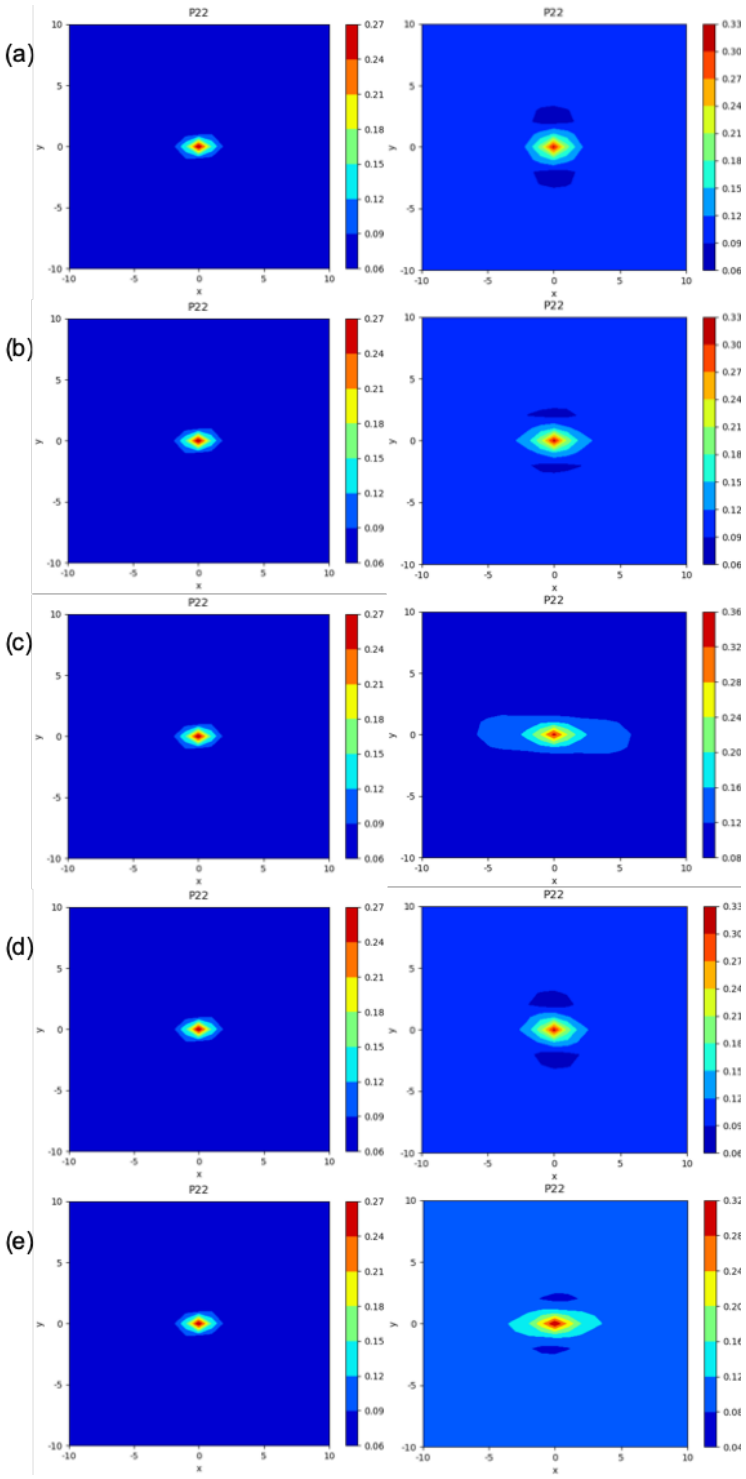

Figure 23: Comparison of the simulated (left) and experimental (right) P22 statistics from the deformed microstructures for each of the specimens compressed at different strain rates of (a) 10^{-3} s^{-1} (b) 10^{-2} s^{-1} (c) 10^{-1} s^{-1} (d) 1 s^{-1} (e) 10 s^{-1}.

In **Figure 22**, the simulated P11 statistics seem to underestimate the deformation that corresponds to the tendril-like arms of the central peak. These arms correspond to the average orientation of the α-phase grains in the SEM images. The visual difference between the simulated central peak and the experimental peaks could be due to the initial statistics. This is due to the fact that the initial statistics define the starting condition for the deformation microstructure. Therefore if the initial statistics are not representative of the entire microstructure, the simulated two-point statistics will be inaccurate. Meanwhile, **Figure 23** shows that for the P22 statistics, the statistical model is able to accurately predict the deformation microstructure. Interestingly, the largest difference between the experimental and simulated two-point statistics for both P11 and P22 is found on the north side of the central peak where the y values are positive. The deformation associated with this area of the central peak is associated with the compression of the z-axis of the sample. Therefore, this error leads to the expectation that compression, which results in a negative value for deformation, is harder to predict than tensile deformation. However, this error is not seen in the south side of the central peak (where y values are negative) which is also associated with the compression of the z-axis. Thus, it is expected that the compression error is associated with difficulties in the algorithm which recalculates the deformed two-point statistics rather than the methodology for the prediction of deformation. Furthermore, it is important to note that the model is heavily dependent on the statistics obtained for the initial microstructure. This is to say that if the initial statistics do not accurately represent the microstructure of the undeformed material then the model results will not be accurate. To quantify the importance of the initial statistics the same simulations were performed using the SEM montage images.

3.3.1 The Effect of Microstructural Statistics

The second form of validation for the proposed model focuses on recognizing that the statistics obtained are representative of the entire microstructure. This was done by calculating the two-point statistics using the large area montage of SEM images for each of the compression conditions. Confirming that the two-point statistics are representative of the entire microstructure in the compression specimens is important because it validates that the model is capable of predicting microscale evolutions, and that the previous increases in error were most likely due to non-representative statistics. To this end, SEM montages similar to the one shown in **Figure 21** were created for each of the specimens compressed at different strain rates ($\dot{\varepsilon}$ = 10^{-3} s^{-1}, 10^{-2} s^{-1}, 10^{-1} s^{-1}, 1 s^{-1} and 10 s^{-1}) and used to calculate the two-point statistics. One such SEM montage is shown in **Figure 24** for the specimen compressed at 1 s^{-1} strain rate. It is important to note that the individual images comprising the montages were obtained at the same magnification and resolution as the single SEM images (shown in **Figure 21**). This procedure simultaneously maintains high resolution for grain identification and covers a large microstructural area to facilitate the calculation of the two-point statistics with adequate statistical reliability. Keeping the magnification and resolution constant between the montages and the single SEM images allows for the comparison of the two-point statistics obtained from these two different approaches.

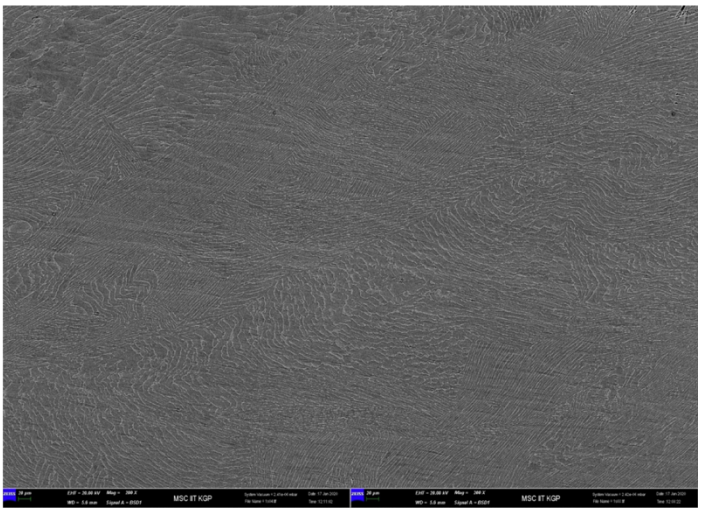

Figure 24: Stitched scanning electron micrograph for the specimen deformed at strain rate of $1s^{-1}$.

Similar to the previous approach of calculating the two-point statistics from the single SEM images, the two-point statistics for each of the SEM montages were averaged between the two such montages for each of the deformed specimens. In **Figures 25** and **26**, the experimentally calculated (from SEM montages) and simulated two-point statistics are compared for each of the deformed specimens.

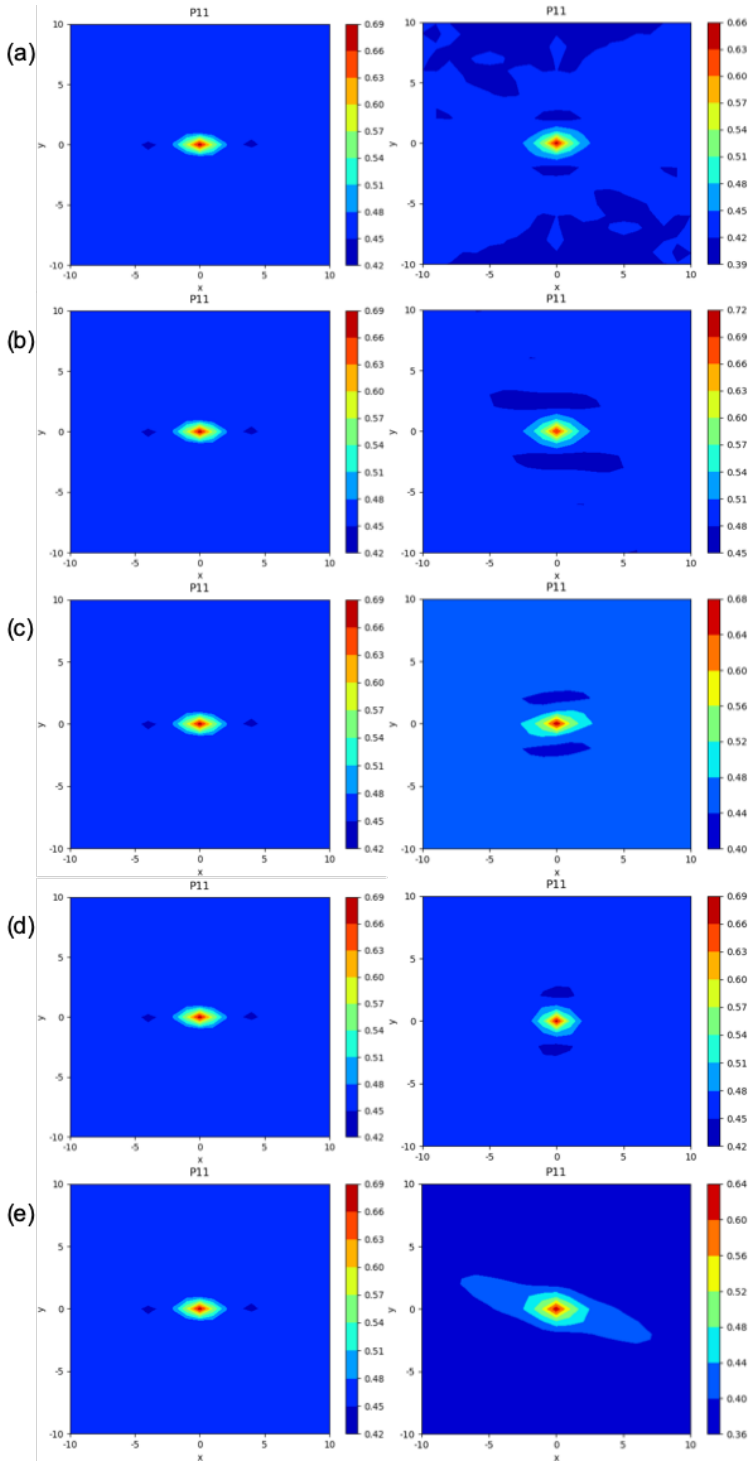

Figure 25: Comparison of the simulated (left) and experimental (right) P11 statistics for the deformed microstructures for each of the specimens compressed at different strain rates of (a) 10^{-3} s^{-1} (b) 10^{-2} s^{-1} (c) 10^{-1} s^{-1} (d) 1 s^{-1} (e) 10 s^{-1}

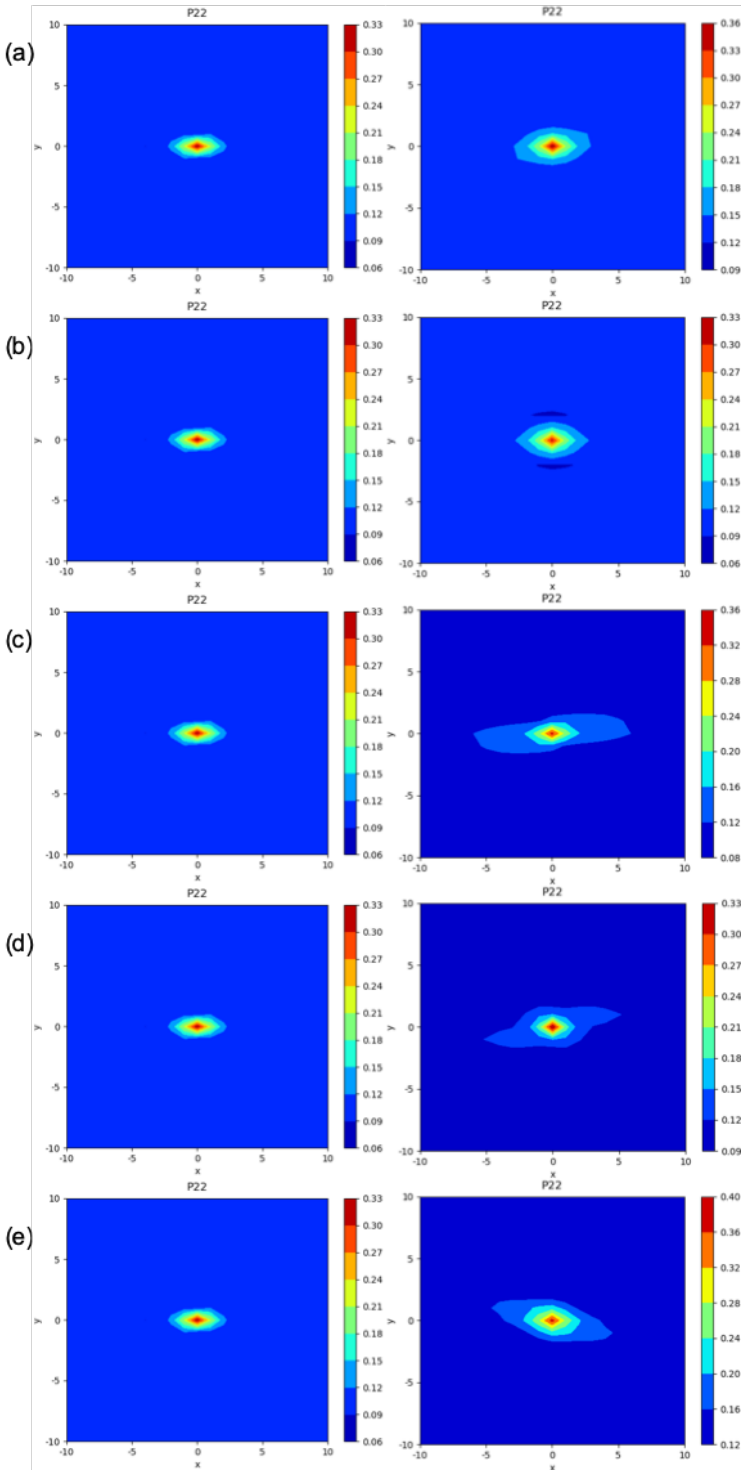

Figure 26: Comparison of the simulated (left) and experimental (right) P22 statistics for the deformed microstructures for each of the specimens compressed at different strain rates of (a) 10^{-3} s^{-1} (b) 10^{-2} s^{-1} (c) 10^{-1} s^{-1} (d) 1 s^{-1} (e) 10 s^{-1}.

As with **Figures 22** and **23**, **Figures 25** and **26** also illustrate the suitability of the proposed model to accurately predict the two-point statistics of the deformed microstructure. However, unlike the simulations in **Figures 22** and **23** any errors associated with the volume fraction calculation are no longer present. This illustrates the importance of obtaining statistics that are representative of the entire microstructure of the compression tested specimens. In the next section a quantitative error analysis will be performed to highlight the capabilities of the model.

3.4 Discussion

In section 3, **Figures 22** and **23** as well as **Figures 25** and **26** illustrate the ability of the proposed statistical model to predict the deformation microstructure caused by the isothermal compression process. The error between the simulated and experimental statistics are plotted in **Figures 27** and **28** illustrating the errors associated with the individual SEM images as well as the SEM montages, respectively, for the specimen compression tested at a strain rate of 10^{-2} s^{-1} simulations.

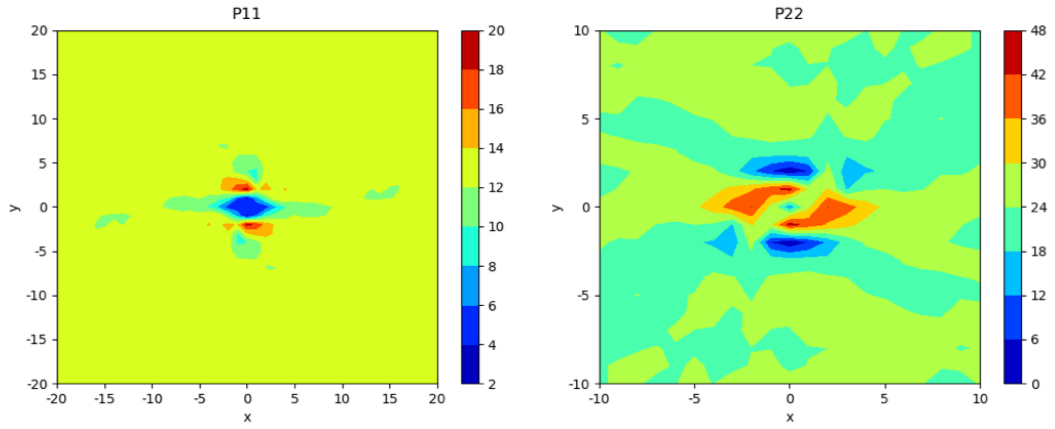

Figure 27: P11 (left) and P22 (right) error plots for the simulation of the deformation microstructure for the specimen compression tested at a strain rate of 10^{-2} s^{-1} based on the two-point statistics obtained from the single SEM images.

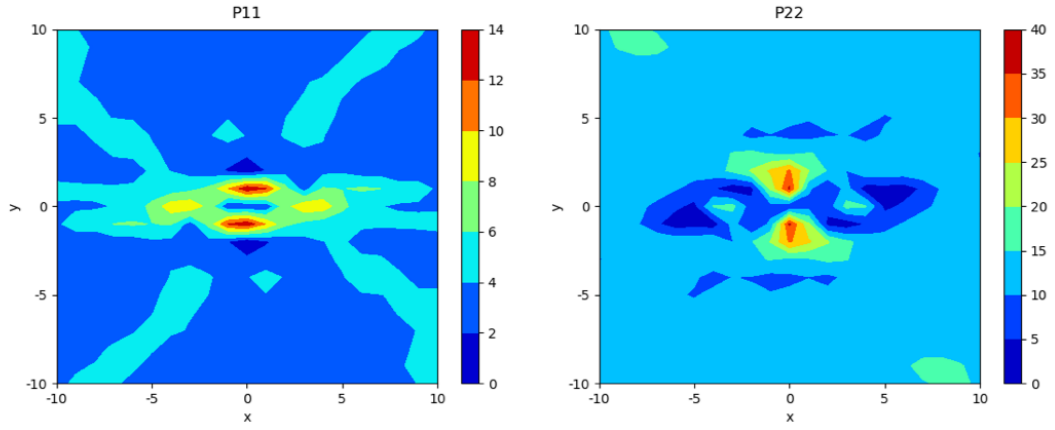

Figure 28: P11 (left) and P22 (right) error plots for the simulation of the deformation microstructure for the specimen compression tested at a strain rate of 10^{-2} s^{-1} based on the two-point statistics obtained from the SEM montage images.

From **Figures 27** and **28**, it can be seen that the maximum error is consistently associated with the centralized peak. It is expected that this error can be attributed to the difficulty of the model in the calculation of deformation caused by compression. Furthermore, as the points get farther away from the centralized peak in **Figures 27** and **28** the error decreases. It is important to note that the error associated with these points for **Figure 27** are larger

than those of **Figure 28** and are closely linked to the volume fraction difference between the experimental and simulated statistics. Therefore, since the SEM montage images were more accurate in the calculation of volume fraction the error associated with these points is lower than for the individual SEM images. Also, in both **Figure 27** and **Figure 28** the largest maximum error (as well as largest average error) is associated with the P22 statistics. This is expected to be due to the relatively lower volume fraction of the β phase which could lead to greater difficulty in obtaining representative statistics for this phase.

Tables 5 and **6** identify the average error across all values for P11 and P22 for both the single SEM images and SEM montages, respectively. These average errors provide a more concrete description of the errors associated with each imaging technique. As such they are able to illustrate the importance of representative statistics while also describing the accuracy of the statistical deformation model.

Table 5: Calculated errors associated with the two-point statistics simulations using single SEM images.

Strain Rate	Average P11 Error (%)	Average P12 Error (%)	Average P21 Error (%)	Average P22 Error (%)
10^{-3} s^{-1}	12.22	9.35	9.35	21.74
10^{-2} s^{-1}	12.37	8.36	8.37	23.98
10^{-1} s^{-1}	20.51	12.46	12.45	33.95
1 s^{-1}	12.21	8.69	8.67	23.77
10 s^{-1}	15.35	10.17	10.18	26.93

Table 6: Calculated errors associated with the two-point statistics simulations using SEM montages.

Strain Rate	Average P11 Error (%)	Average P12 Error (%)	Average P21 Error (%)	Average P22 Error (%)
10^{-3} s^{-1}	9.58	4.67	4.66	17.46
10^{-2} s^{-1}	3.90	2.78	2.78	12.16
10^{-1} s^{-1}	3.45	3.01	2.97	5.31
1 s^{-1}	2.26	2.49	2.45	2.97
10 s^{-1}	17.27	8.36	9.37	23.84

Tables 5 and **6** show that the average simulation error ranges from 7.41% to 33.71% for the single SEM images and 1.72% to 22.89% for the SEM montages. What is interesting is that even for the individual SEM images the average error is low. This is interesting because it means that while the volume fraction is different, the shape of the two-point statistics is similar. Furthermore, the large discrepancy between the average errors of the individual images and the montage images shows the importance of obtaining enough statistics to be representative of the entire microstructure. **Tables 5** and **6** also show that there is a decrease in error with an increase in strain rate. This trend is seen up to the 1 s^{-1} strain rate condition. The high error associated with the simulation of the 10^{-3} s^{-1} strain rate when compared to the 10^{-1} s^{-1} or 1 s^{-1} strain rates can be attributed to the high temperature associated with the isothermal compression tests. This can be attributed to the

high temperature associated with the isothermal compression tests. The low strain rate of 10^{-3} s^{-1} means that the total test time was ten times higher than when the test was performed at a strain rate of 10^{-2} s^{-1}. This longer test duration at lower strain rate could result in some recovery processes (cross slip or climb) to occur in the deformation microstructure. This is also evident in Roy et al.[47,48] from the true stress – true strain curves presented for these conditions (T = 750°C, $\dot{\varepsilon} = 10^{-3}$ s^{-1} and 10^{-2} s^{-1}). This recovery process cannot be accounted for in the model. Therefore, the error associated with simulations of the deformation microstructure with this recovery process (lower strain rates) would undoubtedly be higher than for simulations considering deformation microstructures without recovery (higher strain rates).

3.5 Conclusions

In chapter 2 an inverse model for the prediction of crystallographic orientation was proposed and its results presented. This inverse model utilized the one-point correlation function called the ODF to define the microstructure features of interest. To provide more microstructural feature information, two-point statistics were used which allow for the description of such features as average grain morphology, average grain size, and phase distribution. These two-point statistics were applied to a Ti-6Al-4V alloy undergoing isothermal compression, and a statistical model was developed and proposed which allows for the evolution of the two-point statistics to predict the microstructure evolution of the Ti-6Al-4V alloy. The simulation results were presented and an error analysis was performed which suggests that the statistical model proposed here is capable of accurately predicting the evolution of the two-point statistics. With the development of a forward model for the prediction of the evolution of two-point statistics, an inverse model, similar

to the one developed in chapter 2, will be presented for the optimization of two-point statistics during processing.

CHAPTER 4. DEFORMATION PREDICTION MODELING FOR TWO-PHASE MATERIALS: AN INVERSE MODEL

4.1 Introduction

In chapter 3, a model was proposed which models the evolution of a two-phase material through the use of two-point statistics. This model was validated for multiple strain rates for the application of isothermal compression in the dual phase Ti-6Al-4V alloy. In this chapter, an inverse model will be presented which is capable of predicting the initial microstructure required to obtain a desired final microstructure using the two-point statistics simulated by the forward model.

4.1.1 Microstructure Hull and Two-Point Statistics

In materials science there is a theory that states that all material microstructures, when a feature is identified, can be described in a single space. This space is termed the microstructure hull, and is defined to be the space where each point corresponds to a different microstructure. The microstructure hull can be either one-dimensional or multi-dimensional and is dependent on the microstructural feature of interest. For example, for a two-phase material in which the volume fraction of the phases is the only microstructure characteristic of interest, the microstructure hull is the number line from 0 to 1 which describes the volume fraction of one of the two phases. This two-phase example is the simplest form of the microstructure hull as it requires only a single number to define the entire microstructure. However, microstructure hulls can become multi-dimensional and very complex in their portrayal of the microstructural statistics.

The orientation distribution function for a polycrystalline material can be used to define a material's microstructure, and therefore is capable of being defined using a microstructure hull. This has been illustrated in previous research[56,57] and the full microstructure hull for polycrystalline cubic-orthorhombic materials was simulated by Fullwood et al.[58] in 2010. The microstructure hulls for polycrystalline materials are specified using the texture coefficients defined in chapter 2. **Figure 29** illustrates the simulated microstructure hull for cubic-orthorhombic materials as created by Fullwood et al.[58]

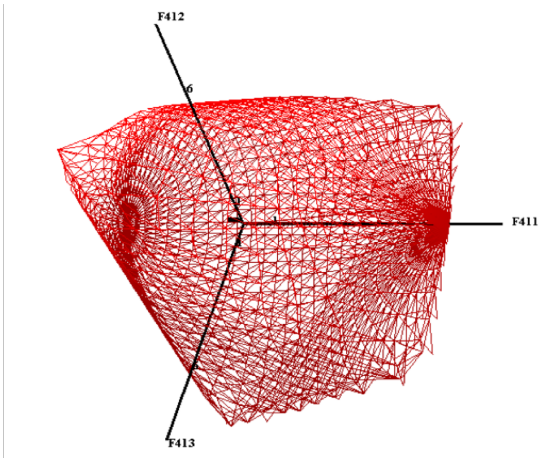

Figure 29: The simulated microstructure hull for cubic-orthorhombic materials created by Fullwood et al.[58]

The microstructure hull for polycrystalline materials uses the F_4^{11}, F_4^{12}, and F_4^{13} texture coefficients to define the ODF. Since the texture coefficients vary from one ODF to another, each point in this microstructure hull corresponds to a different ODF and a different microstructure. Since each point in a microstructure hull corresponds to a different microstructure, the evolution of microstructure can be seen as a "path" which can be followed which connects individual points on the microstructure hull. In **Figure 29**, each parallel set of red lines is a different path which evolves the cubic-orthorhombic

material from one microstructure to another. The inverse model for the evolution of two-point statistics developed here attempts to identify the specific path in order to predict the initial microstructure required to obtain a desired final microstructure.

4.2 Inverse Model Theory

The development of the inverse model for two-point statistics follows a similar description as the conservation of crystallites. The theory behind this approach follows that for any processing procedure which contains only strain-based deformation the microstructure evolution can be discretized based on strain. Using the microstructure hull description in section 4.1, this would result in following a single line from point to point across the microstructure hull. The conservation of crystallites equation in chapter 2 models the line through the microstructure hull using the process path function. Thus, by using the conservation of crystallites equation for the two-point statistics instead of the texture coefficients, the process path function calculated will correspond to the evolution of the two-point statistics. Equations 30 through 33 below describe the four conservation of crystallites equations which, as a whole, define the inverse model for two-point statistics.

$$f_f(h_1, h_1, \vec{r}) = e^{A_{11}(\eta-\eta_0)} f_0(h_1, h_1, \vec{r}) \tag{30}$$

$$f_f(h_1, h_2, \vec{r}) = e^{A_{12}(\eta-\eta_0)} f_0(h_1, h_2, \vec{r}) \tag{31}$$

$$f_f(h_2, h_1, \vec{r}) = e^{A_{21}(\eta-\eta_0)} f_0(h_2, h_1, \vec{r}) \tag{32}$$

$$f_f(h_2, h_2, \vec{r}) = e^{A_{22}(\eta-\eta_0)} f_0(h_2, h_2, \vec{r}) \tag{33}$$

In equations 30 through 33 the $f_f(h_i, h_j, \vec{r})$ terms correspond to the two-point statistics of the final microstructure while the $f_0(h_i, h_j, \vec{r})$ terms correspond to the two-point statistics of the initial microstructure. The A_{ij} terms also correspond to the process path functions associated with each calculation. It is important to note that in order to retain a greater accuracy the process path function was defined separately for each set of two-point statistics. This means that four different path functions were calculated for the P11, P12, P21 and P22 statistics independently of the other functions. It is also important to note that this model was not mathematically derived from the creation of the microstructure hull for two-point statistics. Therefore, this form may not be the form that yields the highest accuracy. However, it is the goal of this model to show that it is possible to create an invertible experimentally driven model which is capable of predicting the two-point statistics of the initial microstructure required to obtain a final desired microstructure.

4.3 Simulation Results

4.3.1 Calibration of the Inverse Model and Ti-6Al-4V Results

The forward model developed in chapter 3 was used to provide data which used to calibrate the process path function of the inverse model. The forward model was run using the same SEM images of the initial Ti-6Al-4V microstructure used in chapter 3. **Figure 30** shows a single SEM of the as-heated Ti-6Al-4V microstructure while **Figure 31** illustrates the two-point autocorrelation of the black (α) phase.

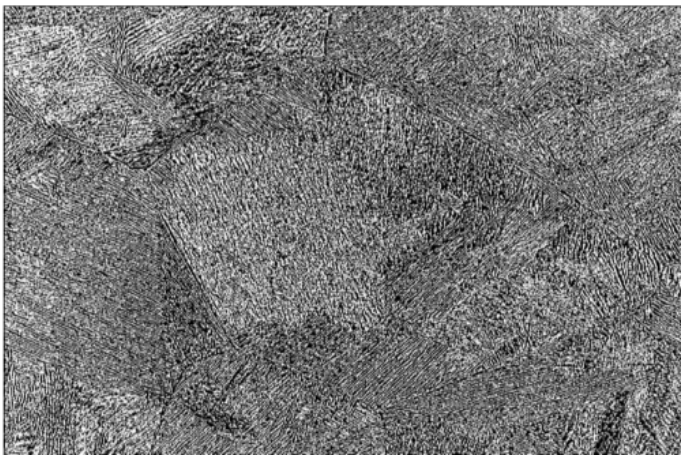

Figure 30: Black & white large area image of the as-heated Ti-6Al-4V initial microstructure in chapter 3.

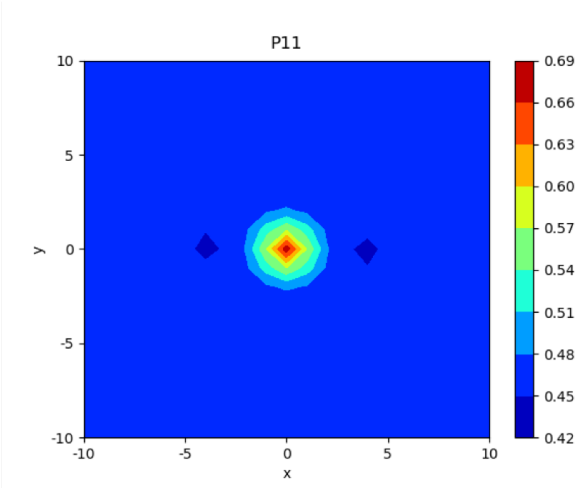

Figure 31: Autocorrelations of the black (alpha) phase for each of the initial microstructures in Figure 30.

The two-point statistics of the initial microstructure were evolved using the forward model, the strain rate tensor associated with compression, and the inverse strain rate sensitivity parameters associated with the alpha and beta phases of Ti-6Al-4V (1.13 & 3.6 respectively[59]). The initial microstructure was evolved to a strain ranging from 0% to 100% at steps of 1% using a strain rate of 10 s^{-1}. The two-point statistics of the Ti-6Al-4V microstructures at strains of 0%, 20%, 40%, 60%, 80% and 100% true strain were used to

calibrate the inverse model. The calibration was performed in a multi-step process between each set of consecutive strains in a similar approach to the calibration performed in chapter 2. The generalized process path function was then saved and used in the inverse calculations to predict the initial microstructure required to obtain a desired final microstructure through compression.

A large number of simulations were systematically performed in order to illustrate the capabilities of the inverse model, after being calibrated using the data obtained from the forward model. **Figure 32** plots the strain of the desired final microstructure versus the strain of the required initial microstructure. Therefore, this figure illustrates all possible simulations that can be performed using this inverse model. This plot does not take into account material system or processing condition and, therefore, is a generic plot for all materials.

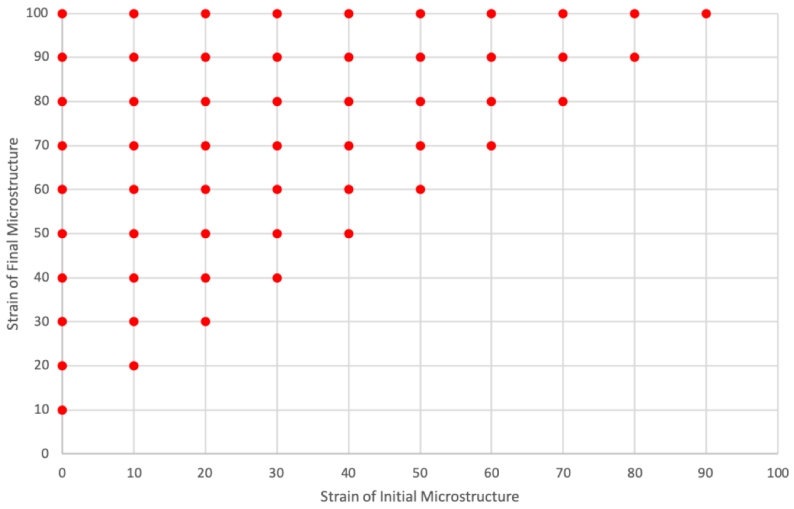

Figure 32: All possible permutations of the strains associated with a desired final microstructure and a required initial microstructure.

In **Figure 32** the red dots correspond to simulations which were performed as part of the validation of the inverse model. Furthermore, since strain cannot be reduced by actively deforming a specimen (i.e. a 50% height-reduced specimen cannot become a 30% height-reduced specimen through further compression) any simulation permutation for which the initial strain is larger than the final strain is considered to be an impossible and unrealistic simulation. Each of the simulations described by the red dots in **Figure 32** can be found in **Appendix A,** including a table of the model parameters for each simulation performed in this study.

For ease of presentation not all of the simulations are shown here. Four separate inverse model simulations were chosen, which are described in **Table 7** below.

Table 7: Model parameters for the inverse simulations described in Figures 33 and 34.

Simulation ID	Strain of Final Microstructure	$(\eta - \eta_0)$	Strain of Initial Microstructure
1	60%	(60 – 40) = 20	40%
2	70%	(70 – 20) = 50	20%
3	90%	(90 – 70) = 20	70%
4	100%	(100 – 0) = 100	0%

Figure 33 compares the simulated and experimental P11 statistics for the four inverse simulations described in **Table 7**. **Figure 34** compares the simulated and experimental P22 statistics for the same four simulations described in **Table 7**.

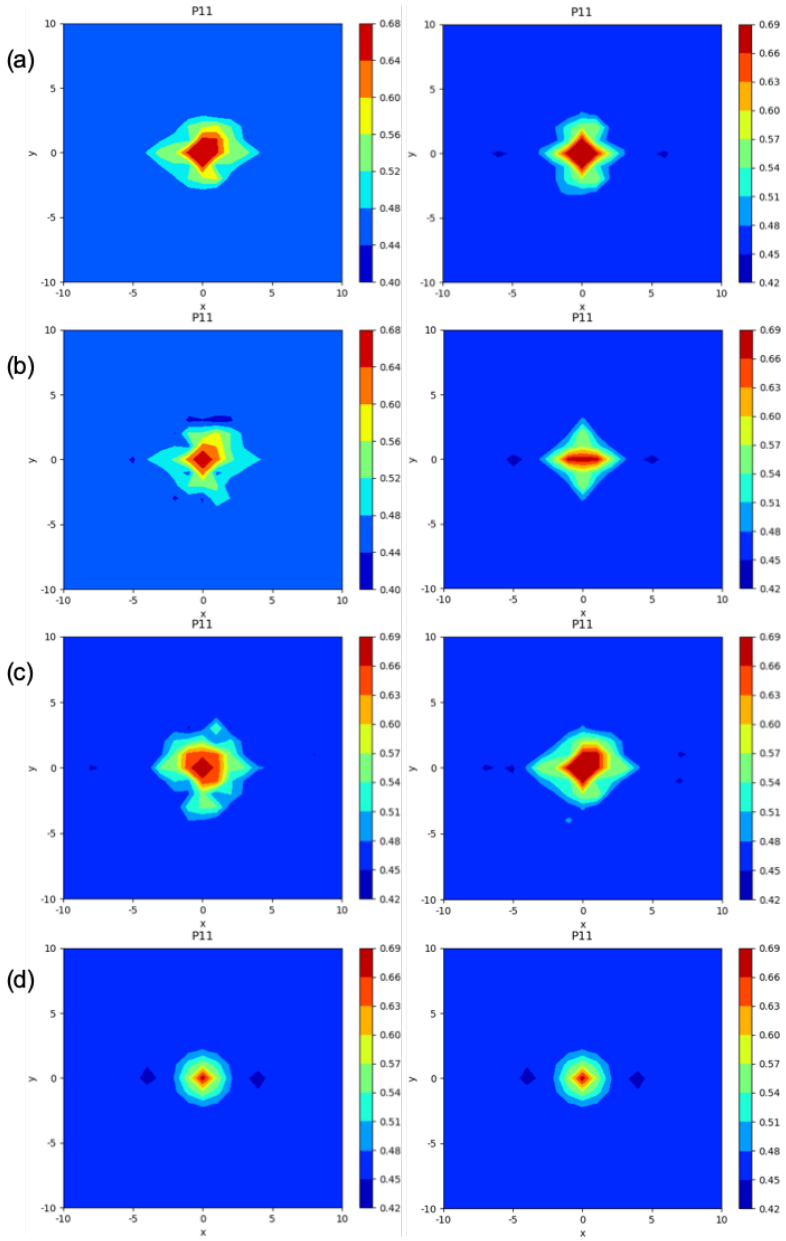

Figure 33: Comparison of the simulated (left) and experimental (right) P11 statistics for the (a) simulation 1 in Table 7, (b) simulation 2 in Table 7, (c) simulation 3 in Table 7, (d) simulation 4 in Table 7.

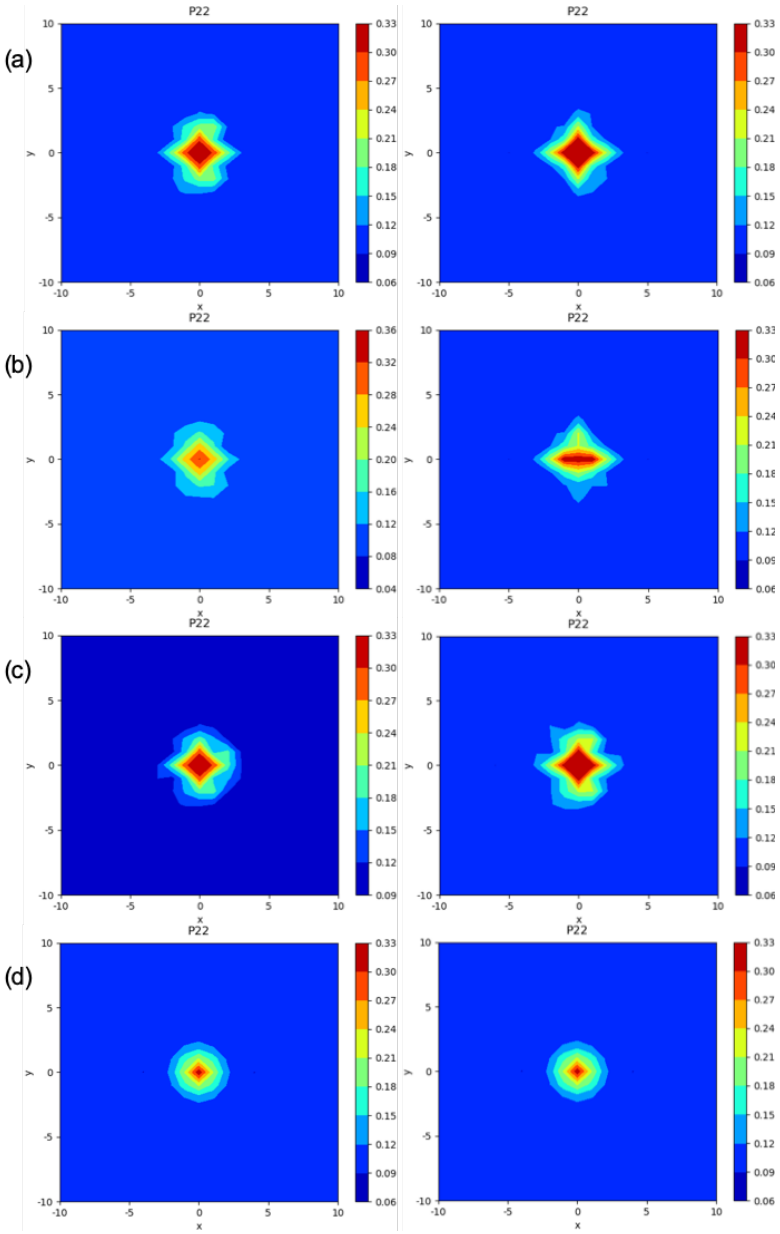

Figure 34: Comparison of the simulated (left) and experimental (right) P22 statistics for the (a) simulation 1 in Table 7, (b) simulation 2 in Table 7, (c) simulation 3 in Table 7, (d) simulation 4 in Table 7.

Both **Figure 33** and **34** show that the inverse model proposed here is capable of accurately predicting the initial microstructure required to obtain a final desired microstructure through the compression deformation process. Furthermore, since the process path function describes the material response to a specific deformation process it is independent

of initial microstructure, and as a result can be saved for future use after calibration. A complete error analysis is provided in section 4.4 to discuss the limitations of the inverse model.

4.4 Discussion

An inverse model has been proposed which predicts the two-point statistics of the initial microstructure required to obtain the two-point statistics of a desired final microstructure. Using this model multiple different simulations were completed and the results were illustrated in section 4.3. To best illustrate the accuracy of the inverse model a full error analysis was performed on each of the inverse simulations performed and is presented here.

4.4.1 Quantifying Inherent Error Using Ti-6Al-4V Calibration Data

As specified in section 4.3, the process path functions were calibrated using the 0%, 20%, 40%, 60%, 80%, and 100% strained two-point statistics. This results in the lowest error being associated with simulations between consecutive strained samples. This is called the inherent error and is the error that is associated with rounding/truncation or the modeling technique itself. The inherent error can be obtained by calculating the error associated with simulations such as simulation 1 in **Table 7**. **Table 8** below specifies each of the simulations which are capable of being used to calculate the inherent error of the inverse model.

Table 8: Model parameters for each simulation used in the calculation of the inherent error.

Simulation ID	Strain of Final Microstructure	$(\eta - \eta_0)$	Strain of Initial Microstructure
Inherent 1	100%	(100 – 80) = 20	80%
Inherent 2	80%	(80 – 60) = 20	60%
Inherent 3	60%	(60 – 40) = 20	40%
Inherent 4	40%	(40 – 20) = 20	20%
Inherent 5	20%	(20 – 0) = 20	0%

For each of the simulations in **Table 8,** the error of the simulation was calculated by averaging the error of each individual point. **Figures 35** and **36** illustrate the error plots associated for the P11 and P22 two-point statistics associated with the Inherent 1 and Inherent 2 simulations from **Table 9**.

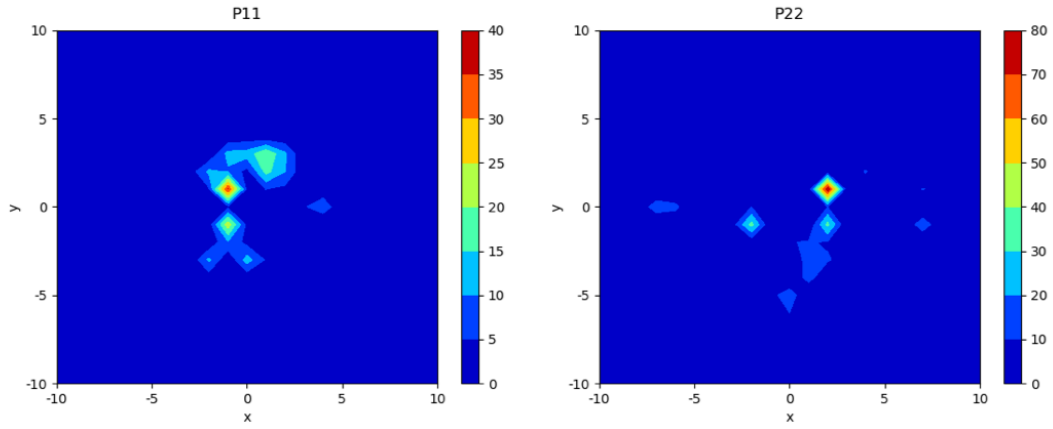

Figure 35: P11 and P22 error plots comparing the simulated and experimental statistics for the Inherent 1 simulation in Table 8.

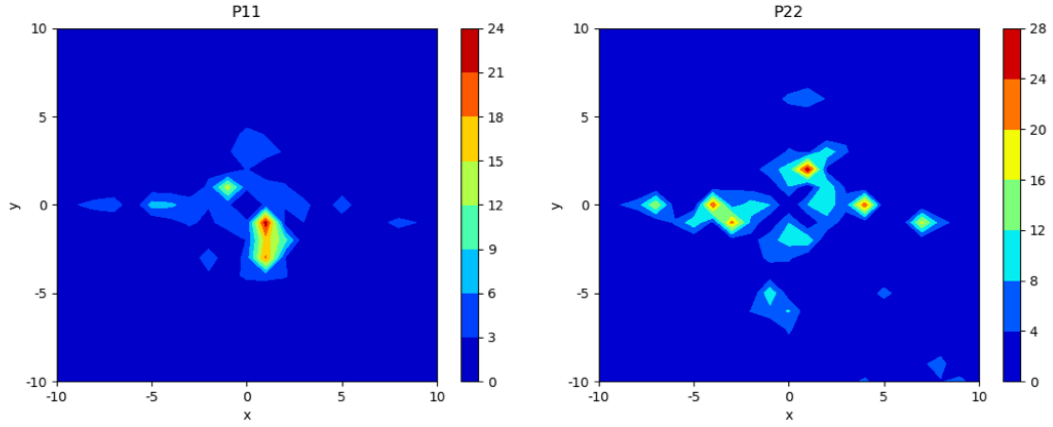

Figure 36: P11 and P22 error plots comparing the simulated and experimental statistics for the Inherent 2 simulation in Table 8.

Figures 35 and **36** show that there are points of high error associated mostly with the central peak of the two-point statistics. This error could mean that the inverse model is unable to accurately predict large changes in the two-point statistics. However, as the simulation points get farther from the central peak the simulation error quickly drops to zero. This shows that while individual points may have a large error, the error associated with the simulation as a whole is rather small. **Table 9** below specifies average error across

all points for each of the simulations in **Table 8**. The average error across these simulations is what will be defined as the inherent error associated with this inverse modeling technique.

Table 9: Average error across all points for the simulation of P11 and P22 associated with Table 8.

Simulation ID	Avg. Error P11 (%)	Avg. Error P22 (%)
Inherent 1	0.19	0.18
Inherent 2	0.15	0.19
Inherent 3	0.12	0.23
Inherent 4	0.15	0.30
Inherent 5	0.13	0.26

Table 9 clearly shows that the inverse model is capable of accurately calculating the two-point statistics of the initial microstructure required to obtain a desired final microstructure. The inherent error is defined using **Table 9** by averaging across all simulations for P11 and P22. This results in an inherent error of 0.143% for the simulation of the P11 statistics and 0.222% for the simulation of the P22 statistics. These low values for the inherent error of the simulation give a strong validation to the predictive capabilities of the proposed inverse model.

4.4.2 Quantification of the Average Error

In section 4.3, **Figure 32** specified all of the possible permutations of the initial and final microstructures that were modeled for this study. The inherent error calculations were obtained using only a small number of these simulations. However, error calculations were performed for all of the permutations in **Figure 33**. **Figure 37** shows the error plots associated with simulations described in **Table 7** in section 4.3. These simulations correspond to predictions which were not used in the calibration of the process path functions. Therefore, the errors associated with these simulations are expected to increase, and it is the amount of increase which will identify if the model is truly able to model the evolution of the two-point statistics.

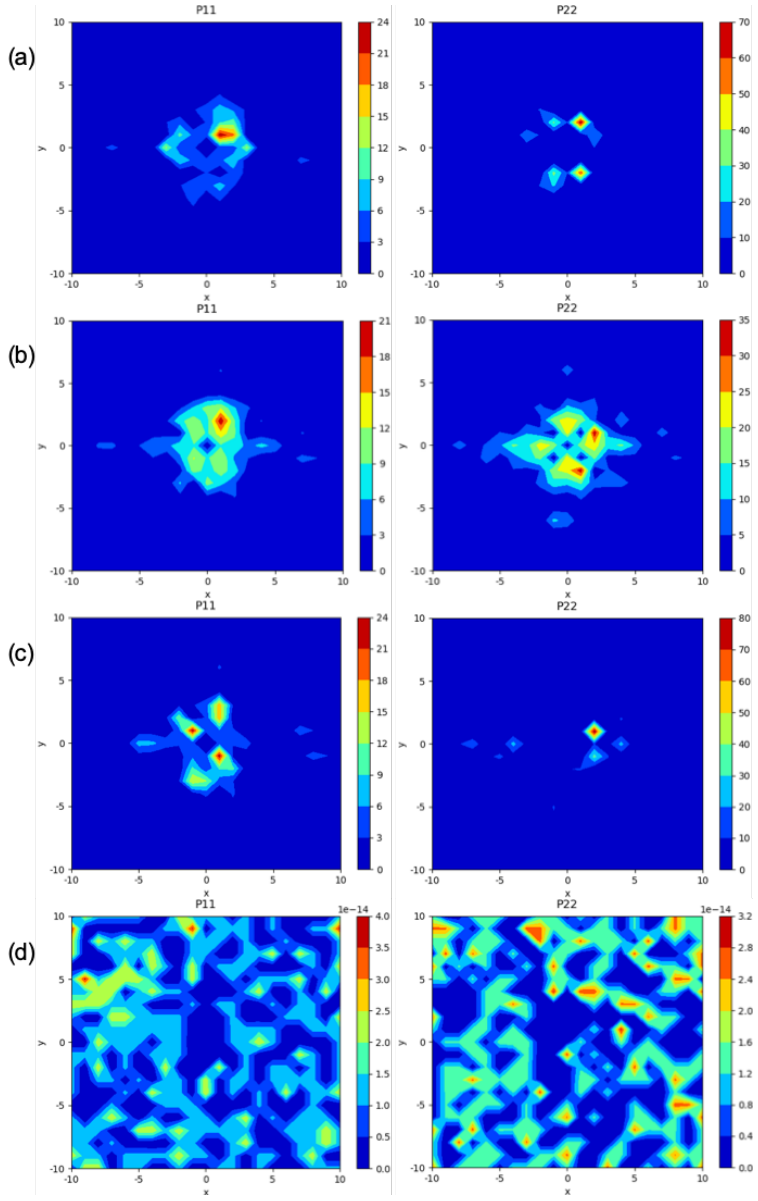

Figure 37: P11 and P22 error plots comparing the simulated and experimental statistics for (a) simulation 1 (b) simulation 2 (c) simulation 3 (d) simulation 4 in Table 7.

Figure 37 shows the error plots obtained after comparing the simulated statistics and experimental statistics for each of the chosen simulations. The error plots for all of the simulations in **Appendix A** can be found in **Appendix B**. From **Figure 37** it can be seen that the largest simulation error is associated with the centralized peak. While these errors

can reach a large maximum for individual points, the overall error is small. **Table 10** describes the average error associated with each simulation found in **Table 7** as well as the total average error across all of the possible permutations found in **Figure 32**.

Table 10: Average error across all points for the simulation of P11 and P22 associated with Table 7 and average error across all simulations.

Simulation ID	Avg. Error P11 (%)	Avg. Error P22 (%)
1	0.12	0.23
2	0.17	0.31
3	0.17	0.19
4	6.5×10^{-15}	5.41×10^{-15}
All	0.145	0.236

From **Table 10** it can be seen that each of the simulations in **Table 7** result in a low error. Furthermore, the average error across all of the inverse simulations is also low though this average is larger than the inherent error obtained from the simulations in **Table 8**. Averaging the error across all simulations results in an error of 0.145% for P11and 0.236% for P22. These small increases in the inherent error show that the model is able to accurately model the material response to the compression process and therefore does not need to be trained using dozens of microstructures. The error plots and table reported in this section, as well as the plots found in **Appendix B**, illustrate that the process path

function has been calibrated to model the material response to the deformation process. Furthermore, it is expected that these errors can be lowered further through continued calibration of the process path function.

4.5 Conclusion

Inverse models for the prediction of the initial microstructure required to obtain a desired final microstructure are of great interest to the materials science community and industrial partners. These models are highly sought after due to their ability to be integrated into material process optimization and for their cost saving potential for industry. A data-driven inverse model is proposed here which utilizes two-point statistics to define the material microstructure and predict the material response to a given deformation process. This model has been shown to be capable of accurately predicting the two-point statistics of the initial microstructure required to obtain a desired final microstructure. The application of this model to isothermal compression in a Ti-6Al-4V alloy, including synthetically created microstructures, has illustrated the strengths of the model. However, this model is not limited to the Ti-6Al-4V material system. Validation of the inverse model for other systems and processing procedures is left for future research opportunities.

CHAPTER 5. CONCLUSIONS

5.1 Summary of Key Conclusions

The development of microstructure evolution models which require few computational resources, while maintaining model accuracy, is of great interest for applications which require fast response times, such as additive manufacturing and nuclear forensics. Both forward and inverse models have been developed here which allow for the prediction of microstructure evolution.

5.1.1 Key Conclusions in the Inverse Modeling of Texture for Nuclear Forensics

An inverse model was developed following the work of Li et al.[31] which is capable of predicting the initial ODF required to obtain a desired final ODF. The work of Li was expanded upon to be applied to hot rolling in a dual-phase Zr-18wt.%Nb system, which included an annealing stage unable to be simulated by Li's work. The inverse model simulations show that after recrystallization was considered, the model was capable of accurately predicting the initial microstructure required to obtain a desired final microstructure. For the nuclear forensics application chosen, the ability to simulate such a processing procedure allows for quick and accurate identification of how interdicted material was processed and, therefore, the location of origin.

5.1.2 Key Conclusions in the Forward Modeling of Deformation in Two-Phase Materials

A forward model was created building upon the work of Garmestani et al.[51] to model the deformation of two-point statistics due to an imposed strain rate. The created

model is capable of evolving the two-point statistics by first calculating the localized velocity gradients, and eventually the deformation caused by the velocity gradients. The evolution results show that the model underestimates the deformation which results in the compression of two points (i.e. when deformation is negative) but is able to accurately calculate the deformation caused by the tensile velocity gradients. Furthermore, this model is capable of simulating the full two-point statistics map and, as such, is able to model anisotropic material systems which the original model was unable to do.

5.1.3 Key Conclusions in the Inverse Modeling of Deformation in Two-Phase Materials

An inverse model was created following the work performed in chapter 2 which is capable of predicting the initial two-point statistics required to obtain a desired final set of statistics. The forward model created in chapter 3 was used to provide calibration data for the calculation of the process path function. The calculated process path function was then used in the inverse model simulations to predict the initial statistics required to obtain a desired final set of statistics. The inverse model simulation results show that the methodology proposed is capable of providing accurate simulations, however the model type chosen here may be the one with the lowest error.

5.2 Future Work

Following the models presented here, future developments for microstructure evolution models include the expansion of the microstructural features of interest, as well as the validation of each of the current models for different material systems and processing conditions. One avenue for the expansion of the microstructural features of interest is the development of a model capable of simulating the evolution of the two-point correlation

functions of the crystallographic orientation. This is possible through the use of EBSD images which contain information on both location and crystallographic orientation of each grain in the microstructure. Furthermore, one avenue for the validation of each model for different material systems is utilizing turning data in the dual-phase Ti-6Al-4V alloy. Turning provides a more complex strain rate tensor which varies with depth into the specimen surface. This complex strain rate tensor provides an opportunity to predict the deformation of complex processing procedures which are very difficult to predict through any material modeling system.

APPENDIX A. INVERSE SIMULATIONS OF TWO-PHASE TWO-POINT STATISTICS

The figures illustrated in this appendix compare the experimental (top) and simulated (bottom) two-point statistics for each inverse simulation specified in **Figure 32**. Prior to each figure is a table which specifies the model parameters for the associated simulation.

Strain of Final Microstructure	$(\eta - \eta_0)$	Strain of Initial Microstructure
100%	(100 – 90) = 10	90%

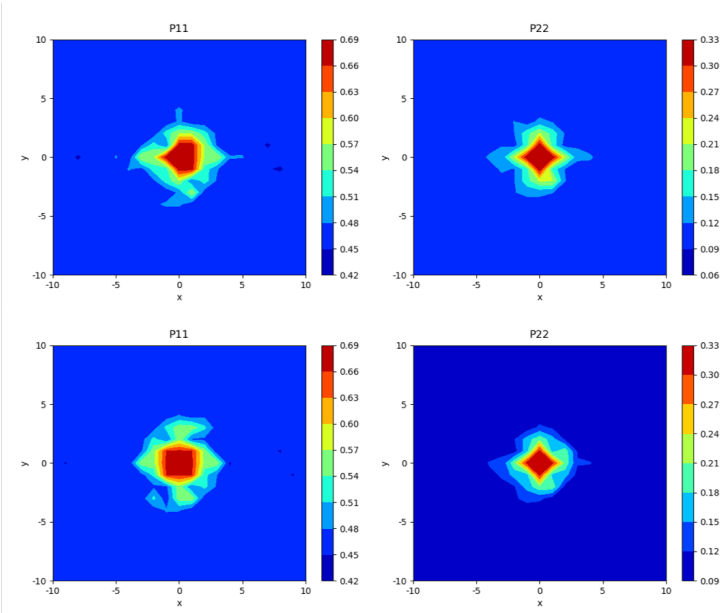

Strain of Final Microstructure	$(\eta - \eta_0)$	Strain of Initial Microstructure
100%	(100 – 80) = 20	80%

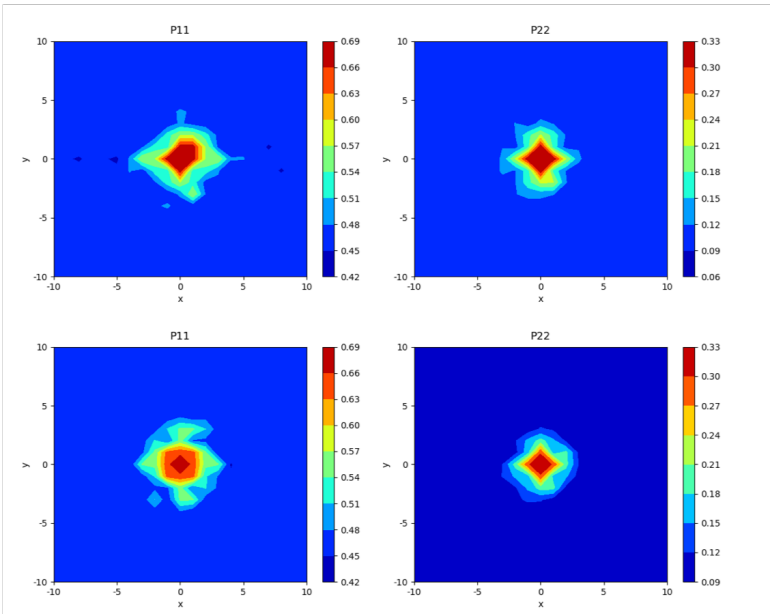

Strain of Final Microstructure	$(\eta - \eta_0)$	Strain of Initial Microstructure
100%	(100 – 70) = 30	70%

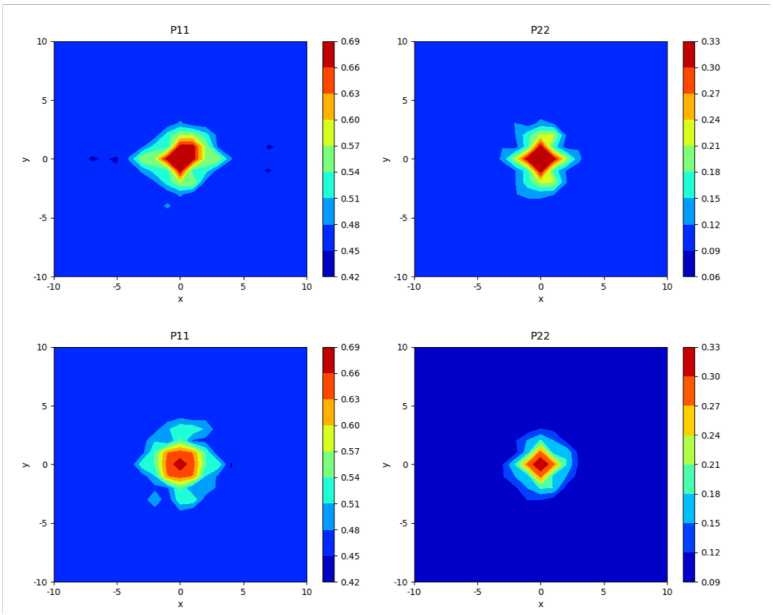

Strain of Final Microstructure	$(\eta - \eta_0)$	Strain of Initial Microstructure
100%	(100 – 60) = 40	60%

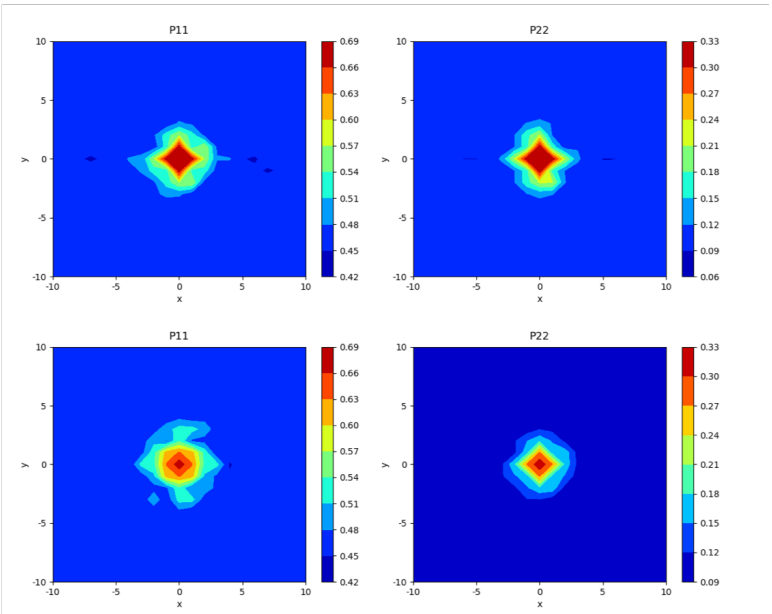

Strain of Final Microstructure	$(\eta - \eta_0)$	Strain of Initial Microstructure
100%	(100 – 50) = 50	50%

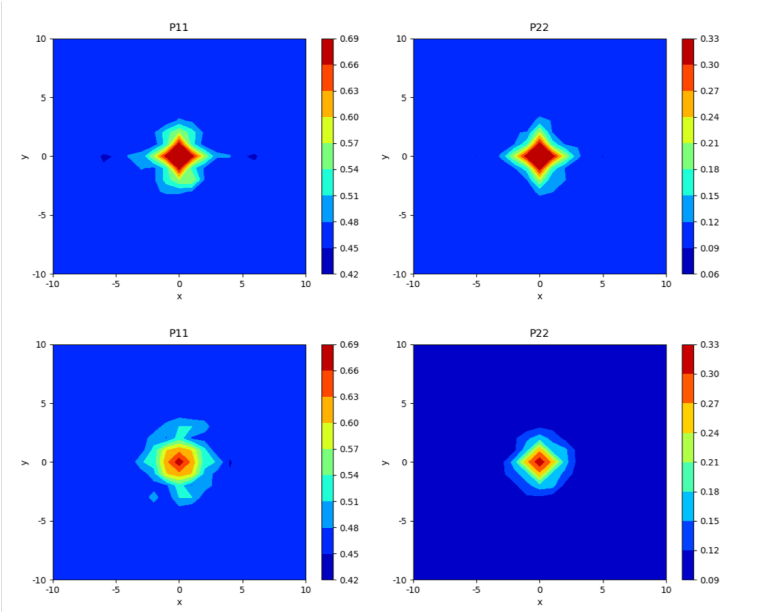

Strain of Final Microstructure	$(\eta - \eta_0)$	Strain of Initial Microstructure
100%	(100 – 40) = 60	40%

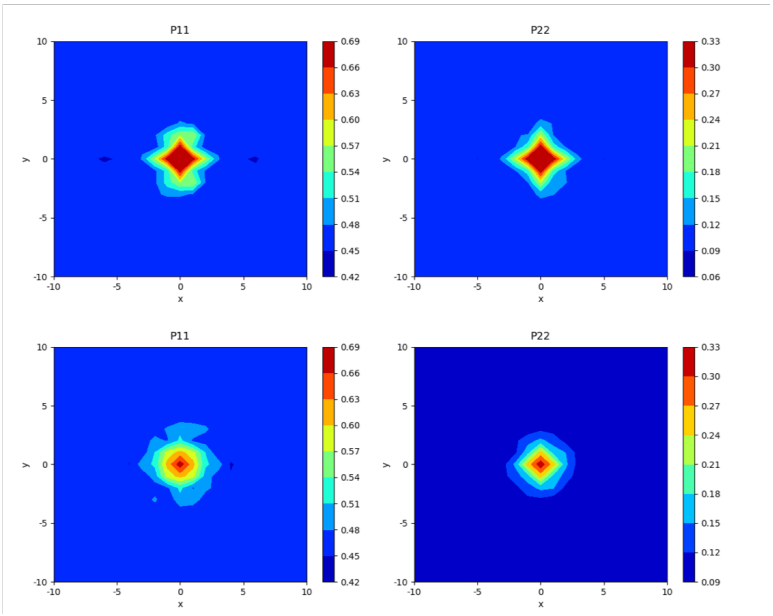

Strain of Final Microstructure	$(\eta - \eta_0)$	Strain of Initial Microstructure
100%	(100 – 30) = 70	30%

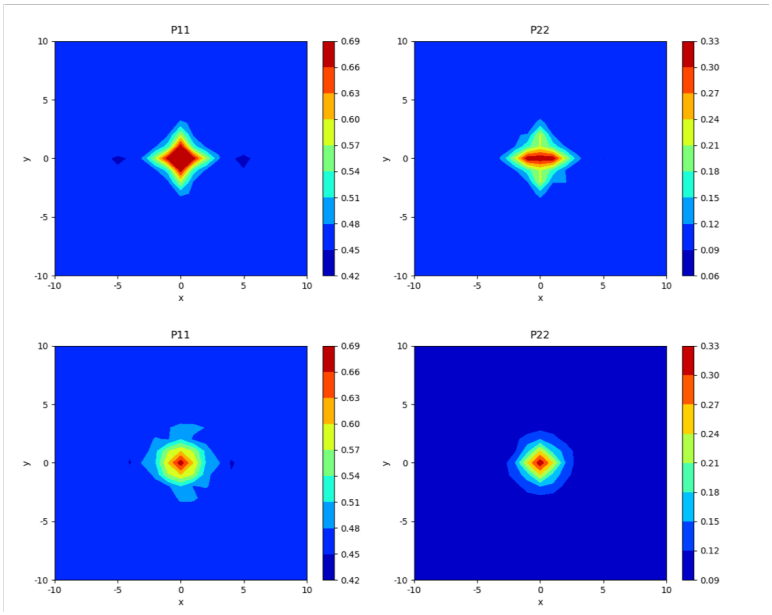

Strain of Final Microstructure	$(\eta - \eta_0)$	Strain of Initial Microstructure
100%	(100 – 20) = 80	20%

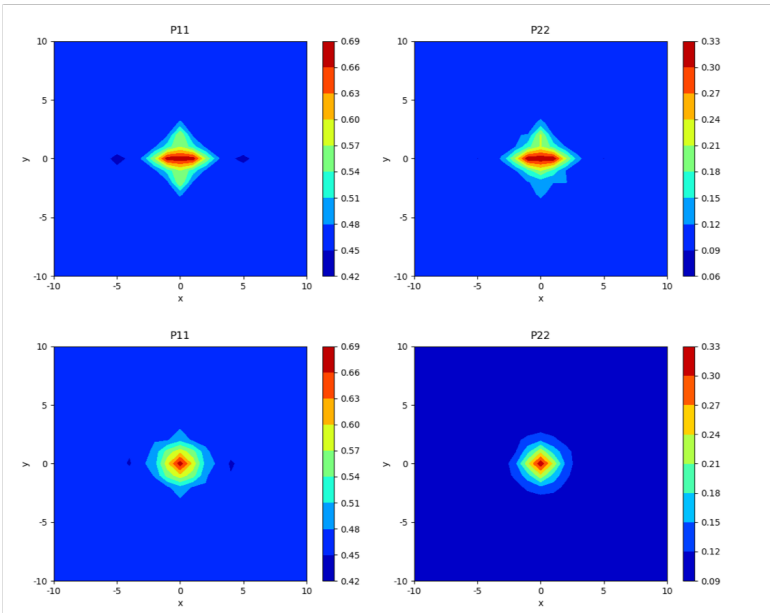

Strain of Final Microstructure	$(\eta - \eta_0)$	Strain of Initial Microstructure
100%	(100 – 10) = 90	10%

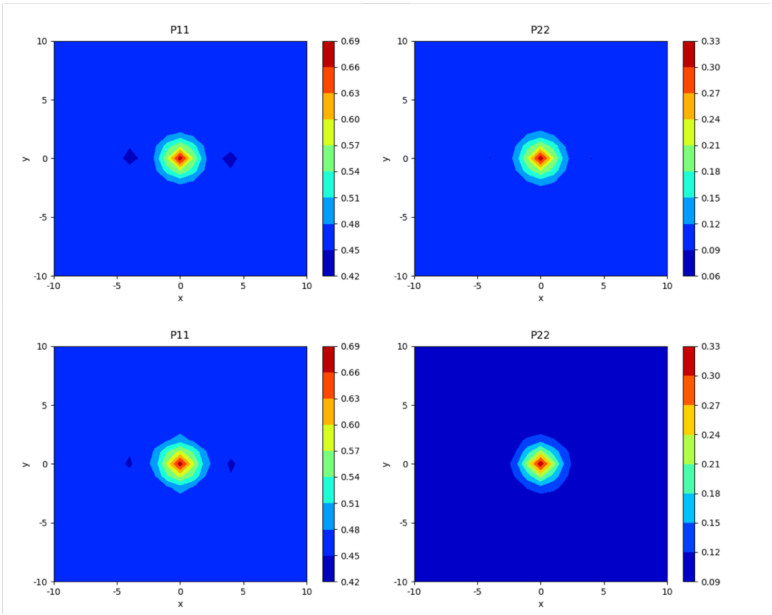

Strain of Final Microstructure	$(\eta - \eta_0)$	Strain of Initial Microstructure
100%	(100 – 0) = 100	0%

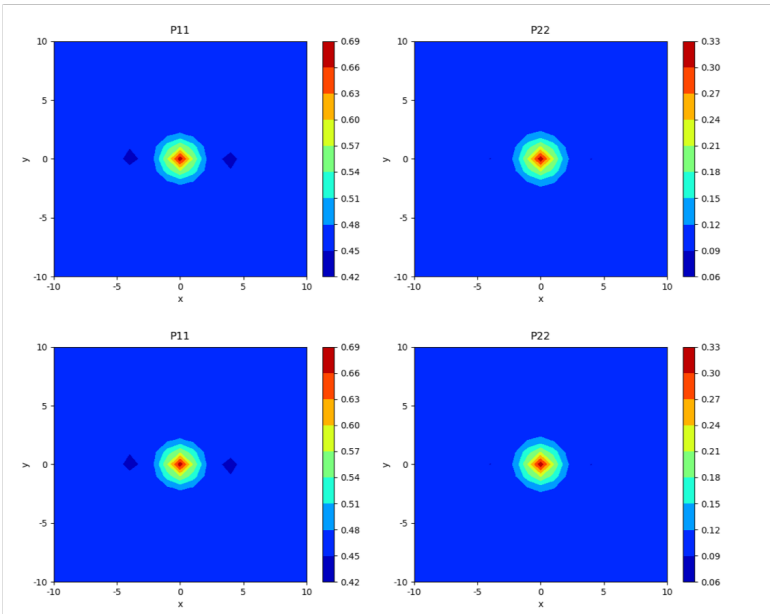

Strain of Final Microstructure	$(\eta - \eta_0)$	Strain of Initial Microstructure
90%	(90 – 80) = 10	80%

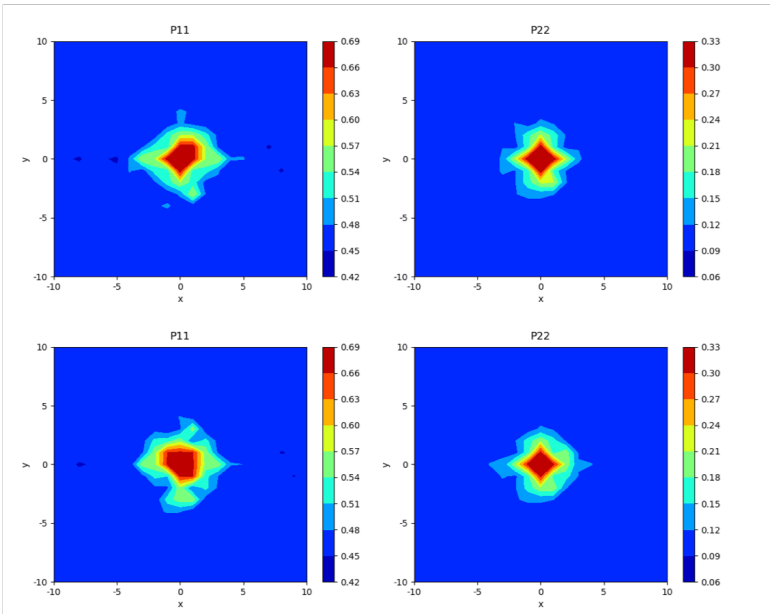

Strain of Final Microstructure	$(\eta - \eta_0)$	Strain of Initial Microstructure
90%	(90 – 70) = 20	70%

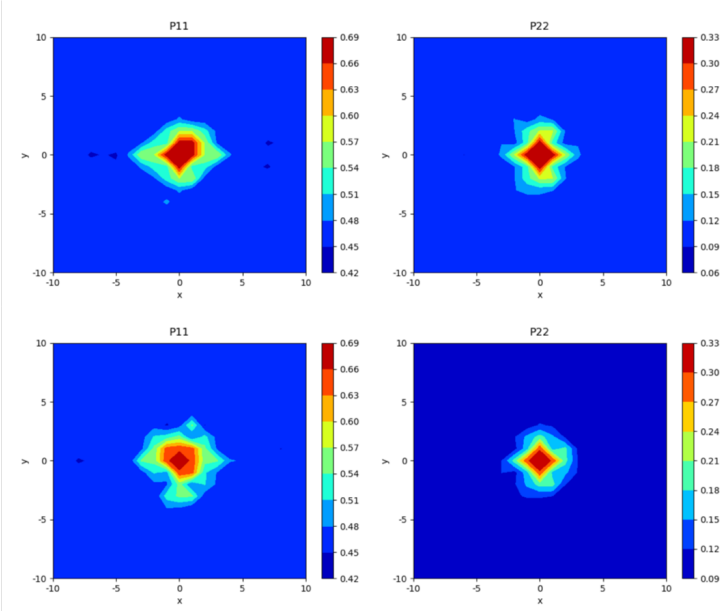

Strain of Final Microstructure	$(\eta - \eta_0)$	Strain of Initial Microstructure
90%	(90 – 60) = 30	60%

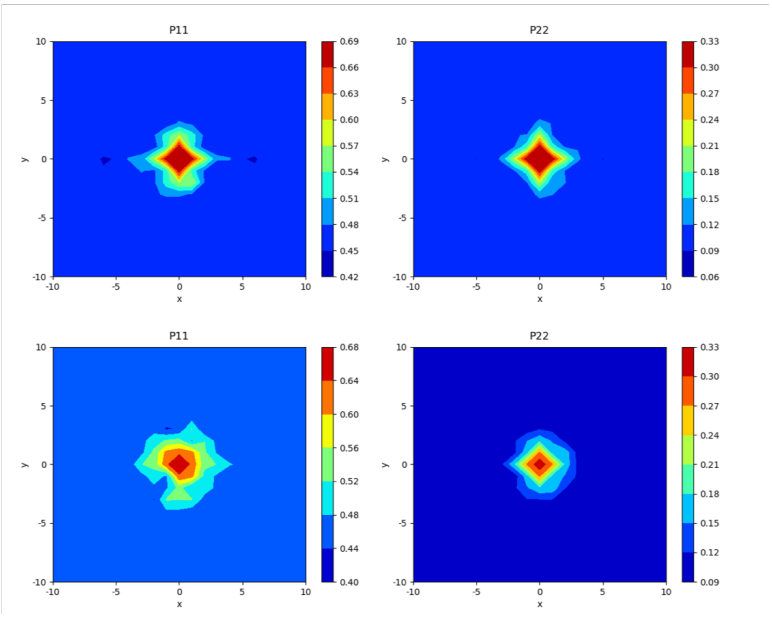

Strain of Final Microstructure	$(\eta - \eta_0)$	Strain of Initial Microstructure
90%	(90 – 50) = 40	50%

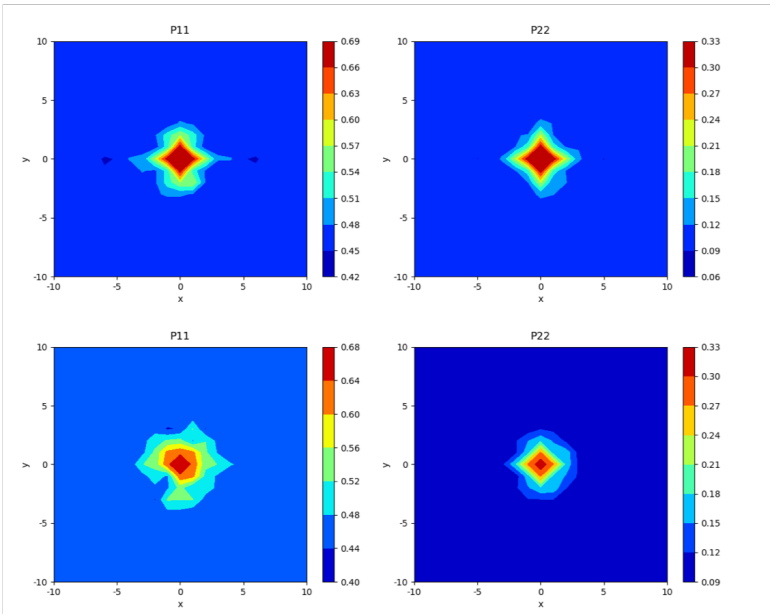

Strain of Final Microstructure	$(\eta - \eta_0)$	Strain of Initial Microstructure
90%	(90 – 40) = 50	40%

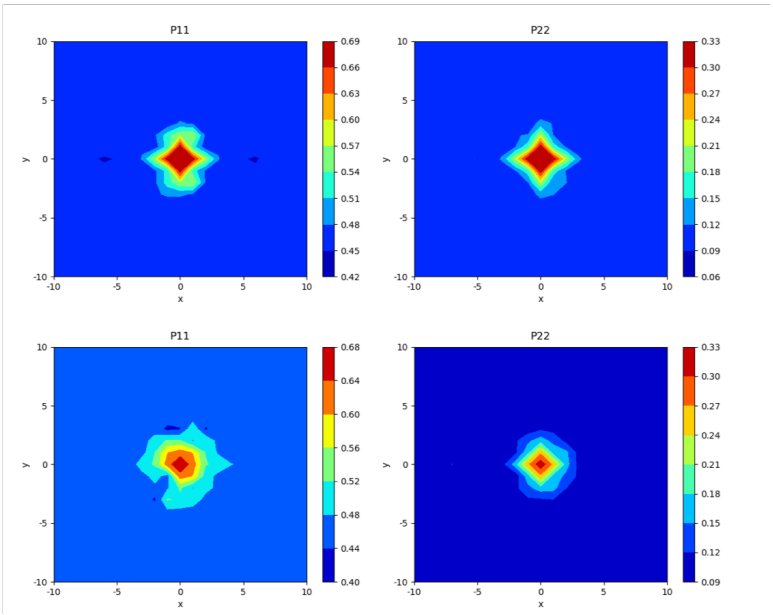

Strain of Final Microstructure	$(\eta - \eta_0)$	Strain of Initial Microstructure
90%	(90 – 30) = 60	30%

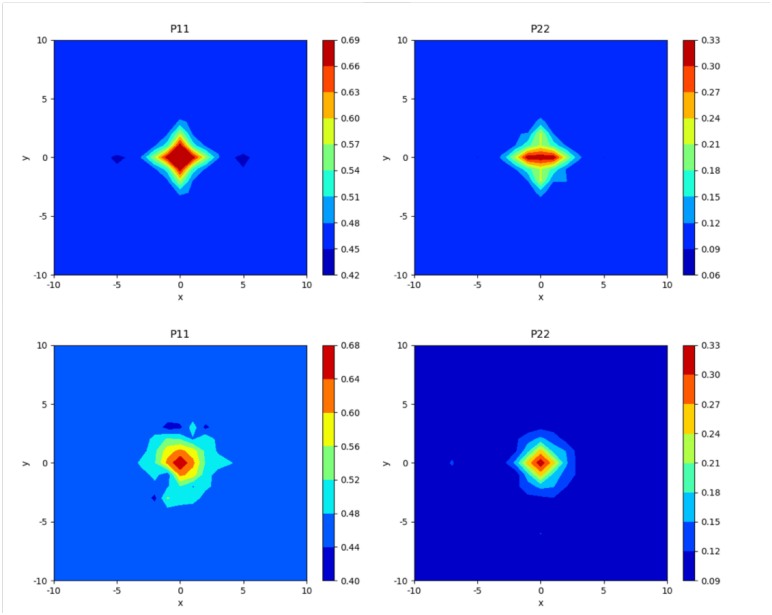

Strain of Final Microstructure	$(\eta - \eta_0)$	Strain of Initial Microstructure
90%	(90 – 20) = 70	20%

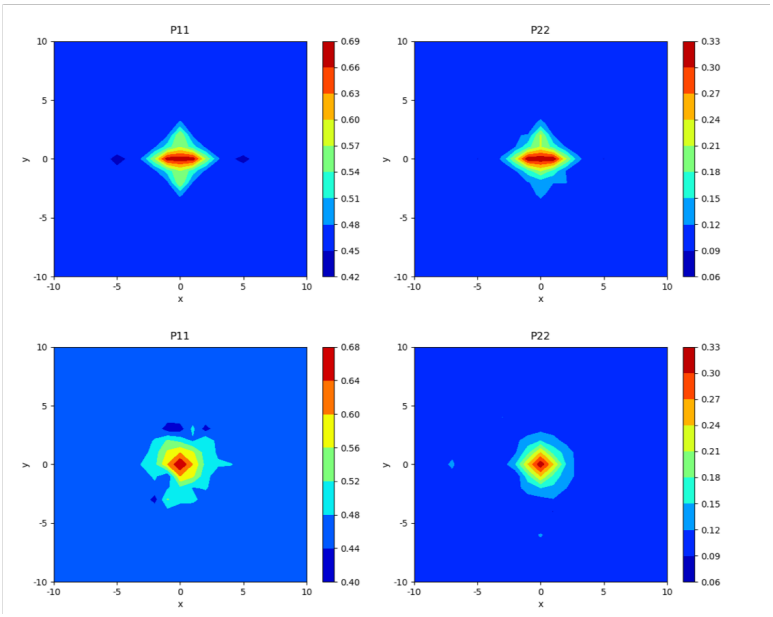

Strain of Final Microstructure	$(\eta - \eta_0)$	Strain of Initial Microstructure
90%	(90 – 10) = 80	10%

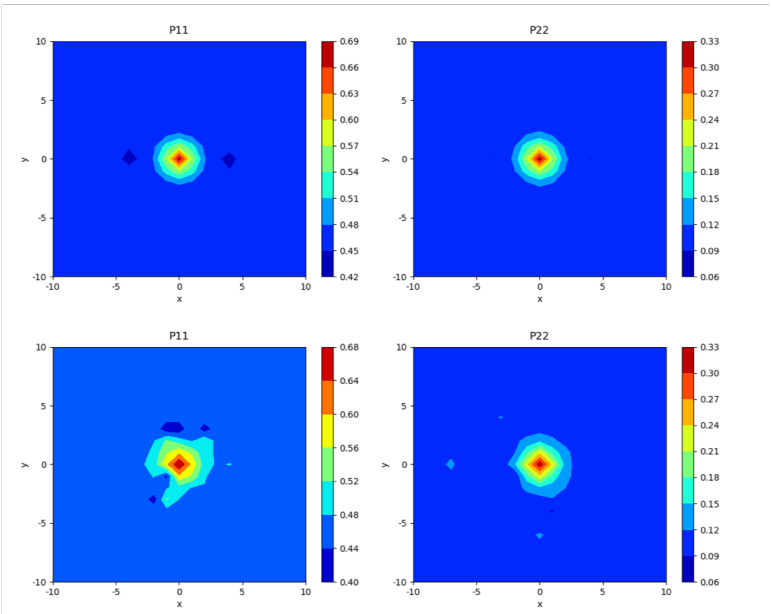

Strain of Final Microstructure	$(\eta - \eta_0)$	Strain of Initial Microstructure
90%	(90 – 0) = 90	0%

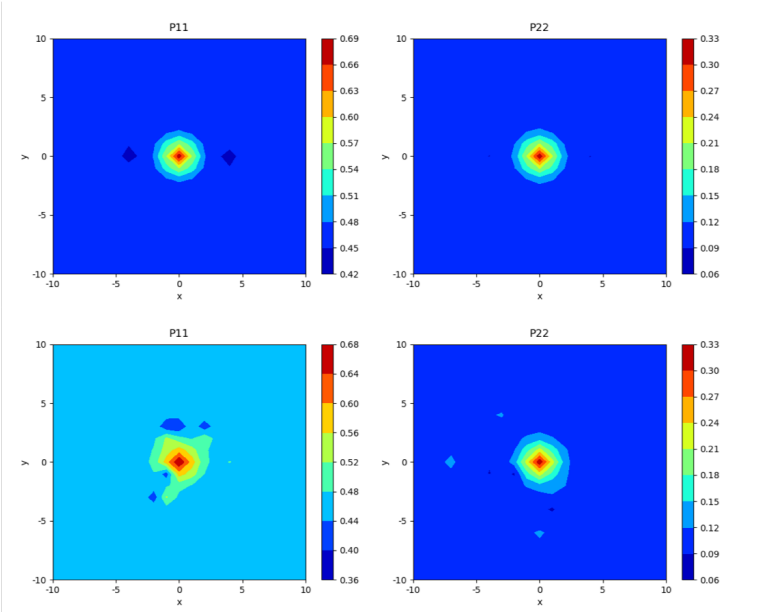

Strain of Final Microstructure	$(\eta - \eta_0)$	Strain of Initial Microstructure
80%	(80 – 70) = 10	70%

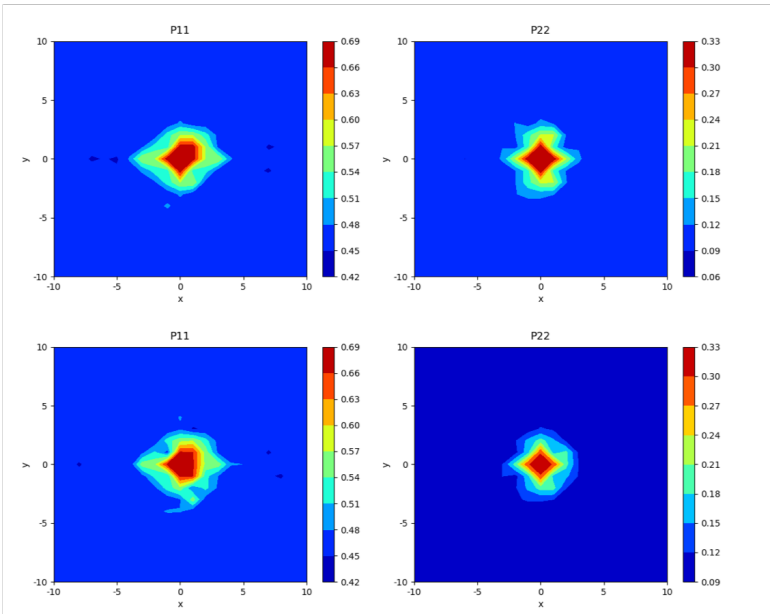

Strain of Final Microstructure	$(\eta - \eta_0)$	Strain of Initial Microstructure
80%	(80 – 60) = 20	60%

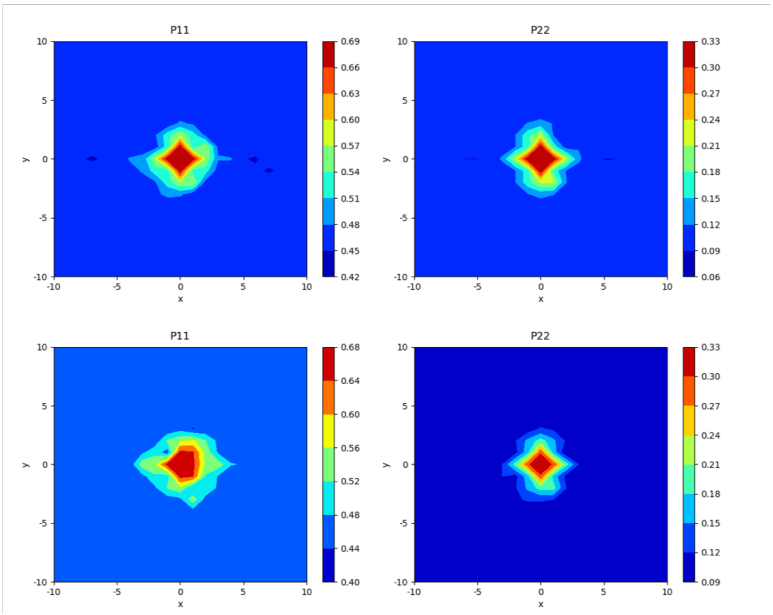

Strain of Final Microstructure	$(\eta - \eta_0)$	Strain of Initial Microstructure
80%	(80 – 50) = 30	50%

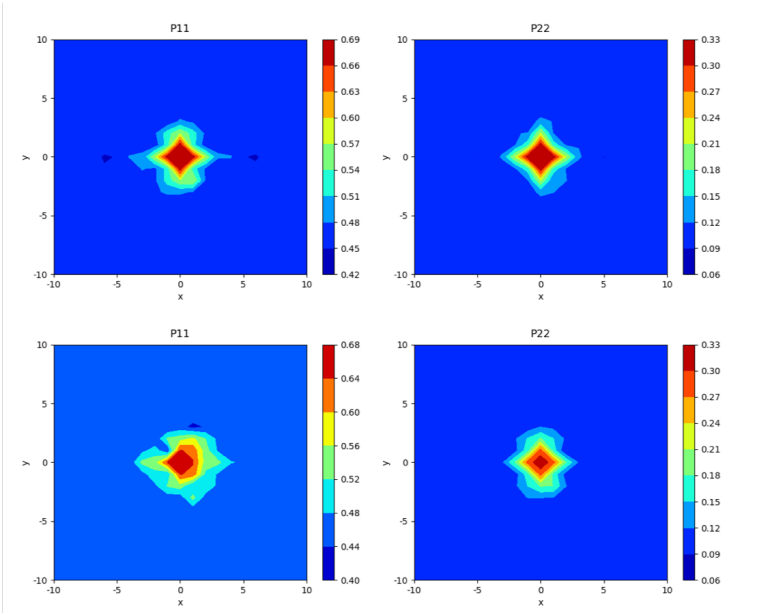

Strain of Final Microstructure	$(\eta - \eta_0)$	Strain of Initial Microstructure
80%	(80 – 40) = 40	40%

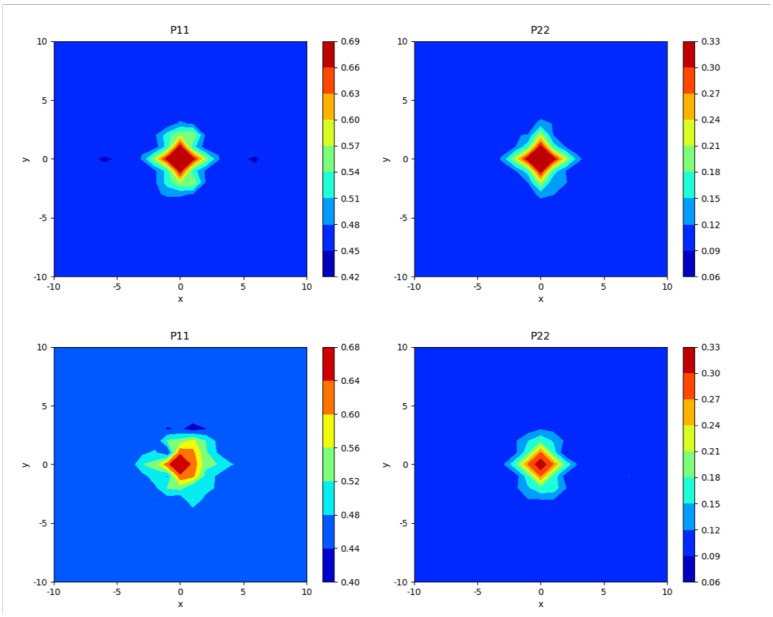

Strain of Final Microstructure	$(\eta - \eta_0)$	Strain of Initial Microstructure
80%	(80 – 30) = 50	30%

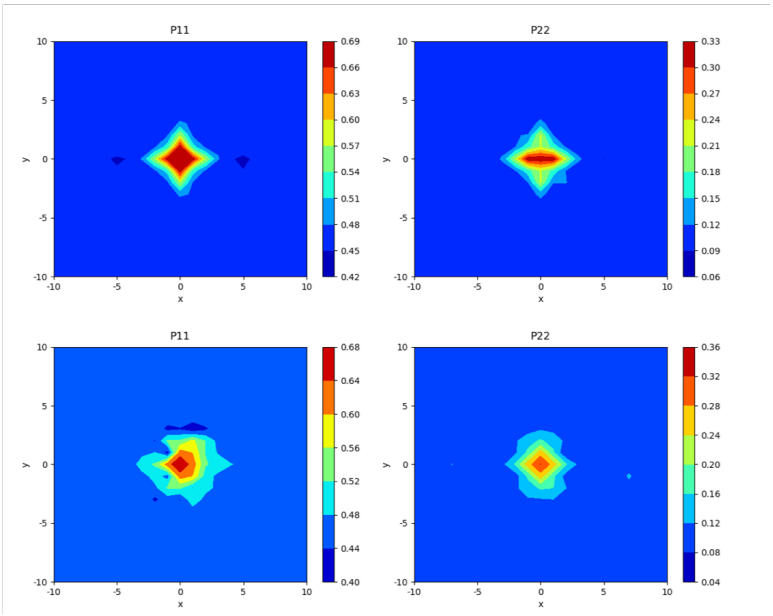

Strain of Final Microstructure	$(\eta - \eta_0)$	Strain of Initial Microstructure
80%	(80 – 20) = 60	20%

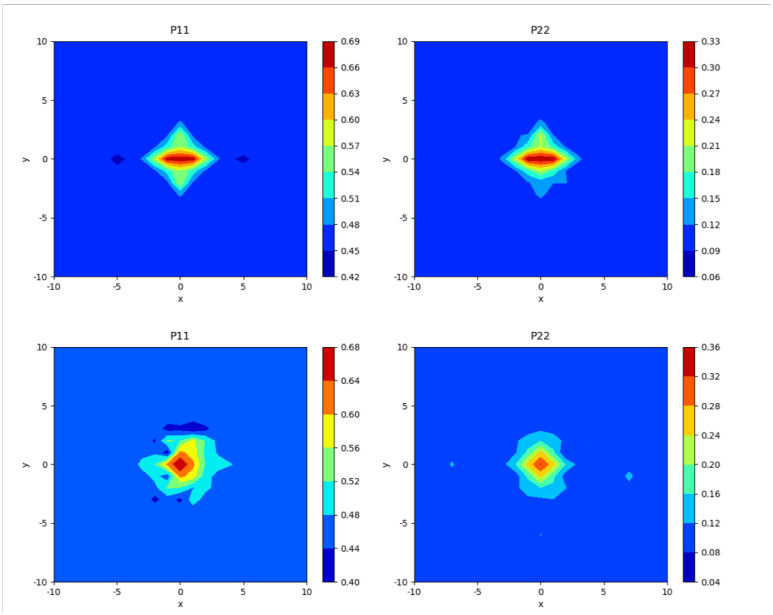

Strain of Final Microstructure	$(\eta - \eta_0)$	Strain of Initial Microstructure
80%	(80 – 10) = 70	10%

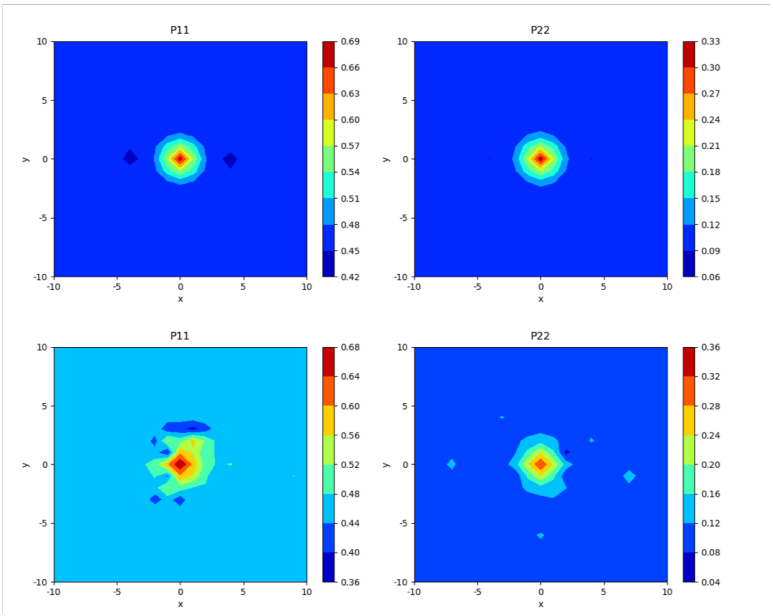

Strain of Final Microstructure	$(\eta - \eta_0)$	Strain of Initial Microstructure
80%	(80 – 0) = 80	0%

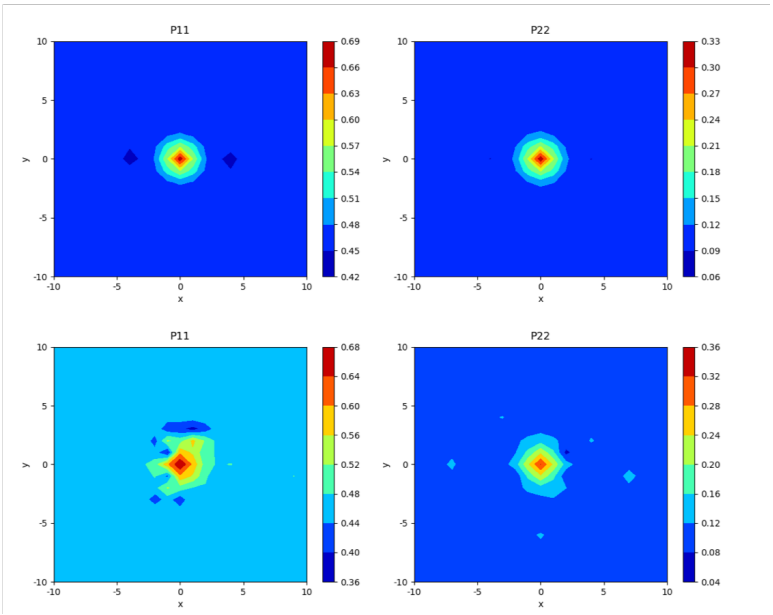

Strain of Final Microstructure	$(\eta - \eta_0)$	Strain of Initial Microstructure
70%	(70 – 60) = 10	60%

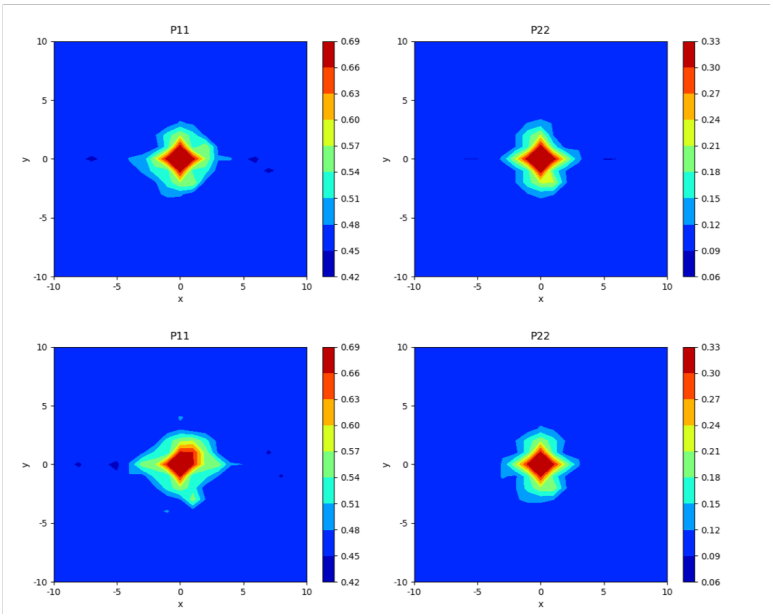

Strain of Final Microstructure	$(\eta - \eta_0)$	Strain of Initial Microstructure
70%	(70 – 50) = 20	50%

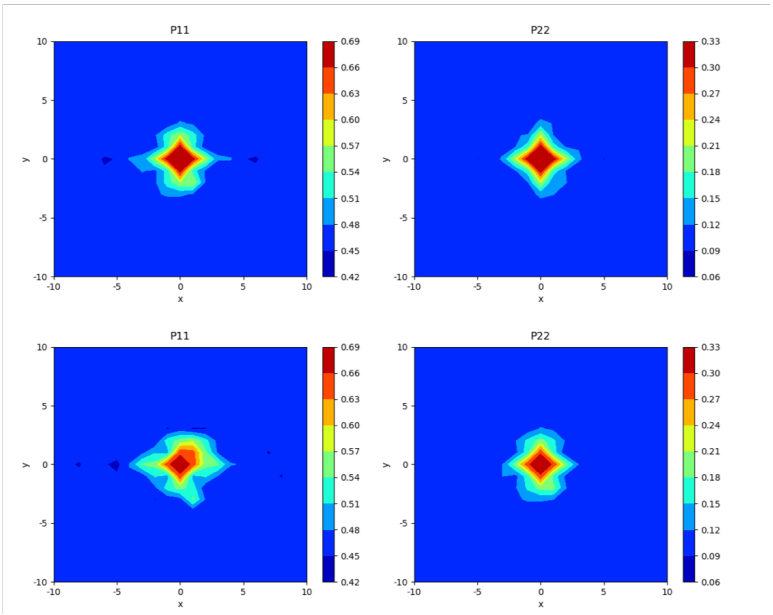

Strain of Final Microstructure	$(\eta - \eta_0)$	Strain of Initial Microstructure
70%	(70 – 40) = 30	40%

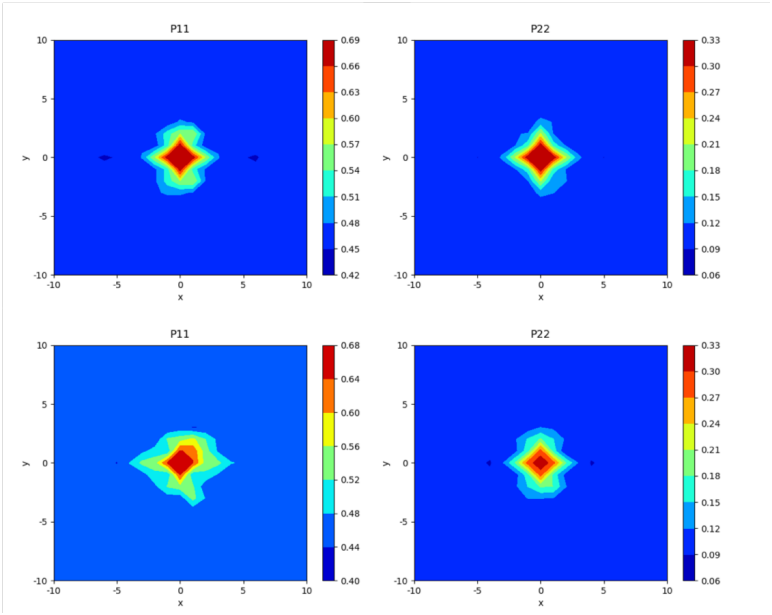

Strain of Final Microstructure	$(\eta - \eta_0)$	Strain of Initial Microstructure
70%	(70 – 30) = 40	30%

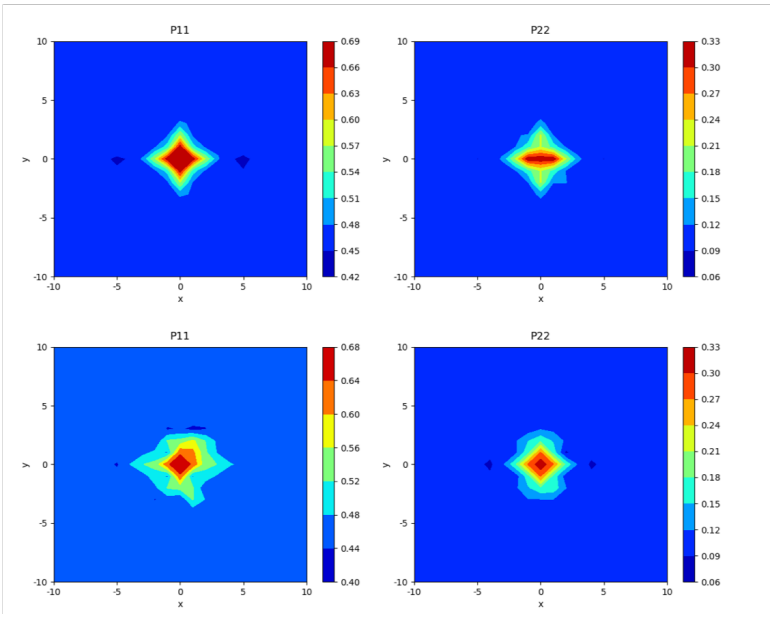

Strain of Final Microstructure	$(\eta - \eta_0)$	Strain of Initial Microstructure
70%	(70 – 20) = 50	20%

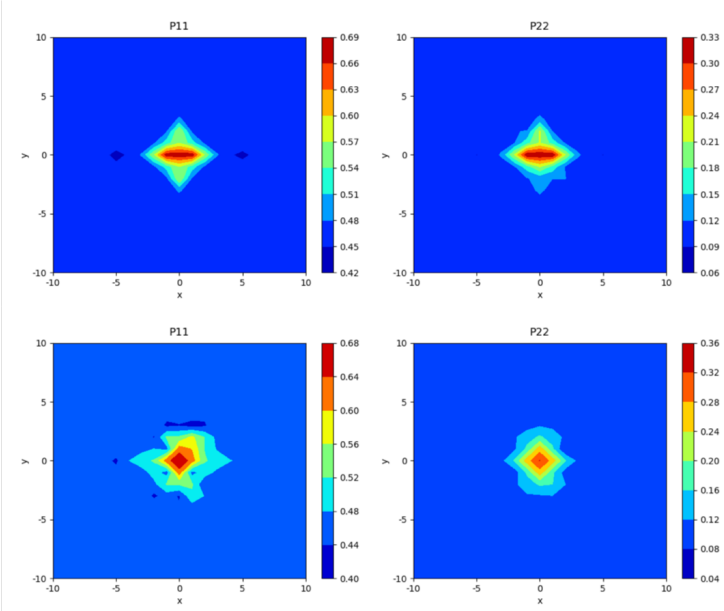

Strain of Final Microstructure	$(\eta - \eta_0)$	Strain of Initial Microstructure
70%	(70 – 10) = 60	10%

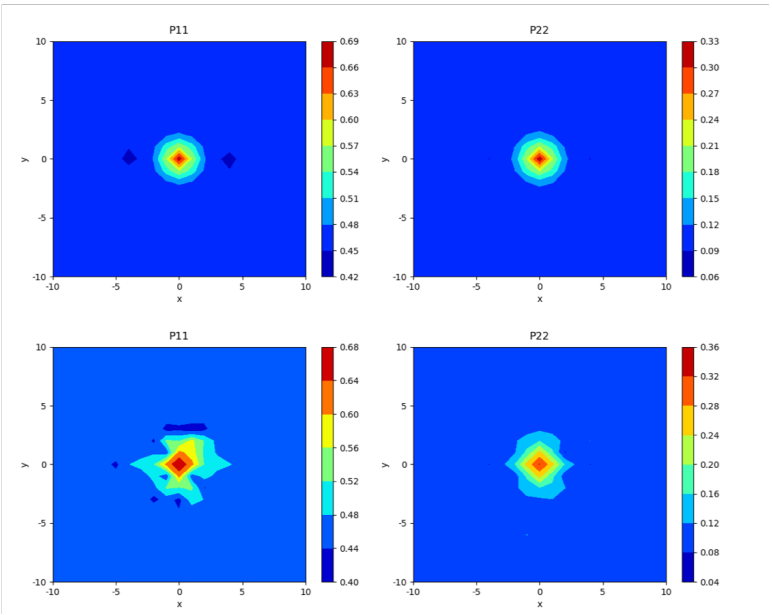

Strain of Final Microstructure	$(\eta - \eta_0)$	Strain of Initial Microstructure
70%	(70 – 0) = 70	0%

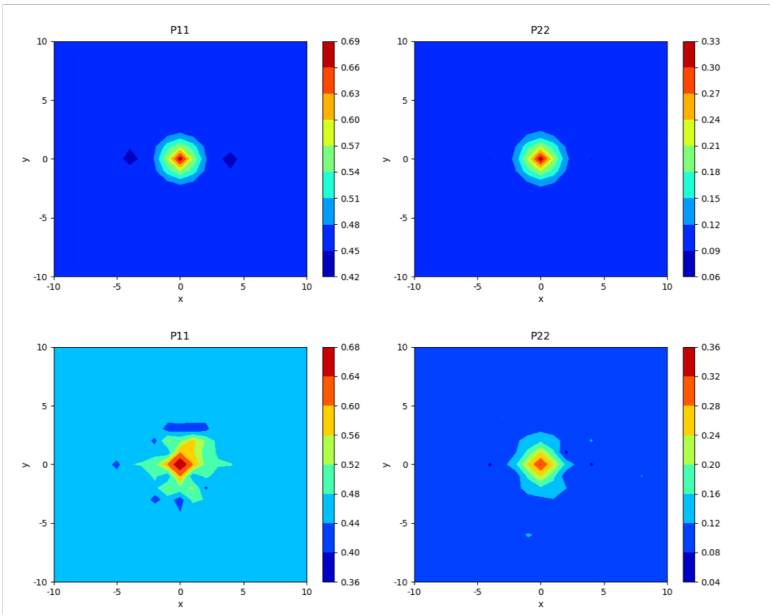

Strain of Final Microstructure	$(\eta - \eta_0)$	Strain of Initial Microstructure
60%	(60 – 50) = 10	50%

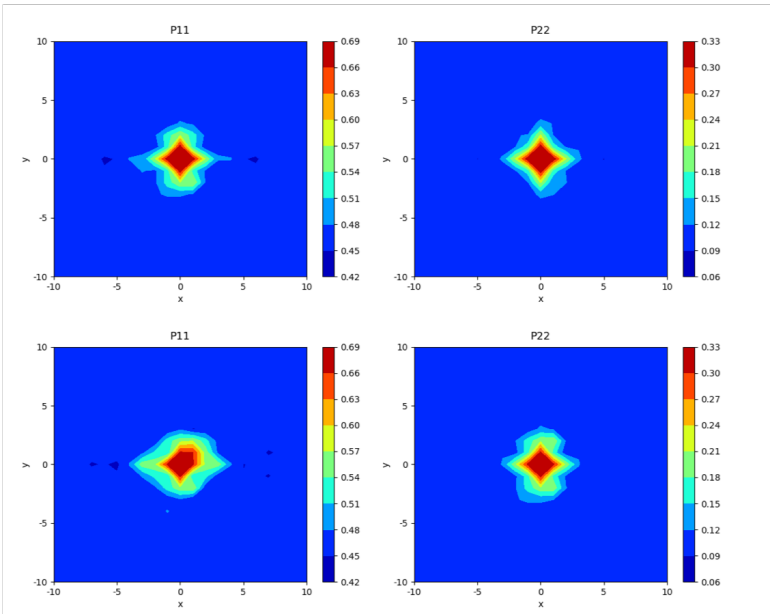

Strain of Final Microstructure	$(\eta - \eta_0)$	Strain of Initial Microstructure
60%	(60 – 40) = 20	40%

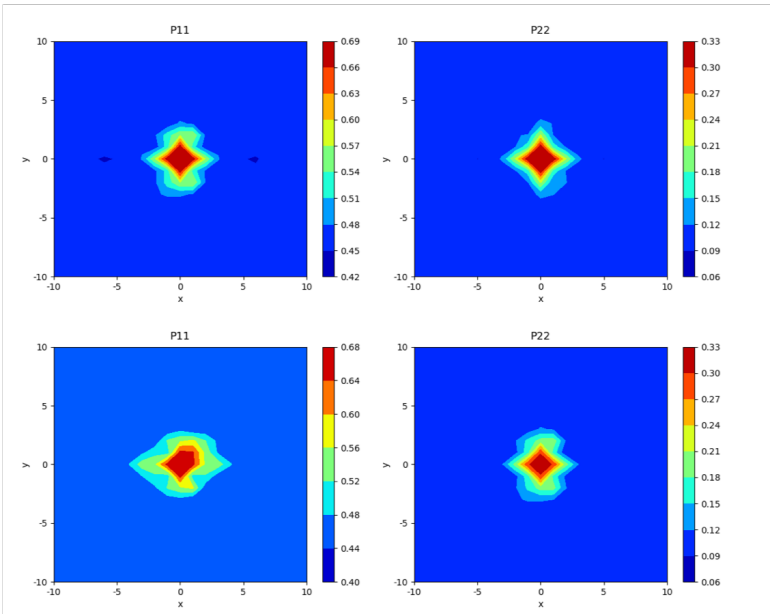

Strain of Final Microstructure	$(\eta - \eta_0)$	Strain of Initial Microstructure
60%	(60 – 30) = 30	30%

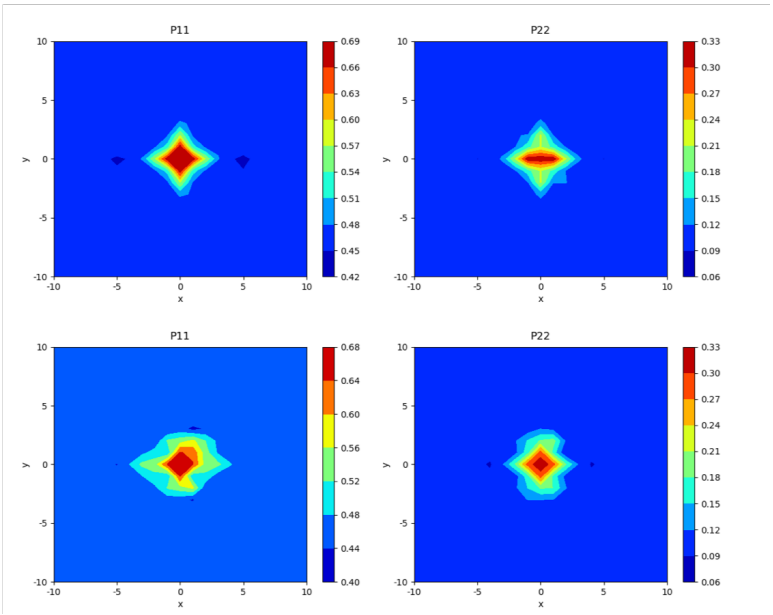

Strain of Final Microstructure	$(\eta - \eta_0)$	Strain of Initial Microstructure
60%	(60 – 20) = 40	20%

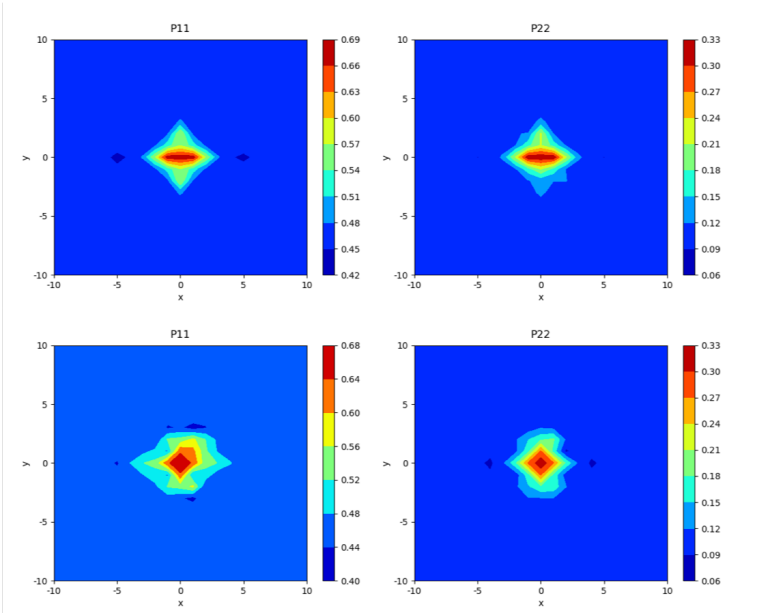

Strain of Final Microstructure	$(\eta - \eta_0)$	Strain of Initial Microstructure
60%	(60 – 10) = 50	10%

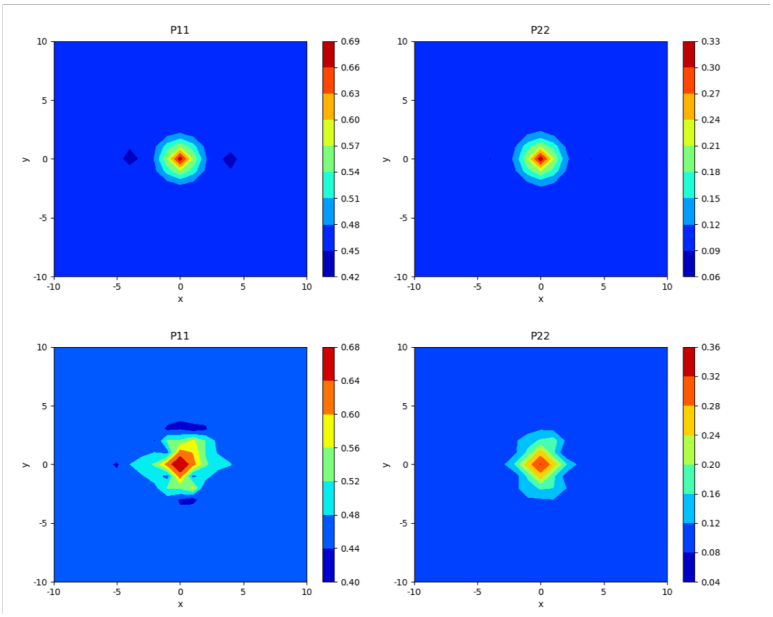

Strain of Final Microstructure	$(\eta - \eta_0)$	Strain of Initial Microstructure
60%	(60 – 0) = 60	0%

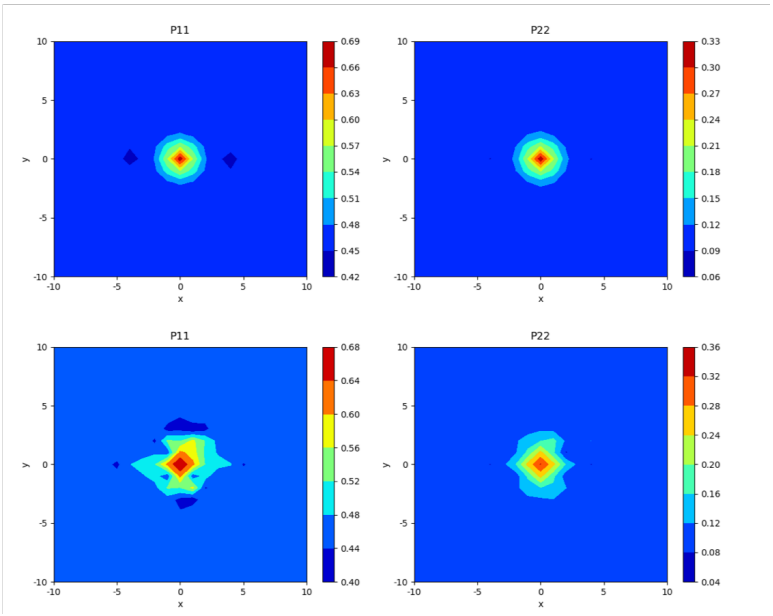

Strain of Final Microstructure	$(\eta - \eta_0)$	Strain of Initial Microstructure
50%	(50 – 40) = 10	40%

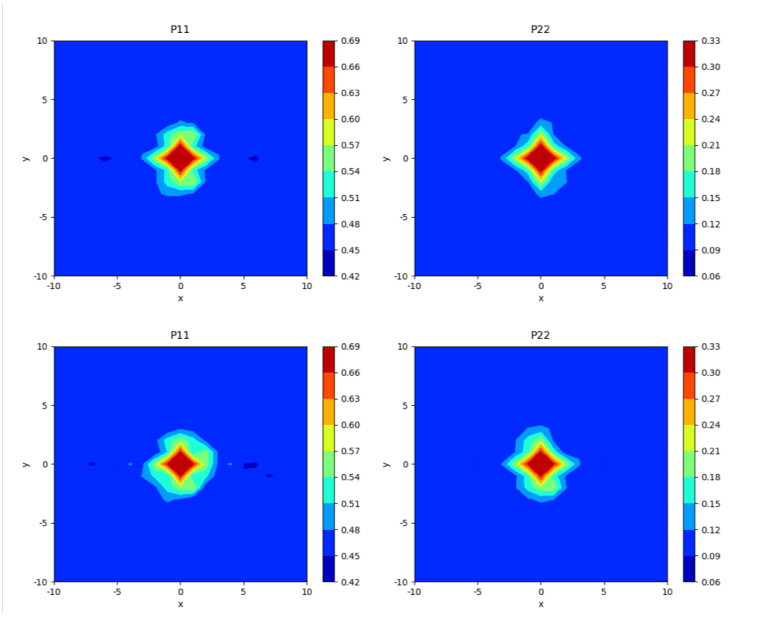

Strain of Final Microstructure	$(\eta - \eta_0)$	Strain of Initial Microstructure
50%	(50 – 30) = 20	30%

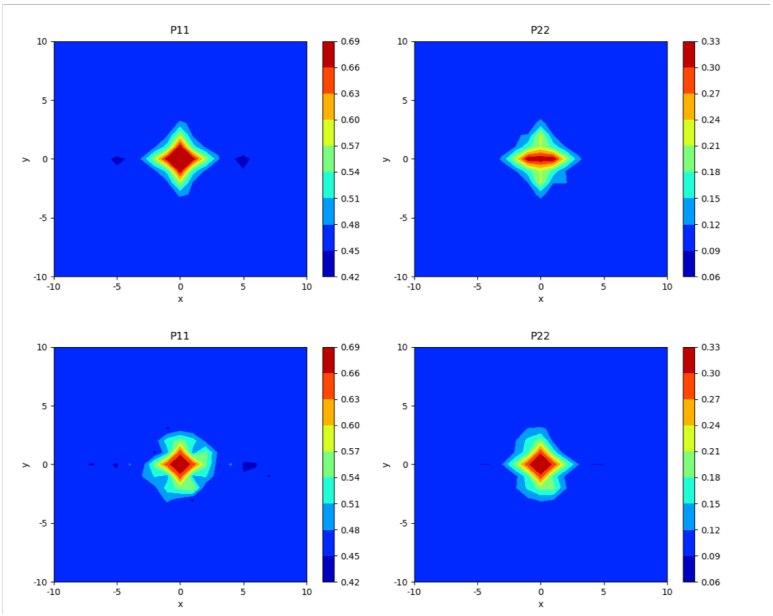

Strain of Final Microstructure	$(\eta - \eta_0)$	Strain of Initial Microstructure
50%	(50 – 20) = 30	20%

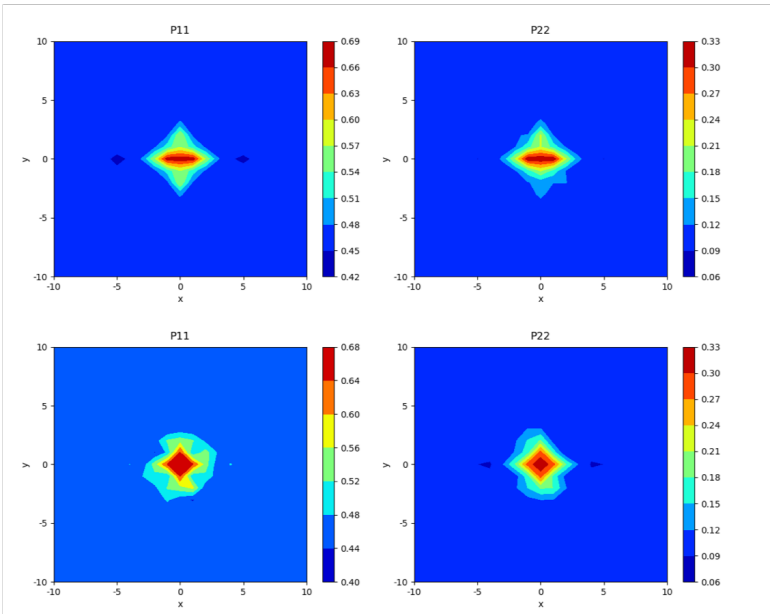

Strain of Final Microstructure	$(\eta - \eta_0)$	Strain of Initial Microstructure
50%	(50 – 10) = 40	10%

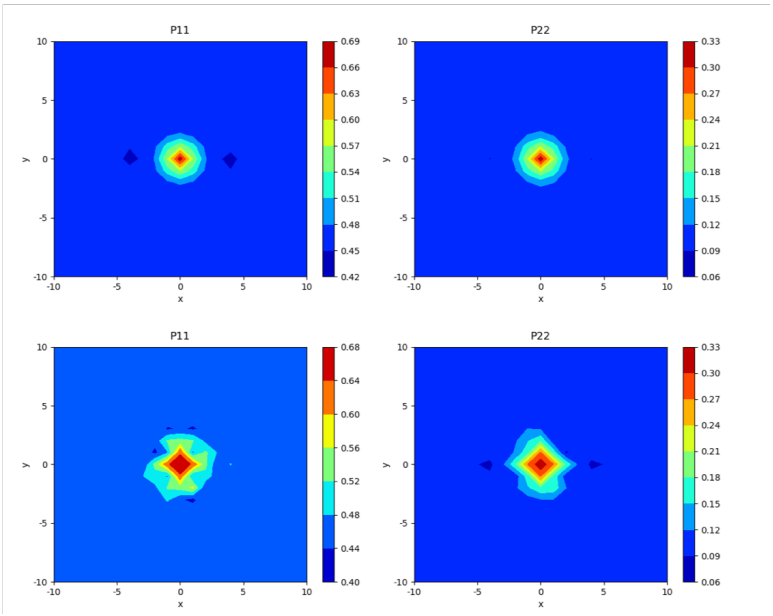

Strain of Final Microstructure	$(\eta - \eta_0)$	Strain of Initial Microstructure
50%	(50 – 0) = 50	0%

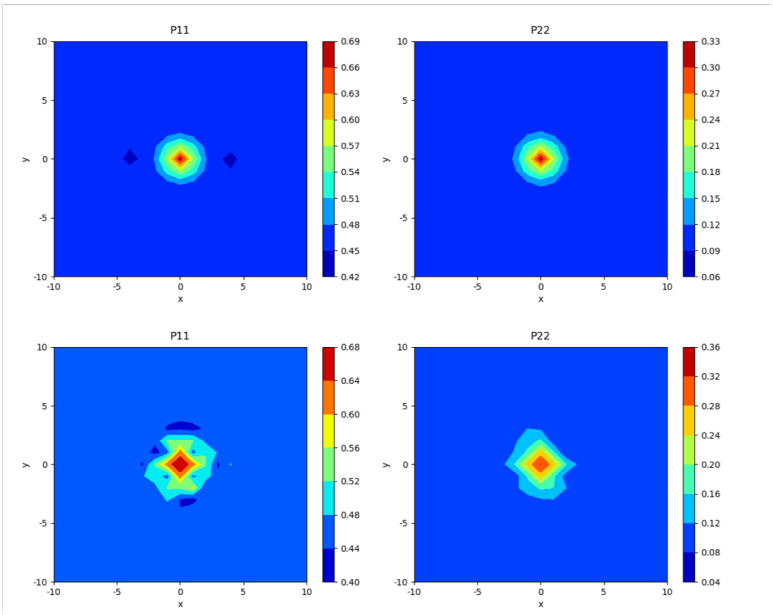

Strain of Final Microstructure	$(\eta - \eta_0)$	Strain of Initial Microstructure
40%	(40 – 30) = 10	30%

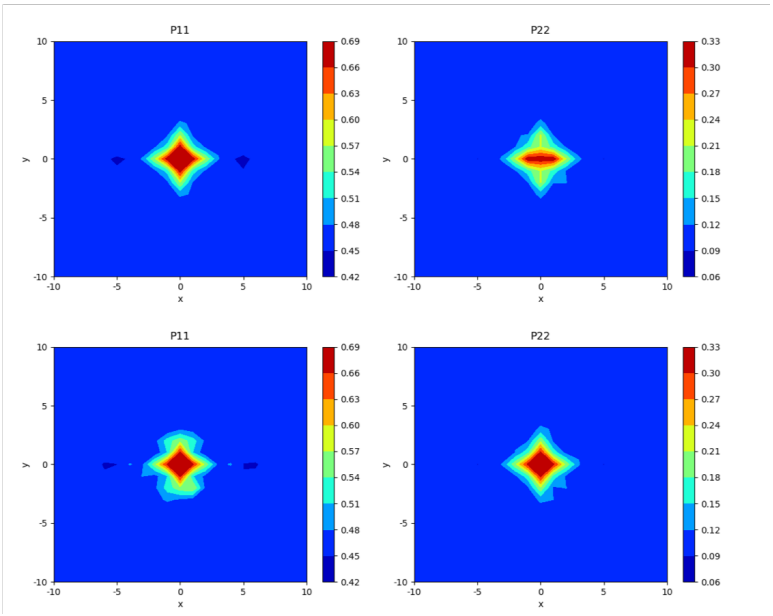

Strain of Final Microstructure	$(\eta - \eta_0)$	Strain of Initial Microstructure
40%	(40 – 20) = 20	20%

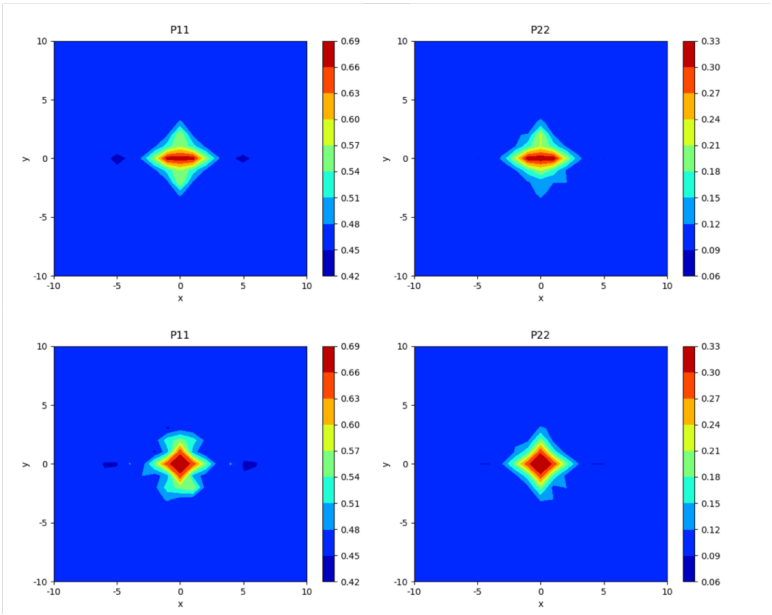

Strain of Final Microstructure	$(\eta - \eta_0)$	Strain of Initial Microstructure
40%	(40 – 10) = 30	10%

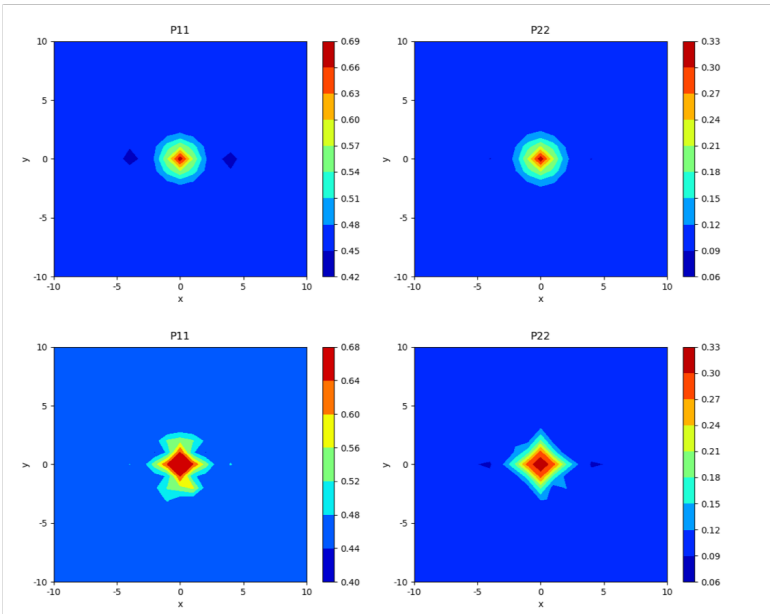

Strain of Final Microstructure	$(\eta - \eta_0)$	Strain of Initial Microstructure
40%	(40 – 0) = 40	0%

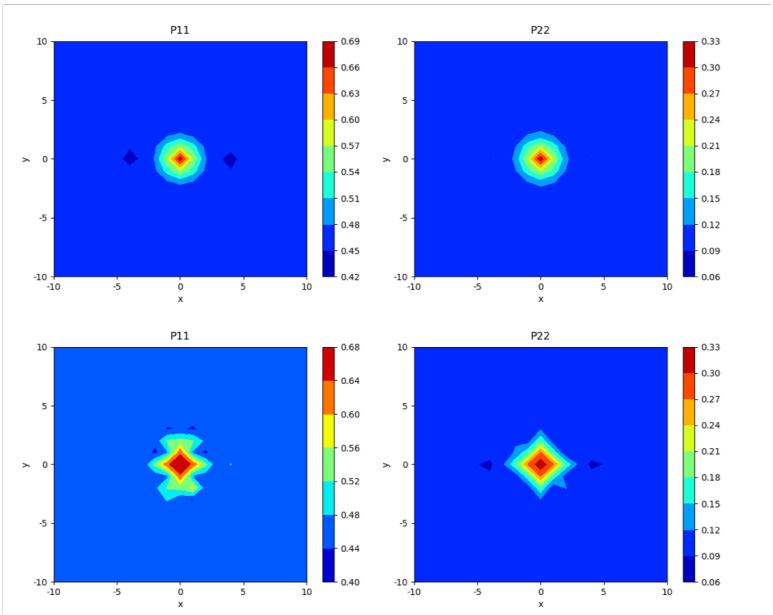

Strain of Final Microstructure	$(\eta - \eta_0)$	Strain of Initial Microstructure
30%	(30 – 20) = 10	20%

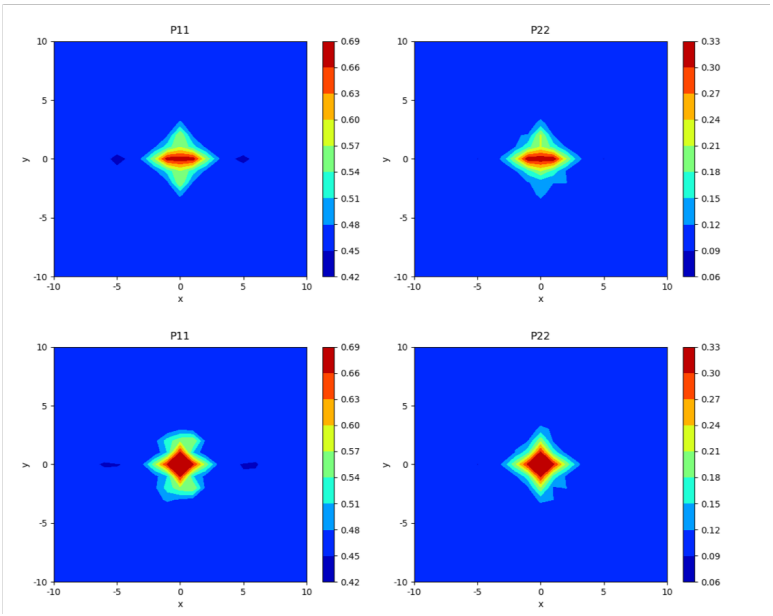

Strain of Final Microstructure	$(\eta - \eta_0)$	Strain of Initial Microstructure
30%	(30 – 10) = 20	10%

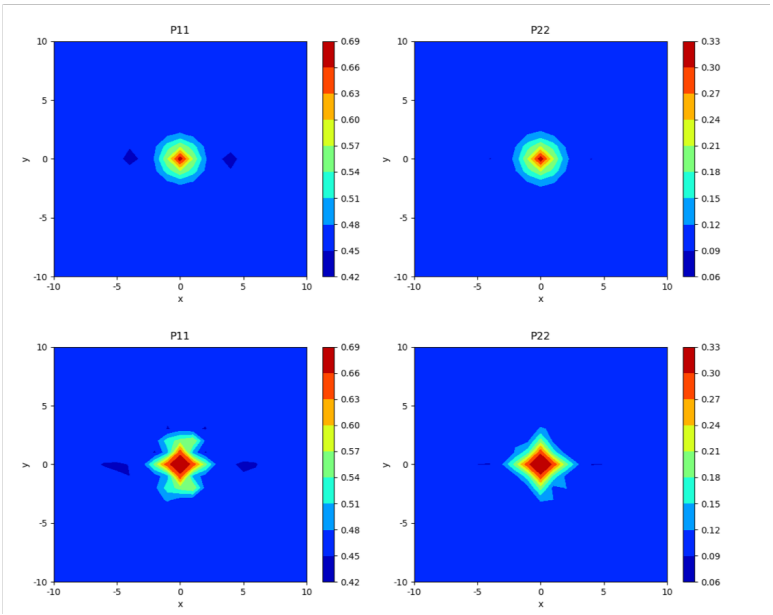

Strain of Final Microstructure	$(\eta - \eta_0)$	Strain of Initial Microstructure
30%	(30 – 0) = 30	0%

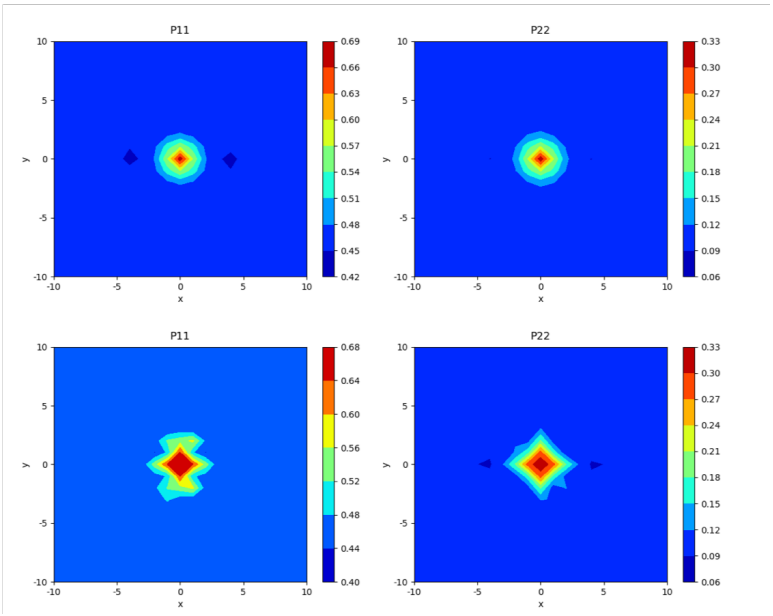

Strain of Final Microstructure	$(\eta - \eta_0)$	Strain of Initial Microstructure
20%	(20 – 10) = 10	10%

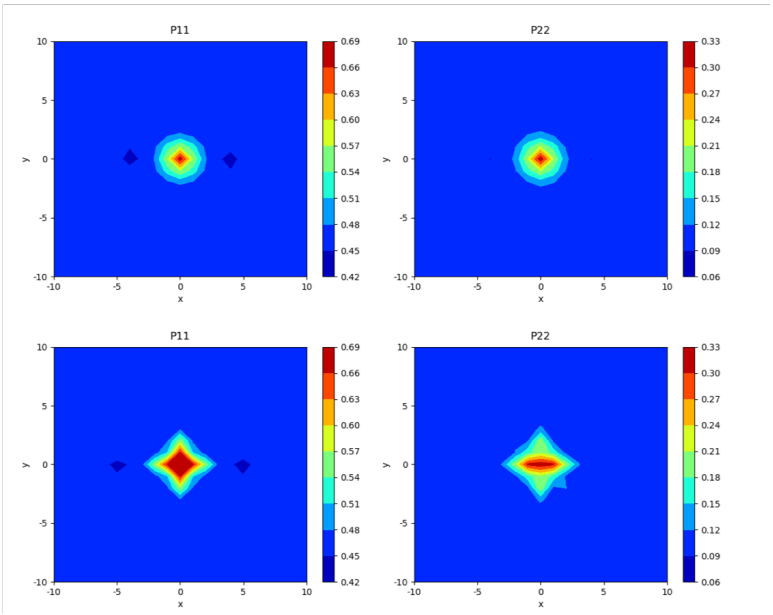

Strain of Final Microstructure	$(\eta - \eta_0)$	Strain of Initial Microstructure
20%	(20 – 0) = 20	0%

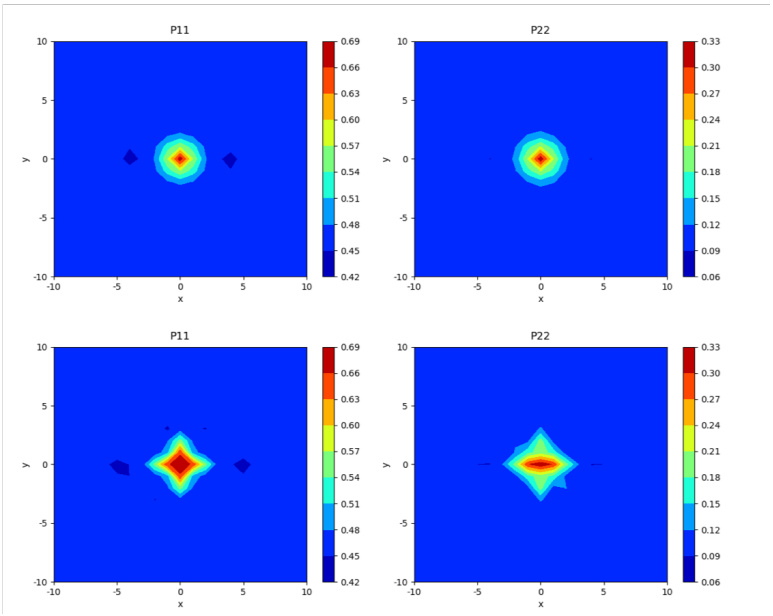

Strain of Final Microstructure	$(\eta - \eta_0)$	Strain of Initial Microstructure
10%	(10 – 0) = 10	0%

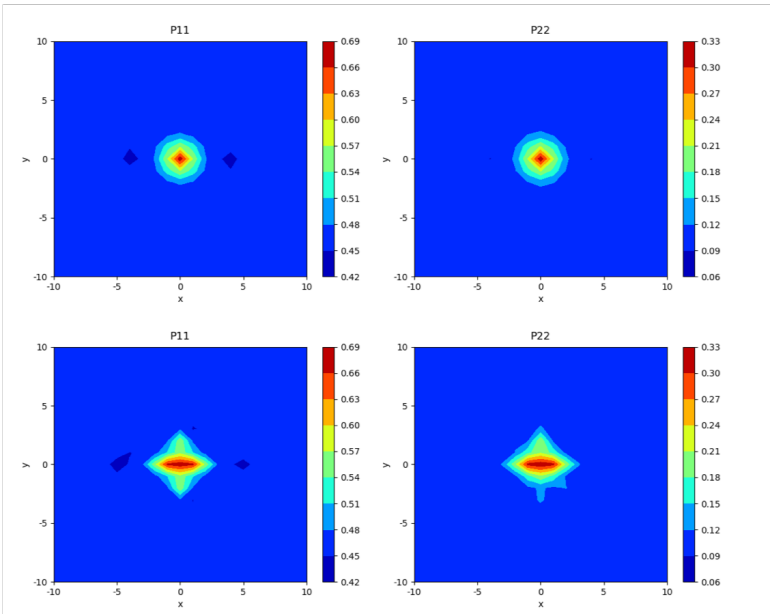

APPENDIX B. ERROR PLOTS OF THE INVERSE SIMULATION OF TWO-PHASE TWO-POINT STATISTICS

The figures illustrated in this appendix shows the error associated with each inverse simulation specified in **Appendix A**. Prior to each figure is a table which specifies the model parameters for the associated simulation as well as the average P11 and P22 error.

Strain of Final Microstructure	$(\eta - \eta_0)$	Strain of Initial Microstructure	Average P11 Error (%)	Average P22 Error (%)
100%	(100 – 90) = 10	90%	15.6	14.2

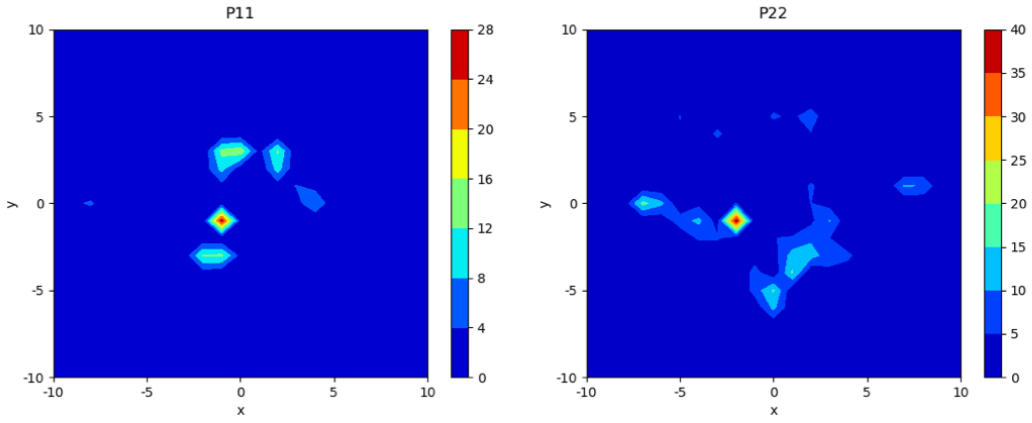

Strain of Final Microstructure	$(\eta - \eta_0)$	Strain of Initial Microstructure	Average P11 Error (%)	Average P22 Error (%)
100%	(100 – 80) = 20	80%	19.8	18.3

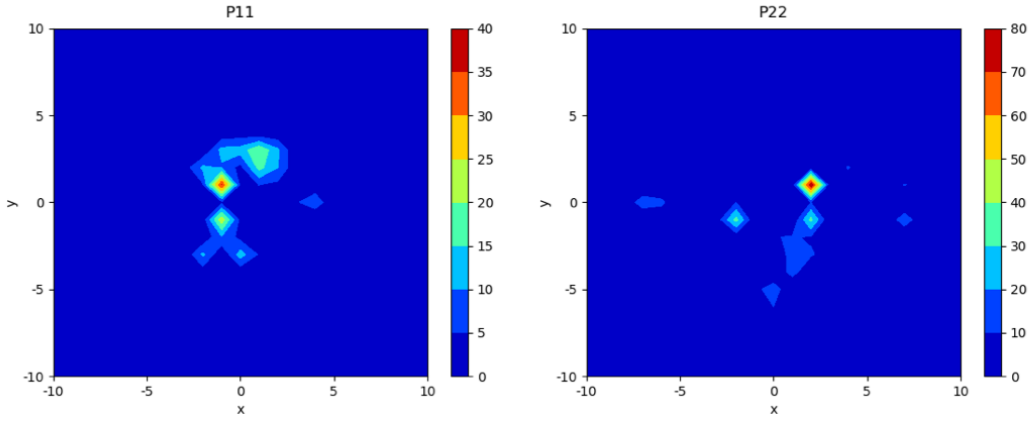

Strain of Final Microstructure	$(\eta - \eta_0)$	Strain of Initial Microstructure	Average P11 Error (%)	Average P22 Error (%)
100%	(100 – 70) = 30	70%	18.5	19.9

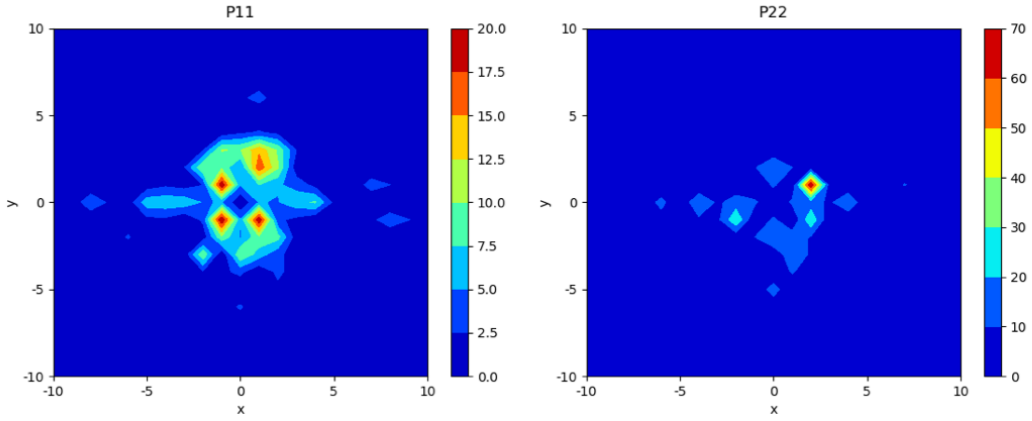

Strain of Final Microstructure	$(\eta - \eta_0)$	Strain of Initial Microstructure	Average P11 Error (%)	Average P22 Error (%)
100%	(100 – 60) = 40	60%	16.0	22.0

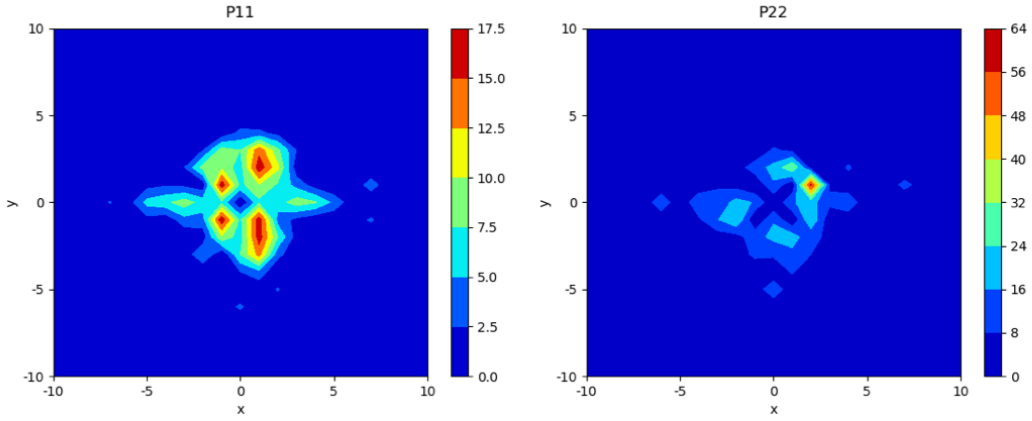

Strain of Final Microstructure	$(\eta - \eta_0)$	Strain of Initial Microstructure	Average P11 Error (%)	Average P22 Error (%)
100%	(100 – 50) = 50	50%	14.0	23.6

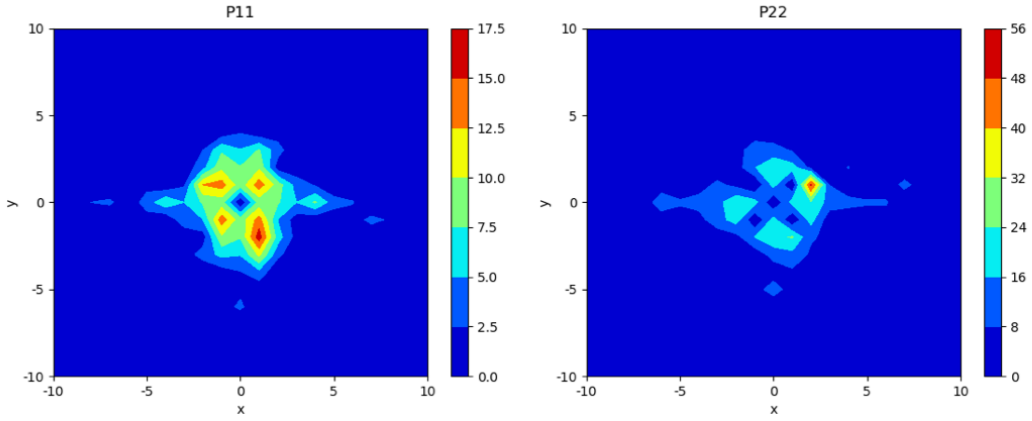

Strain of Final Microstructure	$(\eta - \eta_0)$	Strain of Initial Microstructure	Average P11 Error (%)	Average P22 Error (%)
100%	(100 – 40) = 60	40%	13.5	24.0

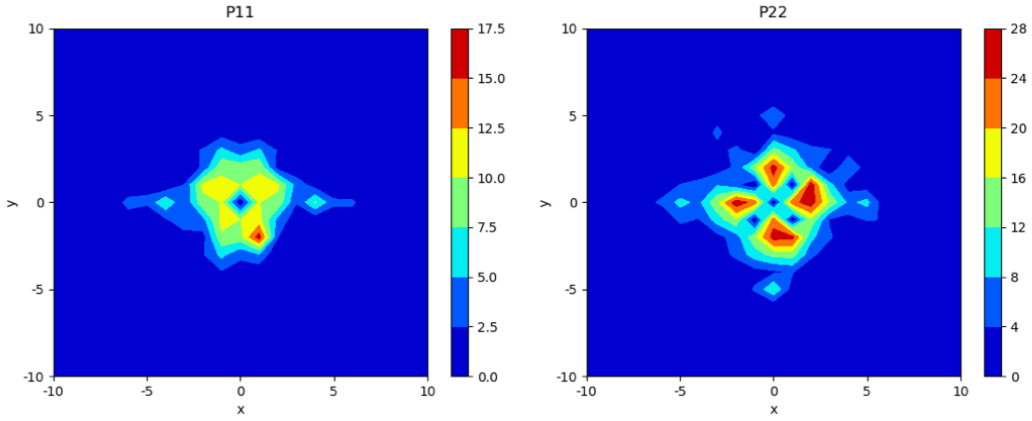

Strain of Final Microstructure	$(\eta - \eta_0)$	Strain of Initial Microstructure	Average P11 Error (%)	Average P22 Error (%)
100%	(100 – 30) = 70	30%	13.6	25.0

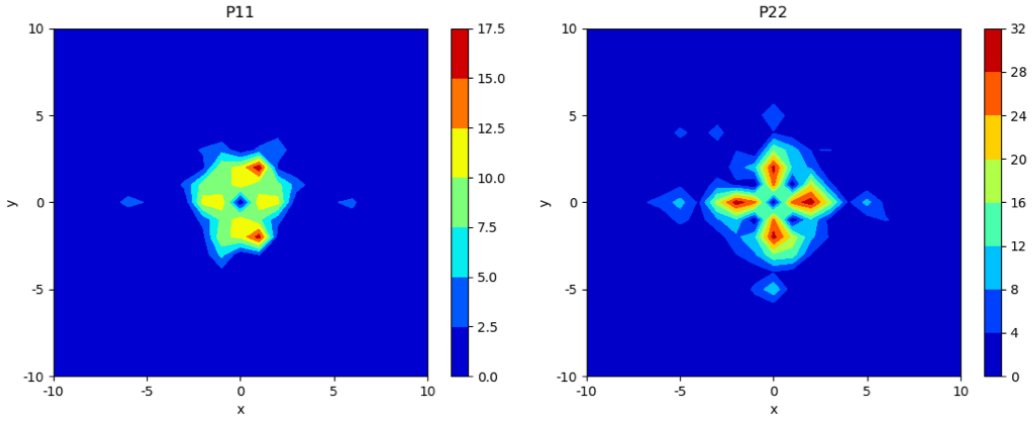

Strain of Final Microstructure	$(\eta - \eta_0)$	Strain of Initial Microstructure	Average P11 Error (%)	Average P22 Error (%)
100%	(100 – 20) = 80	20%	12.8	25.4

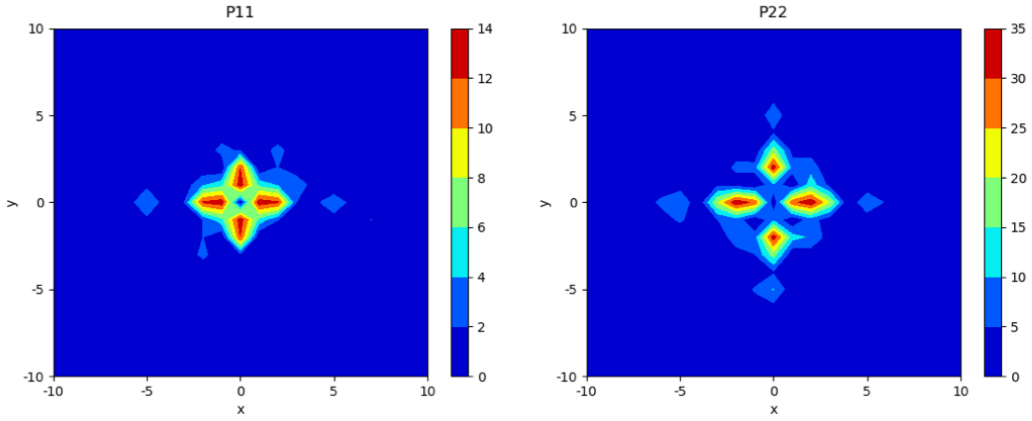

Strain of Final Microstructure	$(\eta - \eta_0)$	Strain of Initial Microstructure	Average P11 Error (%)	Average P22 Error (%)
100%	(100 – 10) = 90	10%	10.0	24.9

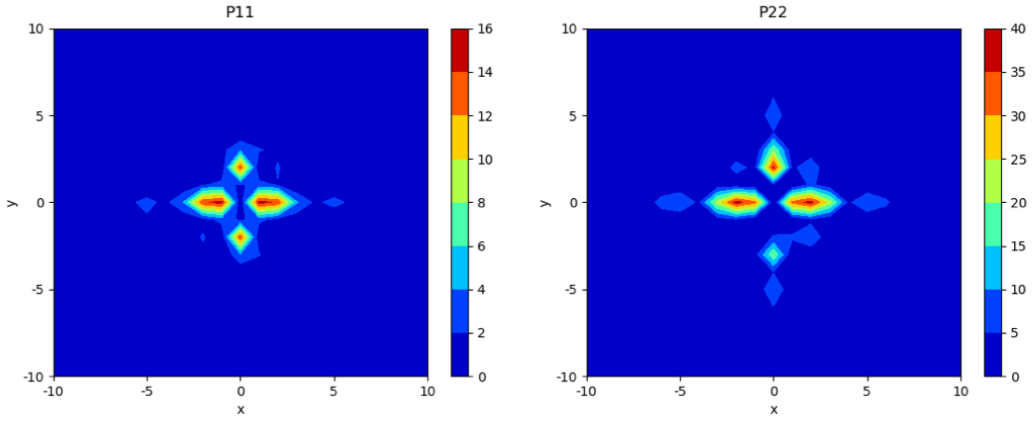

Strain of Final Microstructure	$(\eta - \eta_0)$	Strain of Initial Microstructure	Average P11 Error (%)	Average P22 Error (%)
100%	(100 – 0) = 100	0%	6.5×10^{-15}	5.41×10^{-15}

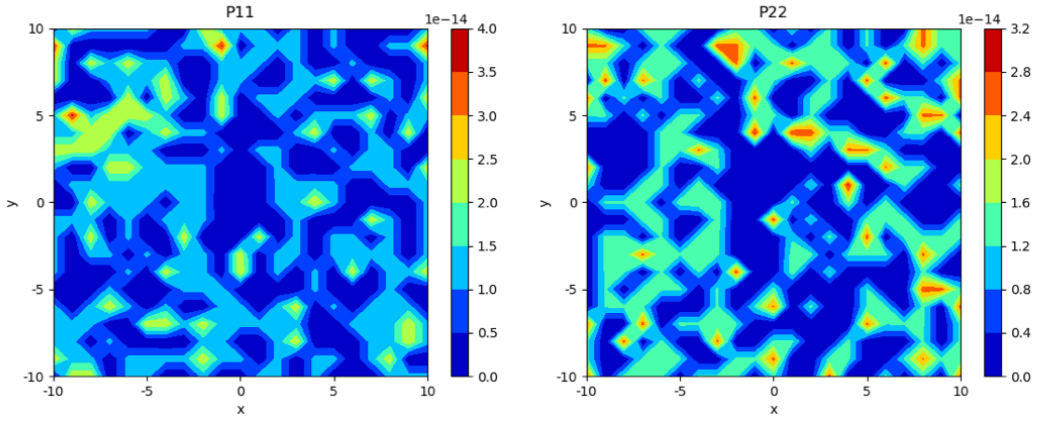

Strain of Final Microstructure	$(\eta - \eta_0)$	Strain of Initial Microstructure	Average P11 Error (%)	Average P22 Error (%)
90%	(90 – 80) = 10	80%	14.4	13.7

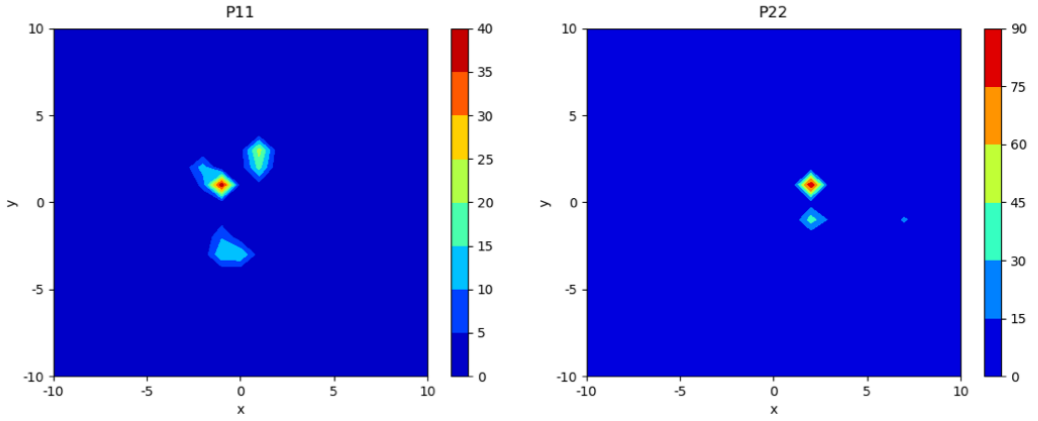

Strain of Final Microstructure	$(\eta - \eta_0)$	Strain of Initial Microstructure	Average P11 Error (%)	Average P22 Error (%)
90%	(90 – 70) = 20	70%	16.5	18.5

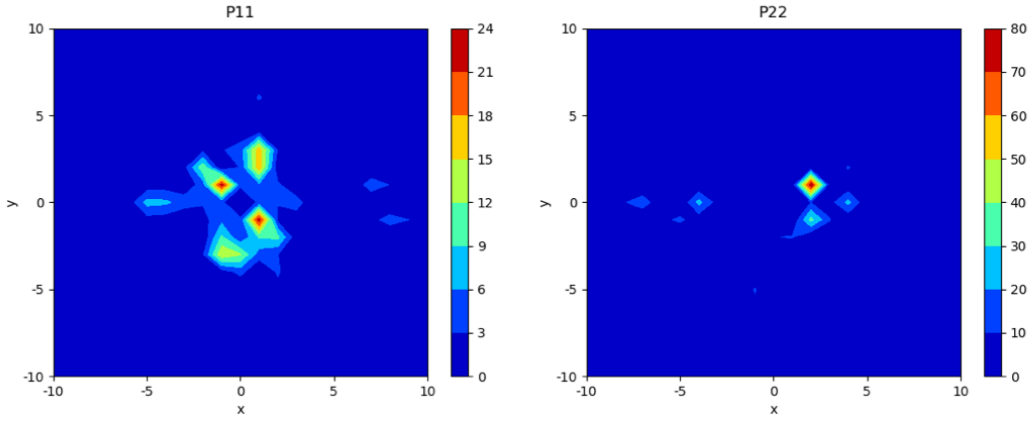

Strain of Final Microstructure	$(\eta - \eta_0)$	Strain of Initial Microstructure	Average P11 Error (%)	Average P22 Error (%)
90%	(90 – 60) = 30	60%	16.5	22.1

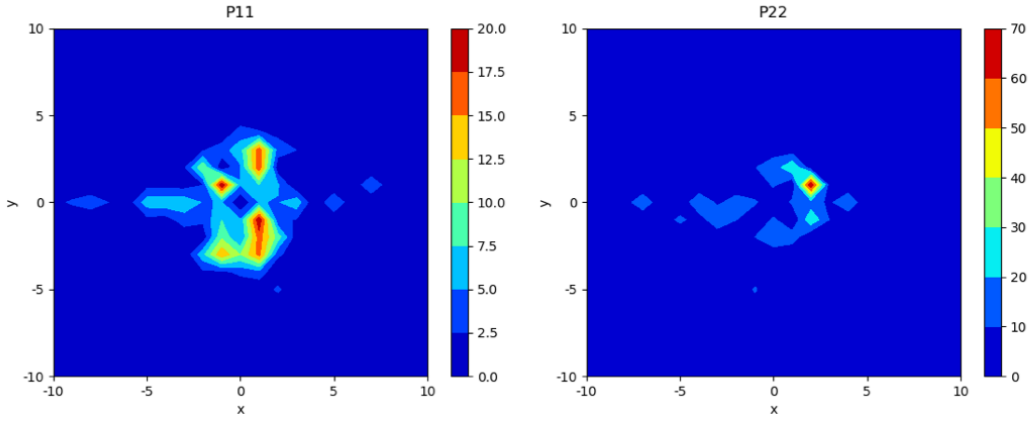

Strain of Final Microstructure	$(\eta - \eta_0)$	Strain of Initial Microstructure	Average P11 Error (%)	Average P22 Error (%)
90%	(90 – 50) = 40	50%	16.4	24.8

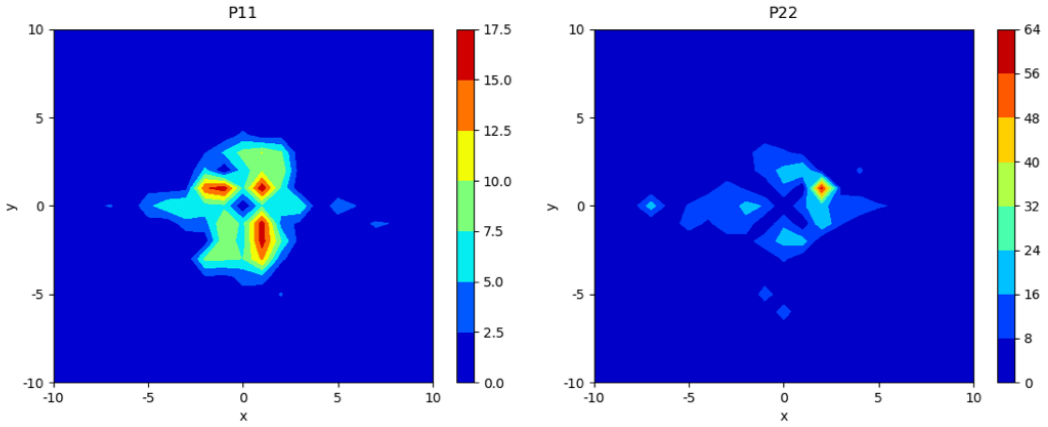

Strain of Final Microstructure	$(\eta - \eta_0)$	Strain of Initial Microstructure	Average P11 Error (%)	Average P22 Error (%)
90%	(90 – 40) = 50	40%	17.6	27.1

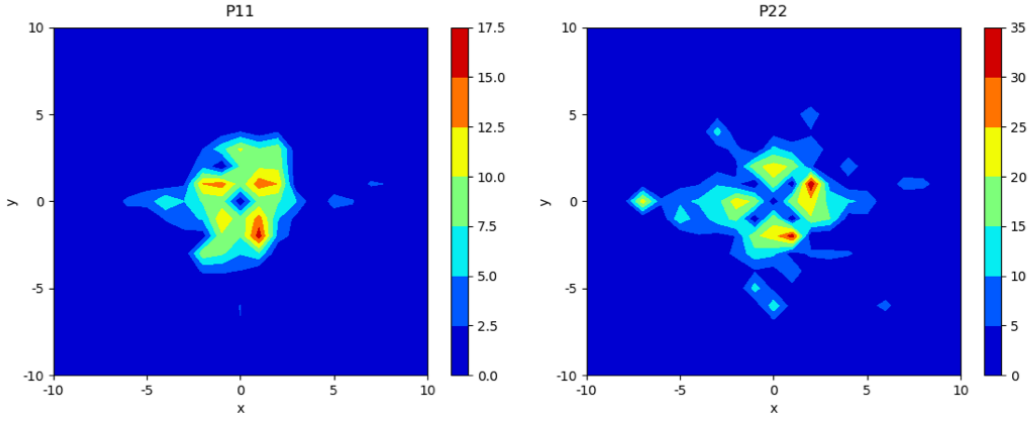

Strain of Final Microstructure	$(\eta - \eta_0)$	Strain of Initial Microstructure	Average P11 Error (%)	Average P22 Error (%)
90%	(90 – 30) = 60	30%	19.0	29.4

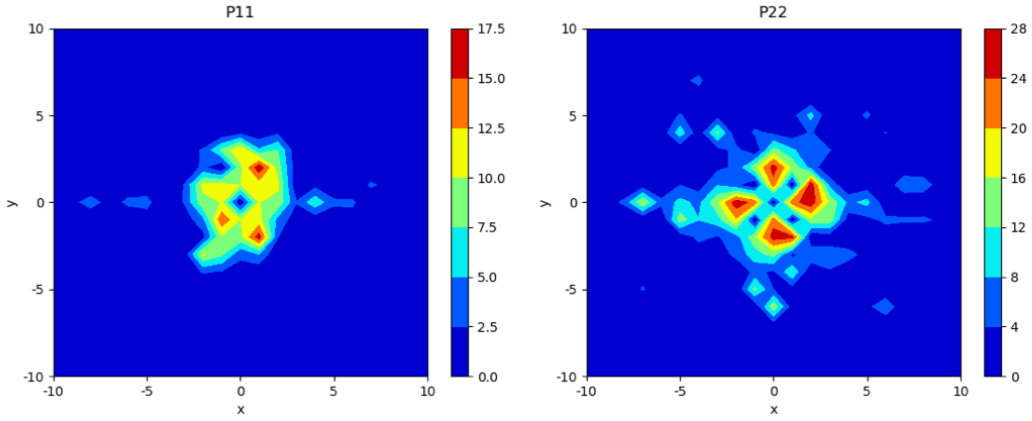

Strain of Final Microstructure	$(\eta - \eta_0)$	Strain of Initial Microstructure	Average P11 Error (%)	Average P22 Error (%)
90%	(90 – 20) = 70	20%	18.9	31.0

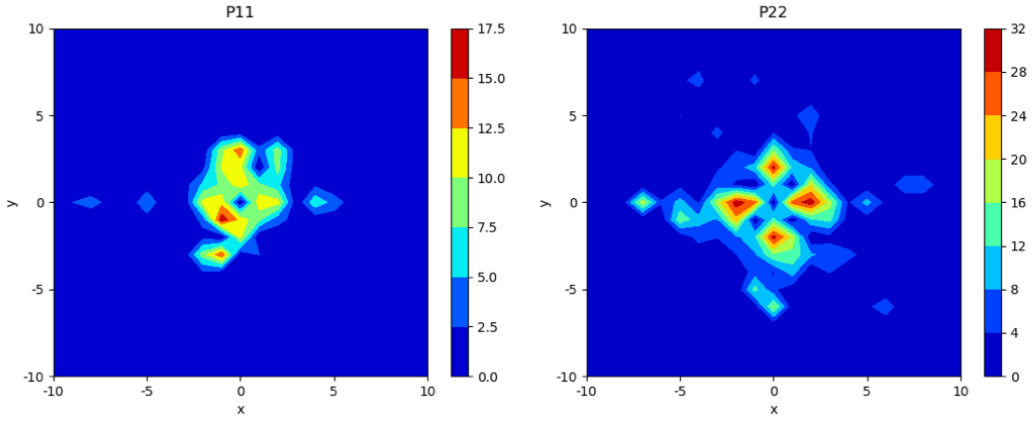

Strain of Final Microstructure	$(\eta - \eta_0)$	Strain of Initial Microstructure	Average P11 Error (%)	Average P22 Error (%)
90%	(90 – 10) = 80	10%	17.7	32.3

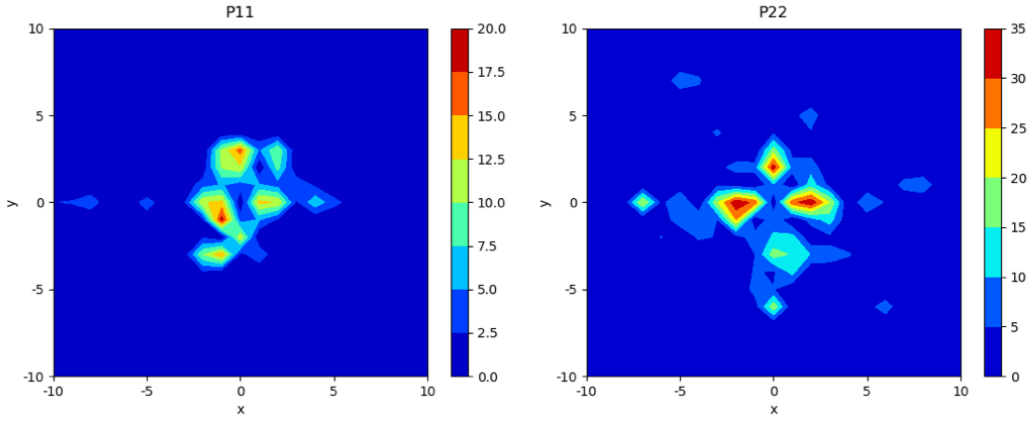

Strain of Final Microstructure	$(\eta - \eta_0)$	Strain of Initial Microstructure	Average P11 Error (%)	Average P22 Error (%)
90%	(90 – 0) = 90	0%	15.5	14.1

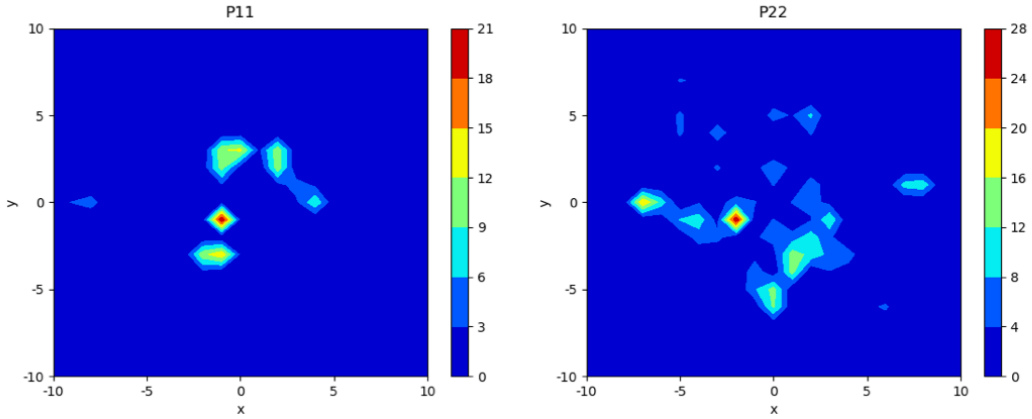

Strain of Final Microstructure	$(\eta - \eta_0)$	Strain of Initial Microstructure	Average P11 Error (%)	Average P22 Error (%)
80%	(80 – 70) = 10	70%	13.8	14.1

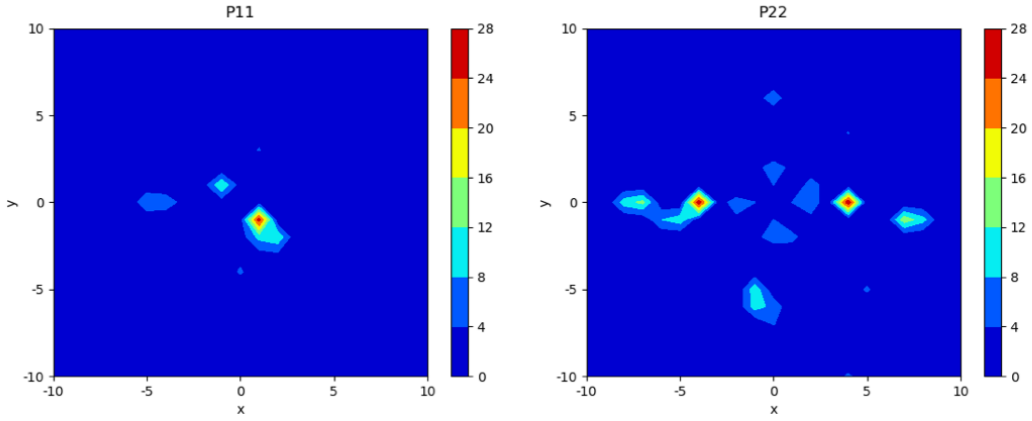

Strain of Final Microstructure	$(\eta - \eta_0)$	Strain of Initial Microstructure	Average P11 Error (%)	Average P22 Error (%)
80%	(80 – 60) = 20	60%	15.0	18.8

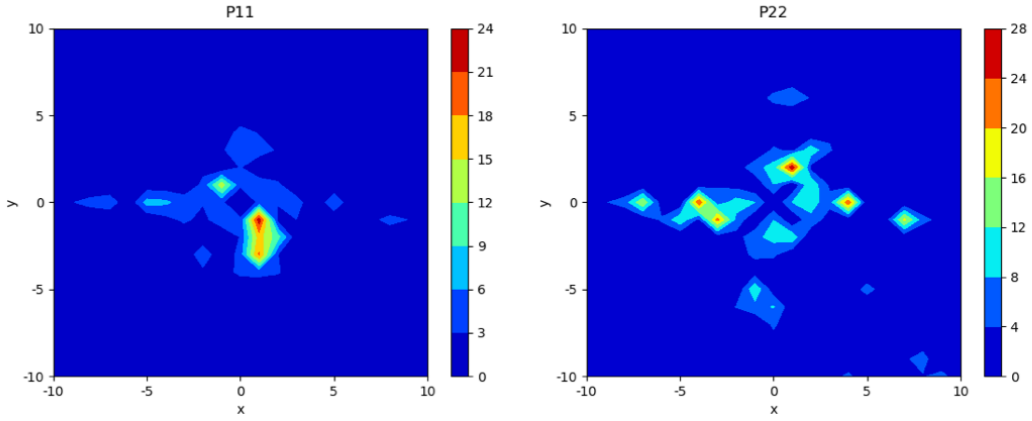

Strain of Final Microstructure	$(\eta - \eta_0)$	Strain of Initial Microstructure	Average P11 Error (%)	Average P22 Error (%)
80%	(80 – 50) = 30	50%	16.6	22.6

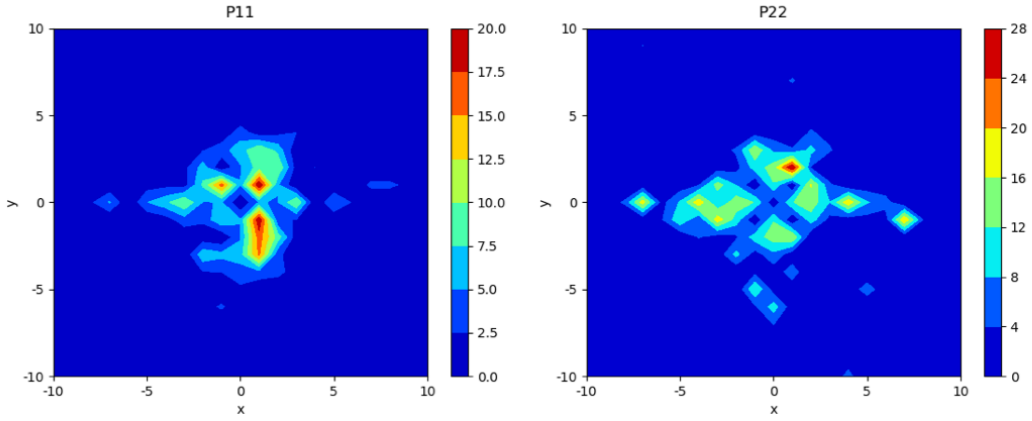

Strain of Final Microstructure	$(\eta - \eta_0)$	Strain of Initial Microstructure	Average P11 Error (%)	Average P22 Error (%)
80%	(80 – 40) = 40	40%	18.0	26.4

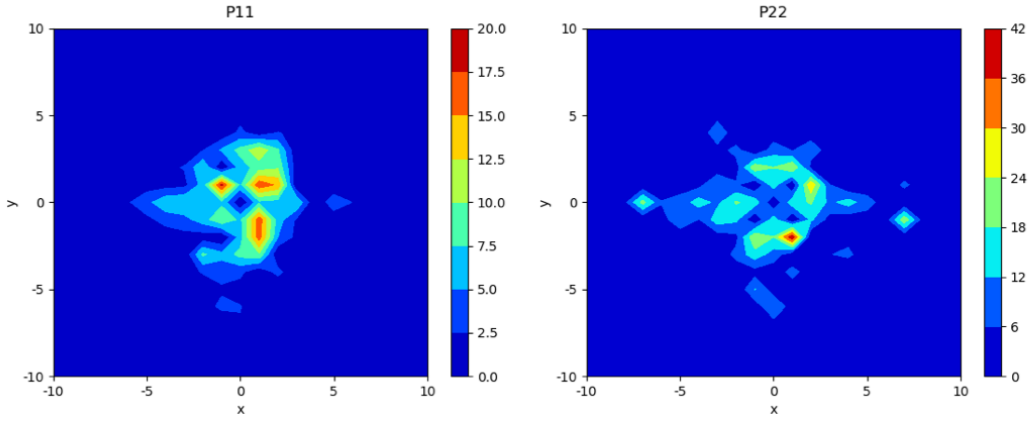

Strain of Final Microstructure	$(\eta - \eta_0)$	Strain of Initial Microstructure	Average P11 Error (%)	Average P22 Error (%)
80%	(80 – 30) = 50	30%	18.9	29.0

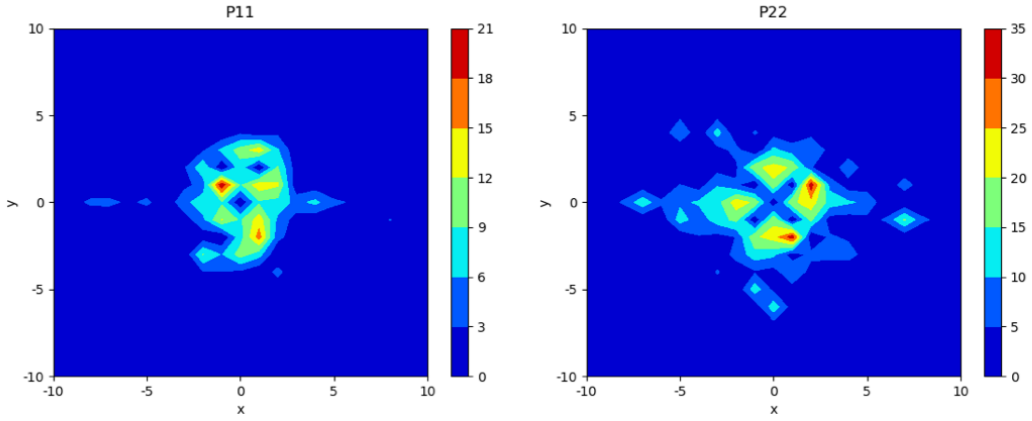

Strain of Final Microstructure	$(\eta - \eta_0)$	Strain of Initial Microstructure	Average P11 Error (%)	Average P22 Error (%)
80%	(80 – 20) = 60	20%	19.0	31.4

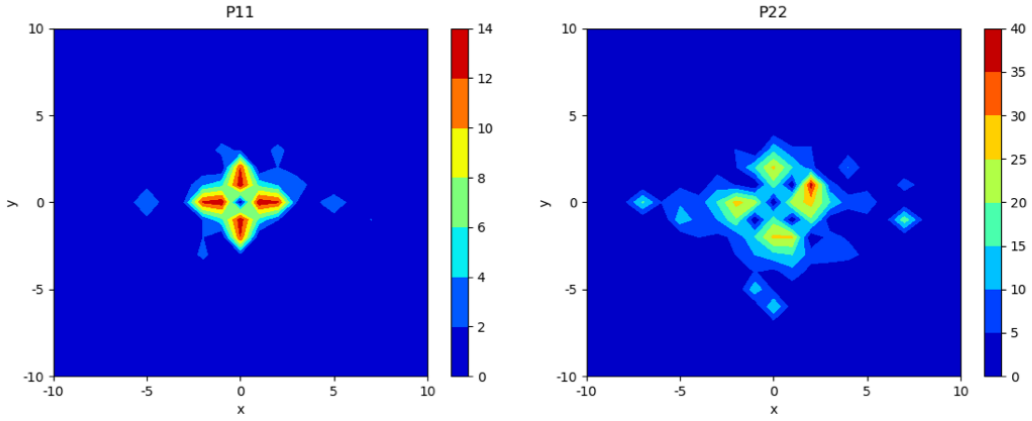

Strain of Final Microstructure	$(\eta - \eta_0)$	Strain of Initial Microstructure	Average P11 Error (%)	Average P22 Error (%)
80%	(80 – 10) = 70	10%	18.3	33.5

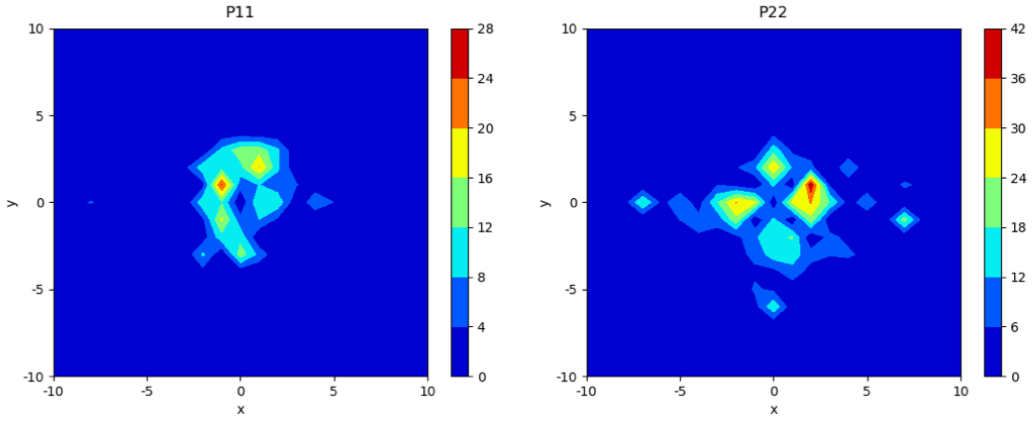

Strain of Final Microstructure	$(\eta - \eta_0)$	Strain of Initial Microstructure	Average P11 Error (%)	Average P22 Error (%)
80%	(80 – 0) = 80	0%	18.6	17.9

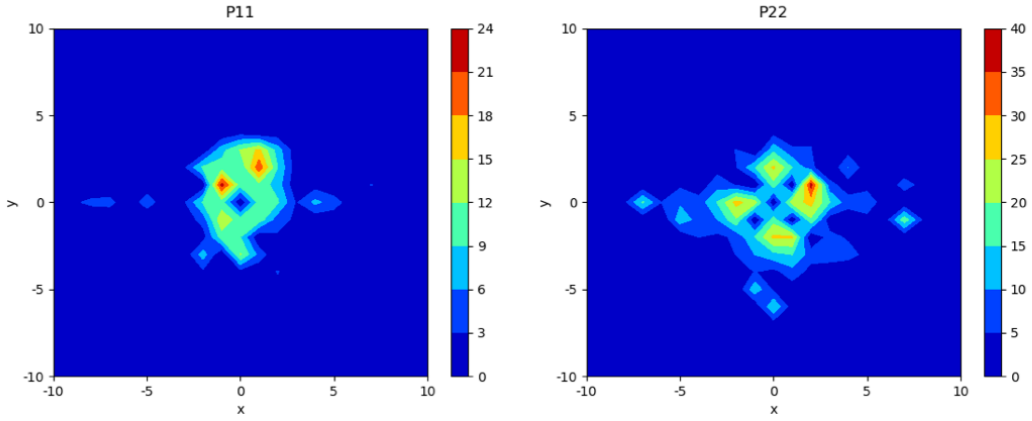

Strain of Final Microstructure	$(\eta - \eta_0)$	Strain of Initial Microstructure	Average P11 Error (%)	Average P22 Error (%)
70%	(70 – 60) = 10	60%	11.6	14.3

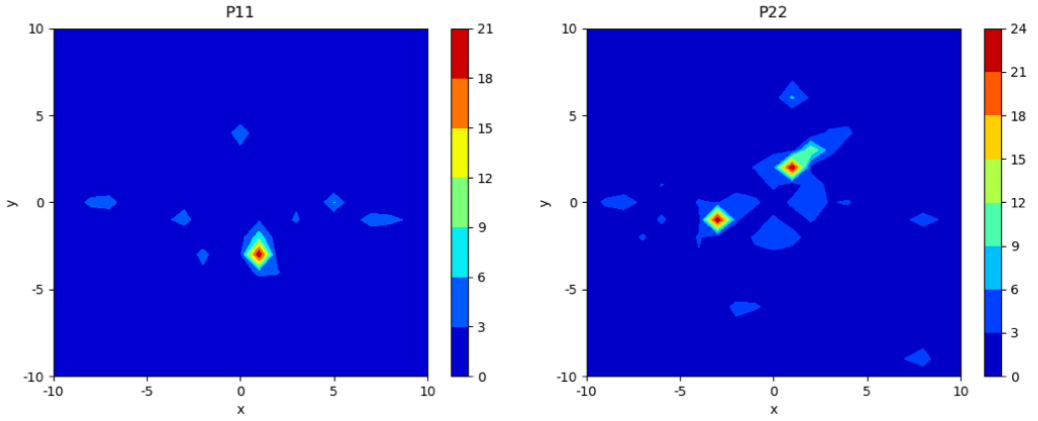

Strain of Final Microstructure	$(\eta - \eta_0)$	Strain of Initial Microstructure	Average P11 Error (%)	Average P22 Error (%)
70%	(70 – 50) = 20	50%	14.3	19.6

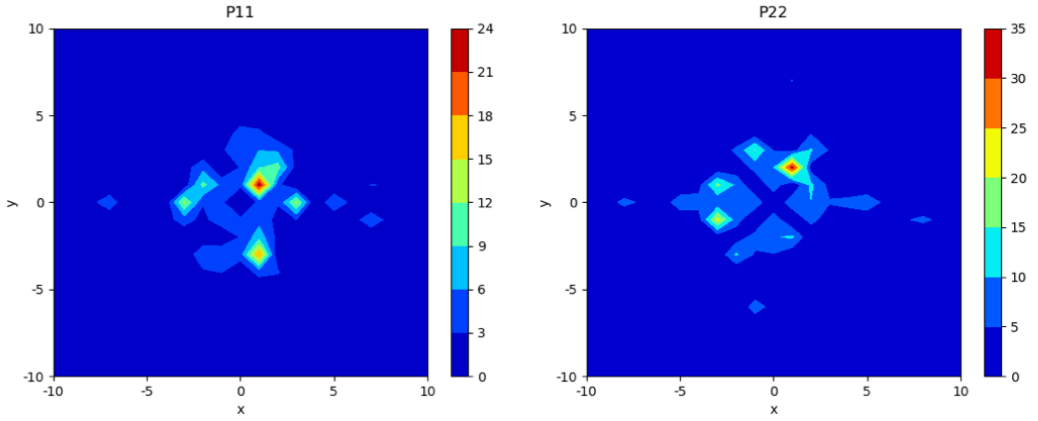

Strain of Final Microstructure	$(\eta - \eta_0)$	Strain of Initial Microstructure	Average P11 Error (%)	Average P22 Error (%)
70%	(70 – 40) = 30	40%	15.4	24.3

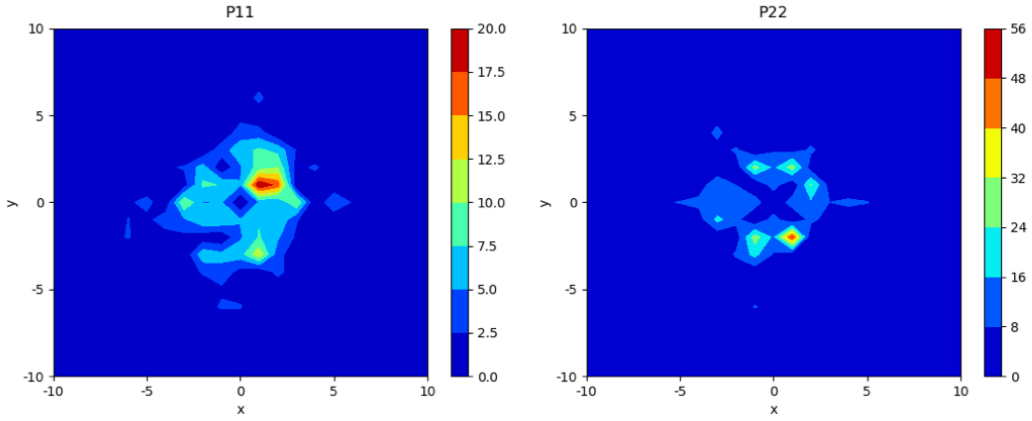

Strain of Final Microstructure	$(\eta - \eta_0)$	Strain of Initial Microstructure	Average P11 Error (%)	Average P22 Error (%)
70%	(70 – 30) = 40	30%	15.7	27.5

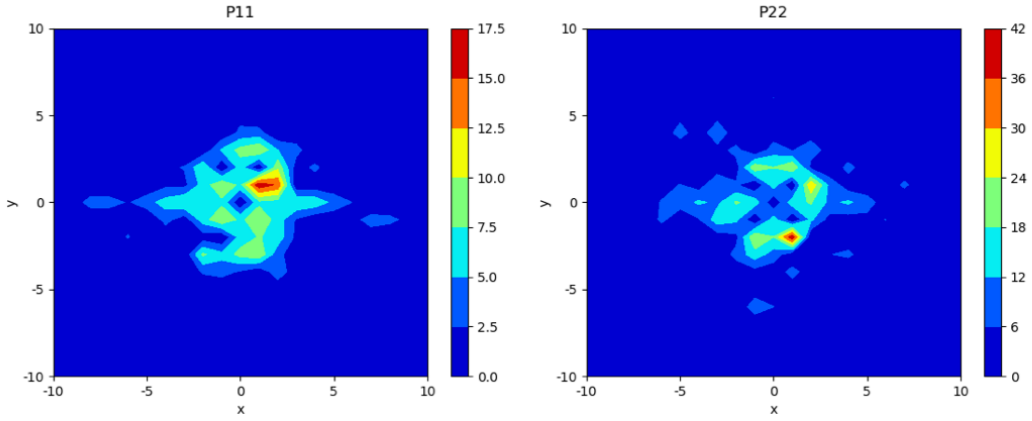

Strain of Final Microstructure	$(\eta - \eta_0)$	Strain of Initial Microstructure	Average P11 Error (%)	Average P22 Error (%)
70%	(70 – 20) = 50	20%	16.7	30.9

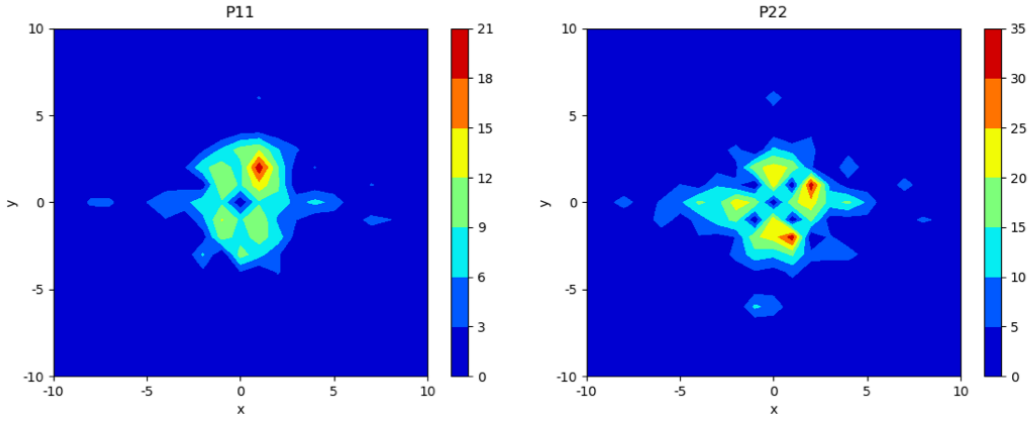

Strain of Final Microstructure	$(\eta - \eta_0)$	Strain of Initial Microstructure	Average P11 Error (%)	Average P22 Error (%)
70%	(70 – 10) = 60	10%	18.8	33.3

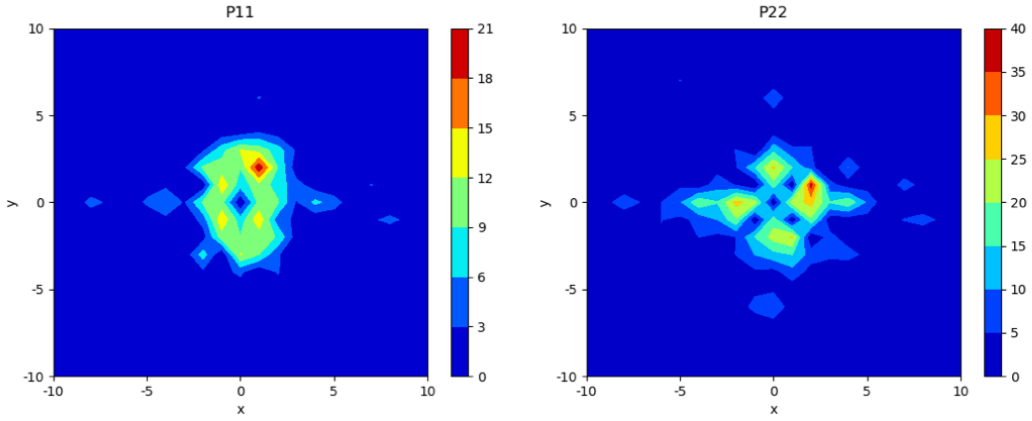

Strain of Final Microstructure	$(\eta - \eta_0)$	Strain of Initial Microstructure	Average P11 Error (%)	Average P22 Error (%)
70%	(70 – 0) = 70	0%	18.4	19.7

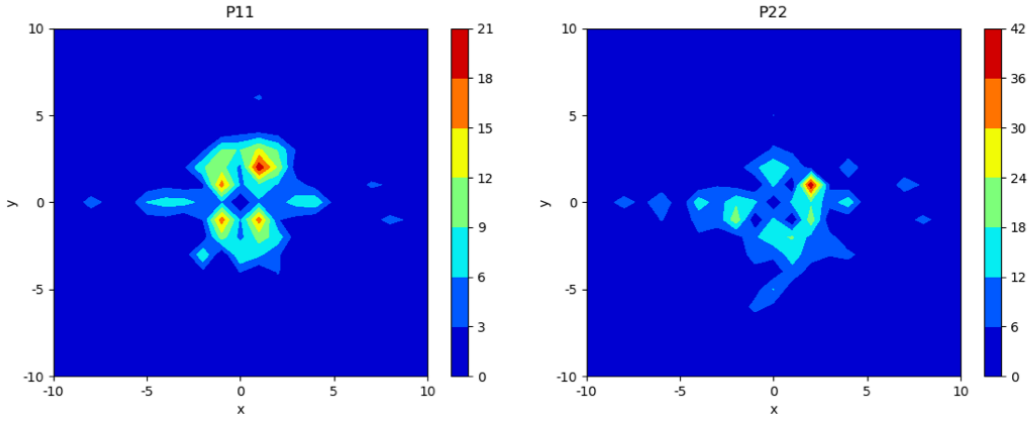

Strain of Final Microstructure	$(\eta - \eta_0)$	Strain of Initial Microstructure	Average P11 Error (%)	Average P22 Error (%)
60%	(60 – 50) = 10	50%	9.04	16.2

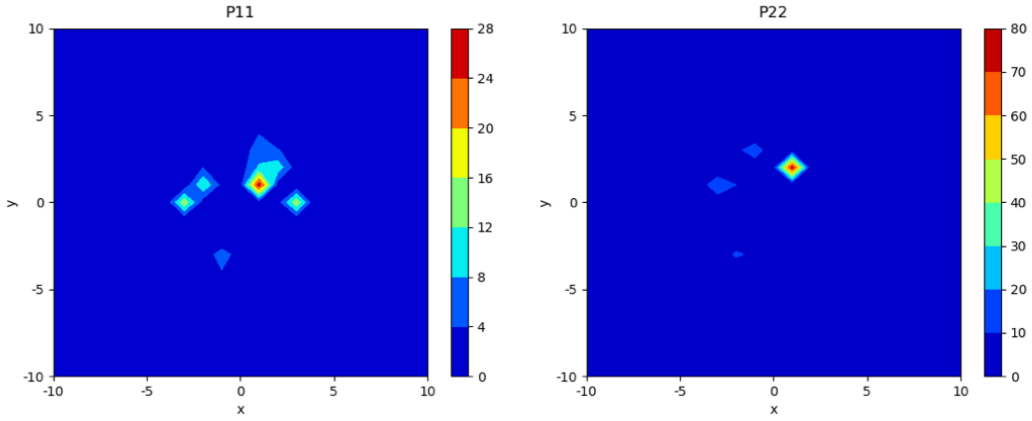

Strain of Final Microstructure	$(\eta - \eta_0)$	Strain of Initial Microstructure	Average P11 Error (%)	Average P22 Error (%)
60%	(60 – 40) = 20	40%	11.5	22.5

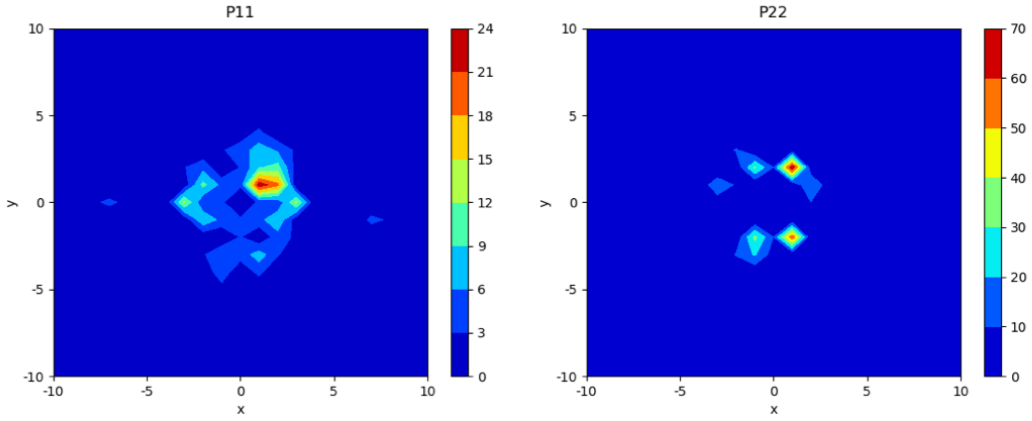

Strain of Final Microstructure	$(\eta - \eta_0)$	Strain of Initial Microstructure	Average P11 Error (%)	Average P22 Error (%)
60%	(60 – 30) = 30	30%	14.5	26.3

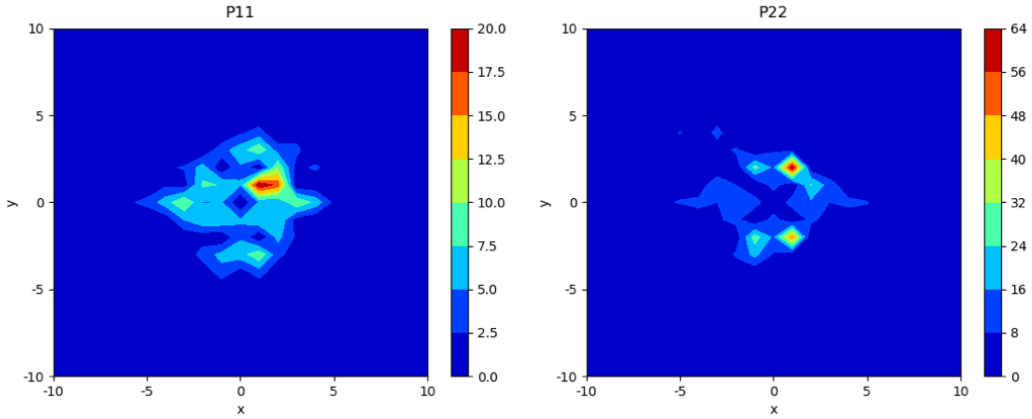

Strain of Final Microstructure	$(\eta - \eta_0)$	Strain of Initial Microstructure	Average P11 Error (%)	Average P22 Error (%)
60%	(60 – 20) = 40	20%	17.6	30.3

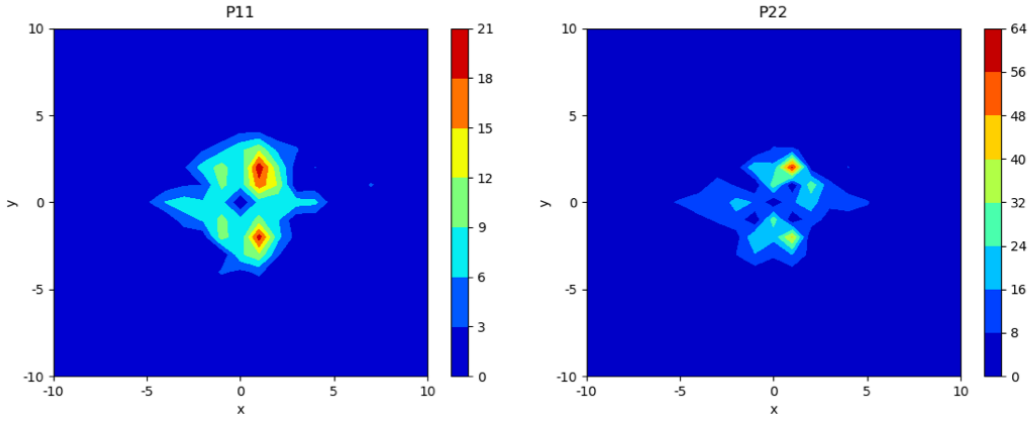

Strain of Final Microstructure	$(\eta - \eta_0)$	Strain of Initial Microstructure	Average P11 Error (%)	Average P22 Error (%)
60%	(60 – 10) = 50	10%	18.0	33.4

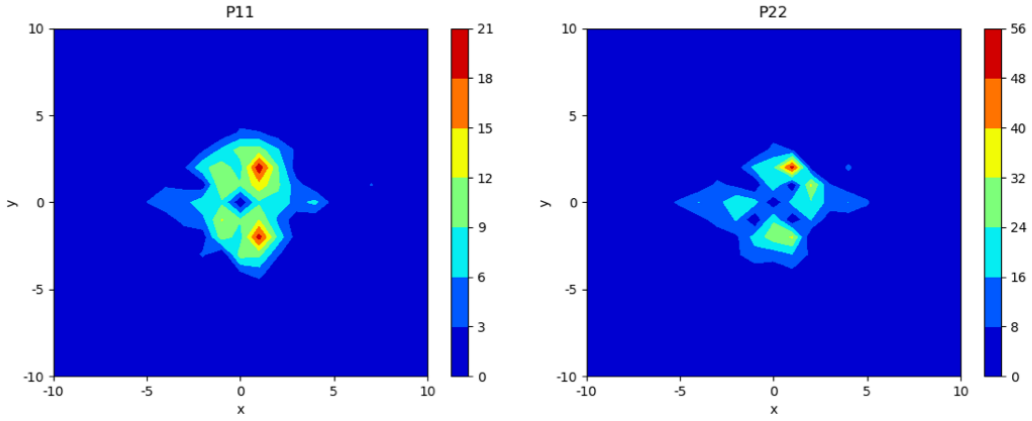

Strain of Final Microstructure	$(\eta - \eta_0)$	Strain of Initial Microstructure	Average P11 Error (%)	Average P22 Error (%)
60%	(60 – 0) = 60	0%	16.0	22.1

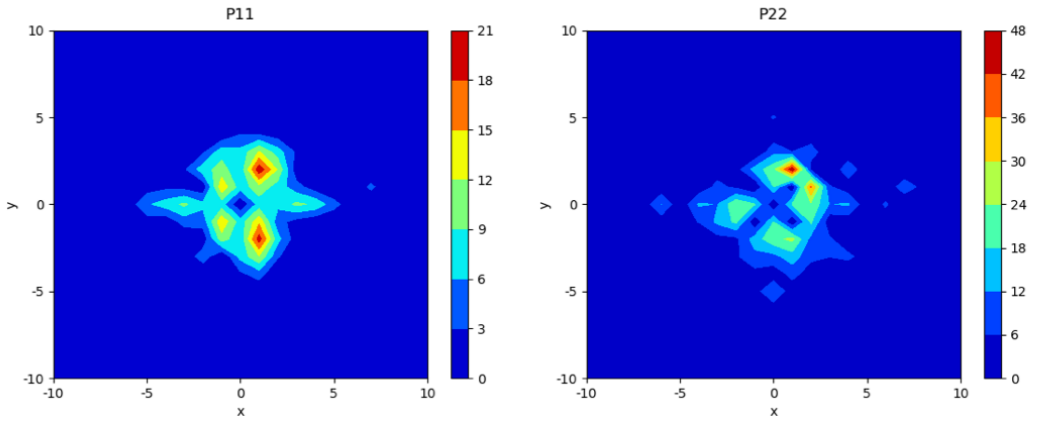

Strain of Final Microstructure	$(\eta - \eta_0)$	Strain of Initial Microstructure	Average P11 Error (%)	Average P22 Error (%)
50%	(50 – 40) = 10	40%	8.89	18.5

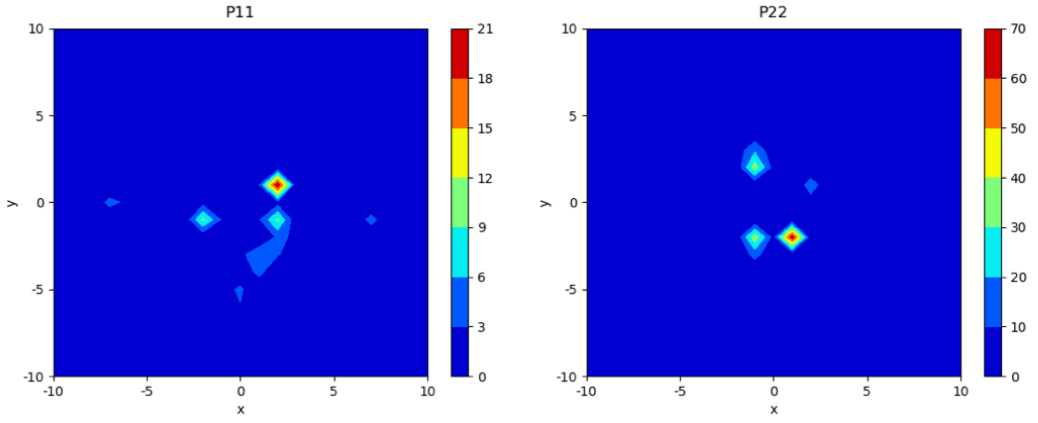

Strain of Final Microstructure	$(\eta - \eta_0)$	Strain of Initial Microstructure	Average P11 Error (%)	Average P22 Error (%)
50%	(50 – 30) = 20	30%	12.9	23.8

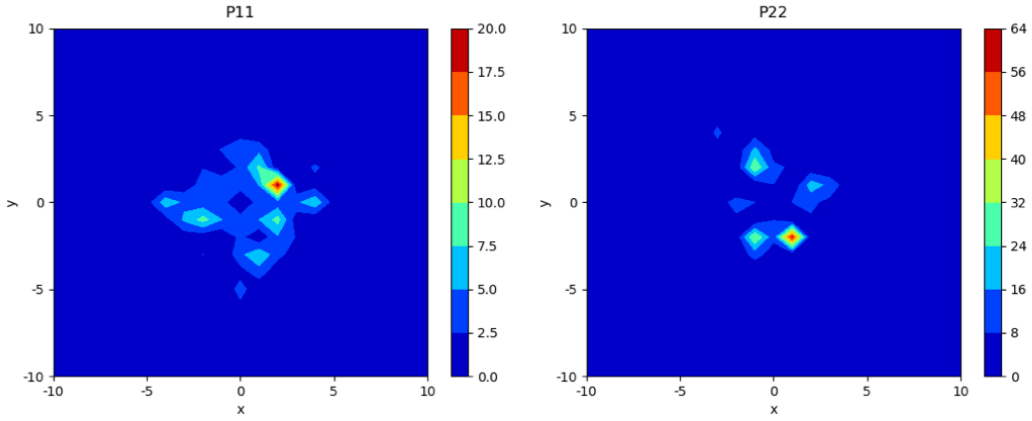

Strain of Final Microstructure	$(\eta - \eta_0)$	Strain of Initial Microstructure	Average P11 Error (%)	Average P22 Error (%)
50%	(50 – 20) = 30	20%	15.7	28.5

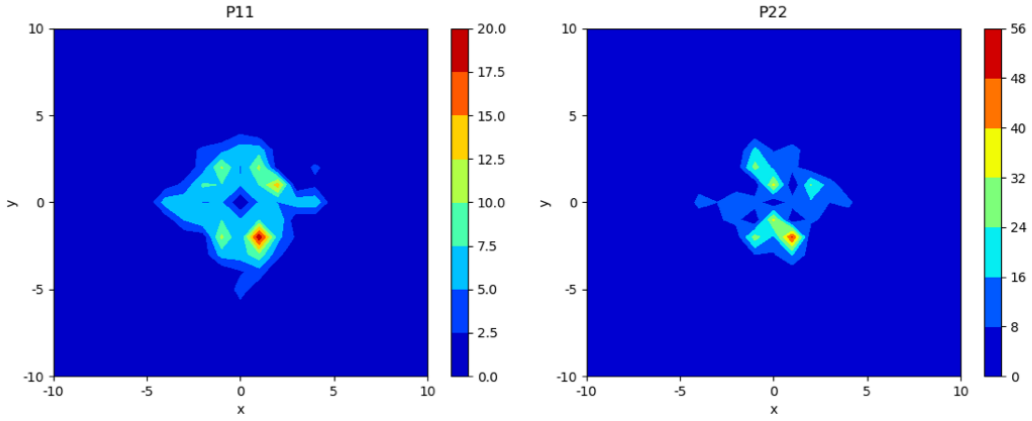

Strain of Final Microstructure	$(\eta - \eta_0)$	Strain of Initial Microstructure	Average P11 Error (%)	Average P22 Error (%)
50%	(50 – 10) = 40	10%	16.2	32.3

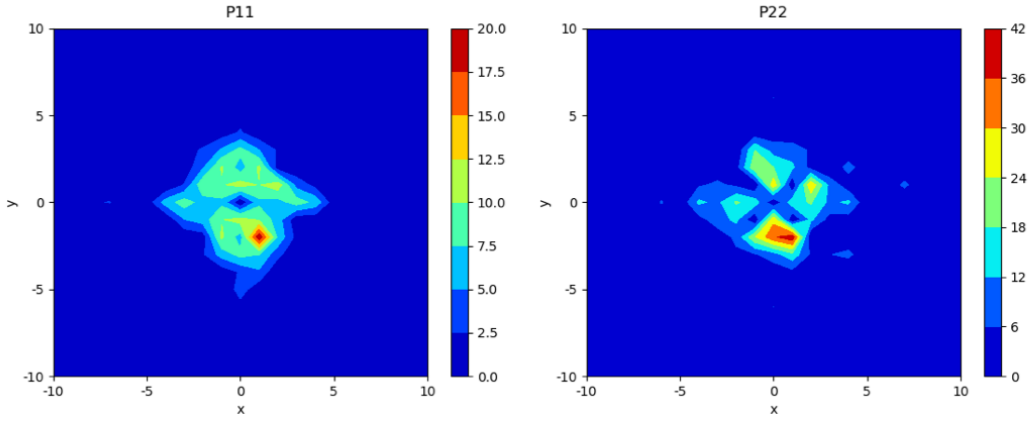

Strain of Final Microstructure	$(\eta - \eta_0)$	Strain of Initial Microstructure	Average P11 Error (%)	Average P22 Error (%)
50%	(50 – 0) = 50	0%	14.0	23.9

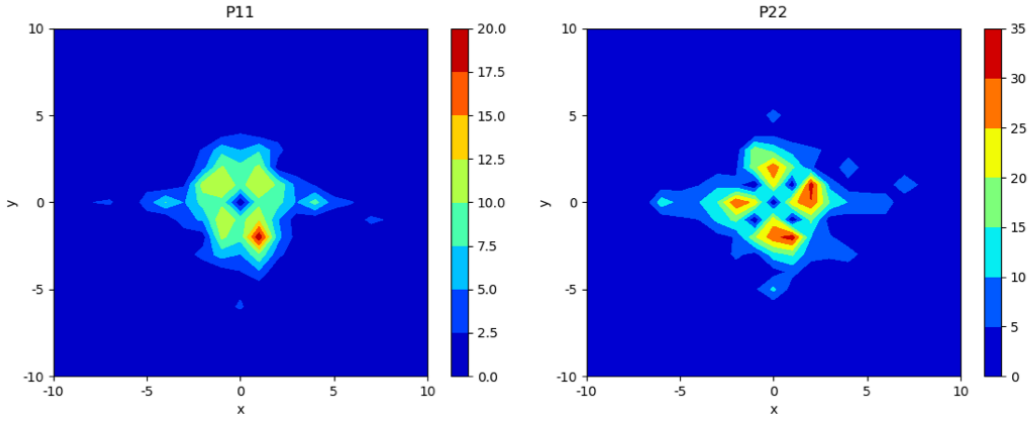

Strain of Final Microstructure	$(\eta - \eta_0)$	Strain of Initial Microstructure	Average P11 Error (%)	Average P22 Error (%)
40%	(40 – 30) = 10	30%	9.14	18.2

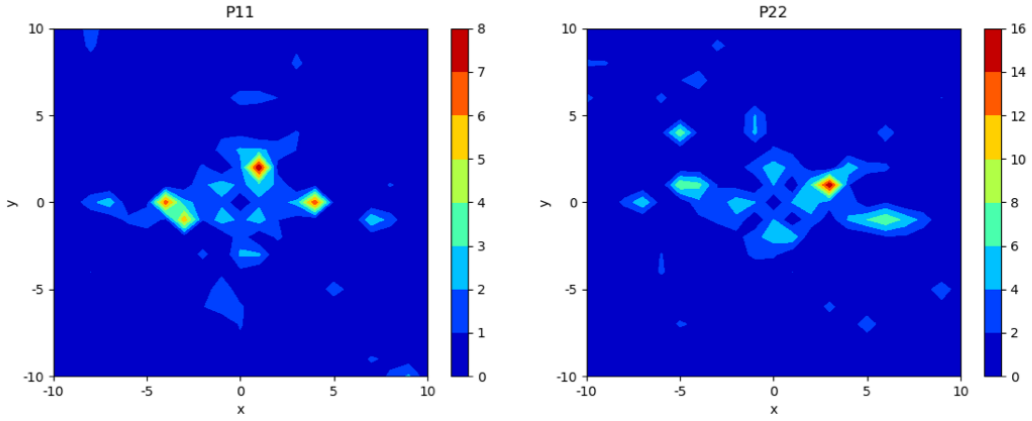

Strain of Final Microstructure	$(\eta - \eta_0)$	Strain of Initial Microstructure	Average P11 Error (%)	Average P22 Error (%)
40%	(40 – 20) = 20	20%	13.4	25.0

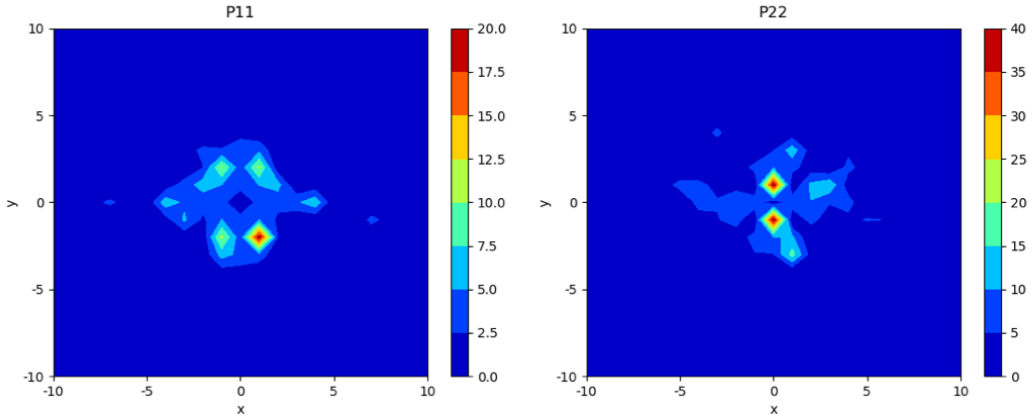

Strain of Final Microstructure	$(\eta - \eta_0)$	Strain of Initial Microstructure	Average P11 Error (%)	Average P22 Error (%)
40%	(40 – 10) = 30	10%	15.0	30.1

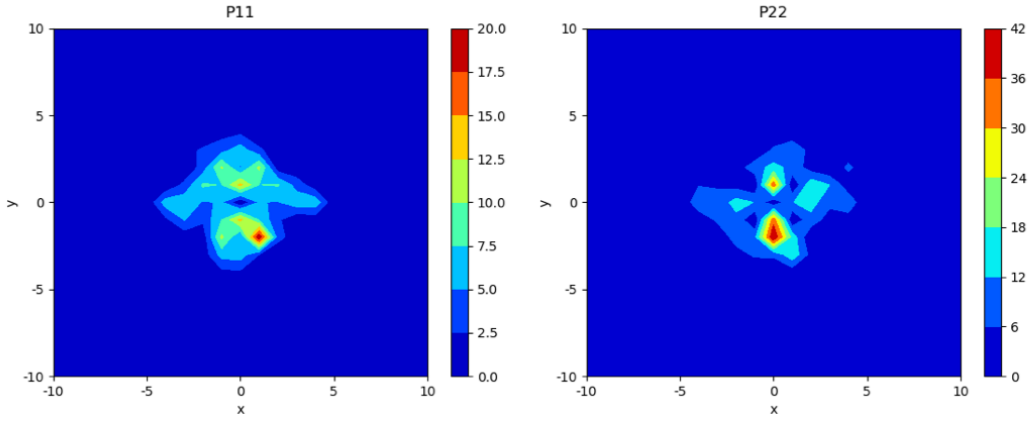

Strain of Final Microstructure	$(\eta - \eta_0)$	Strain of Initial Microstructure	Average P11 Error (%)	Average P22 Error (%)
40%	(40 – 0) = 40	0%	13.5	24.5

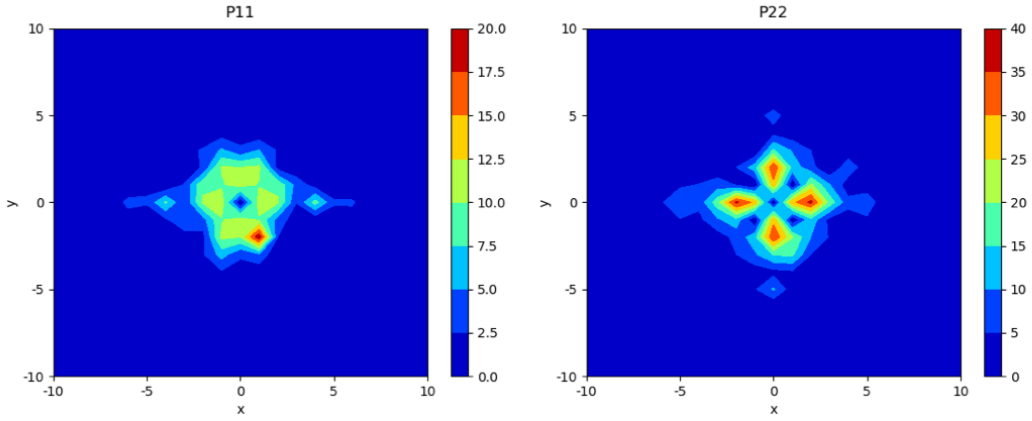

Strain of Final Microstructure	$(\eta - \eta_0)$	Strain of Initial Microstructure	Average P11 Error (%)	Average P22 Error (%)
30%	(30 – 20) = 10	20%	10.4	21.1

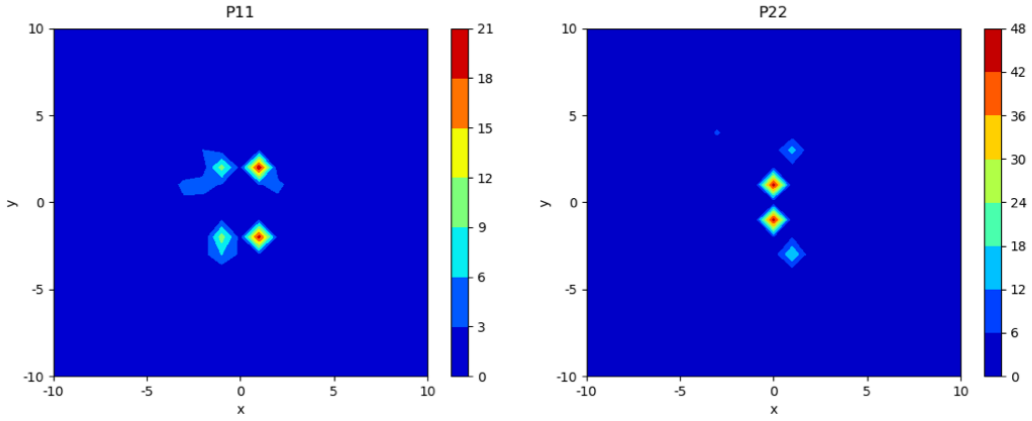

Strain of Final Microstructure	$(\eta - \eta_0)$	Strain of Initial Microstructure	Average P11 Error (%)	Average P22 Error (%)
30%	(30 – 10) = 20	10%	13.9	27.9

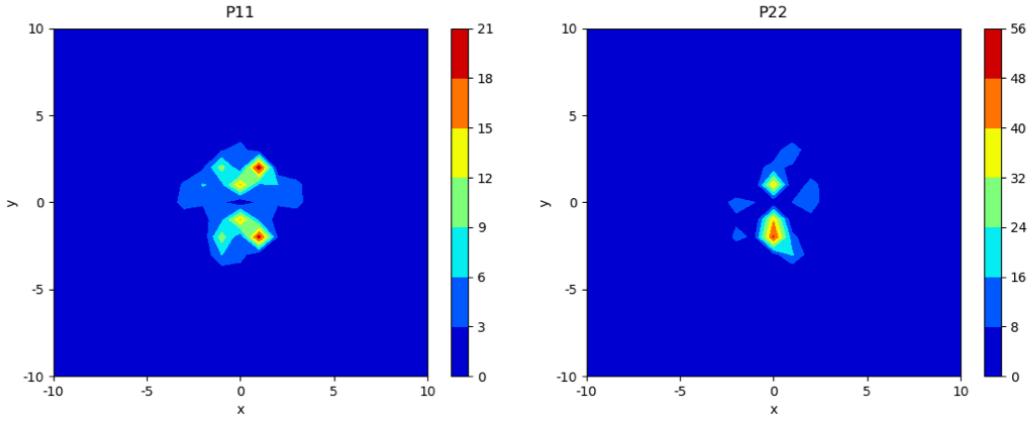

Strain of Final Microstructure	$(\eta - \eta_0)$	Strain of Initial Microstructure	Average P11 Error (%)	Average P22 Error (%)
30%	(30 – 0) = 30	0%	13.7	25.9

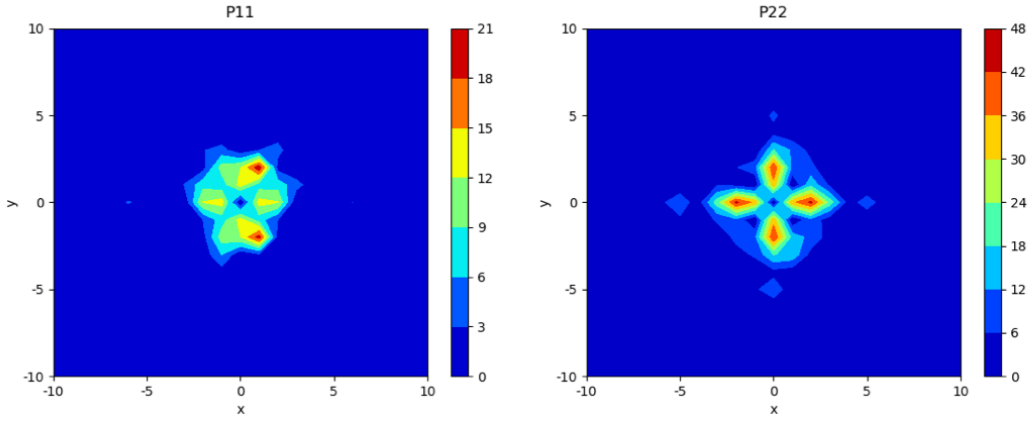

Strain of Final Microstructure	$(\eta - \eta_0)$	Strain of Initial Microstructure	Average P11 Error (%)	Average P22 Error (%)
20%	(20 – 10) = 10	10%	10.4	23.2

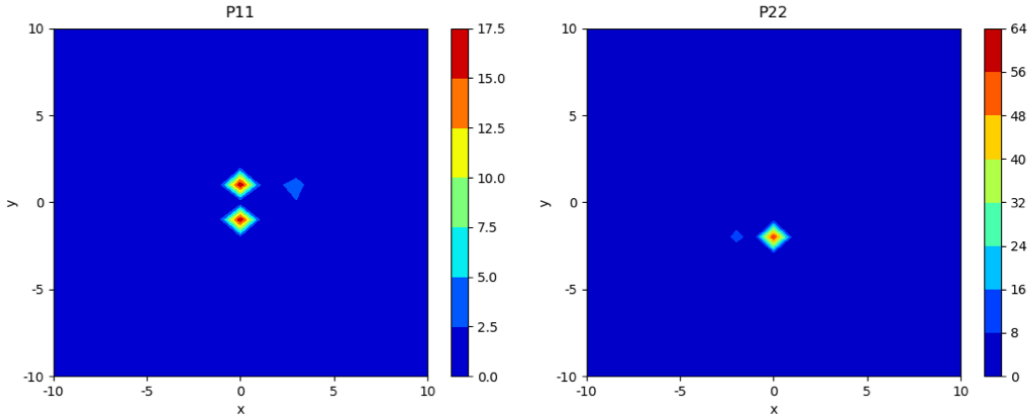

Strain of Final Microstructure	$(\eta - \eta_0)$	Strain of Initial Microstructure	Average P11 Error (%)	Average P22 Error (%)
20%	$(20 - 0) = 20$	0%	12.9	26.4

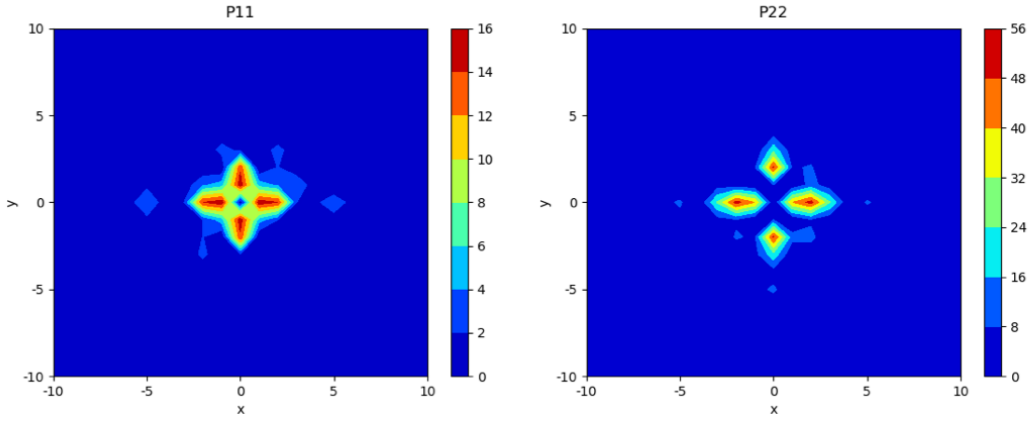

Strain of Final Microstructure	$(\eta - \eta_0)$	Strain of Initial Microstructure	Average P11 Error (%)	Average P22 Error (%)
10%	$(10 - 0) = 10$	0%	10.1	25.9

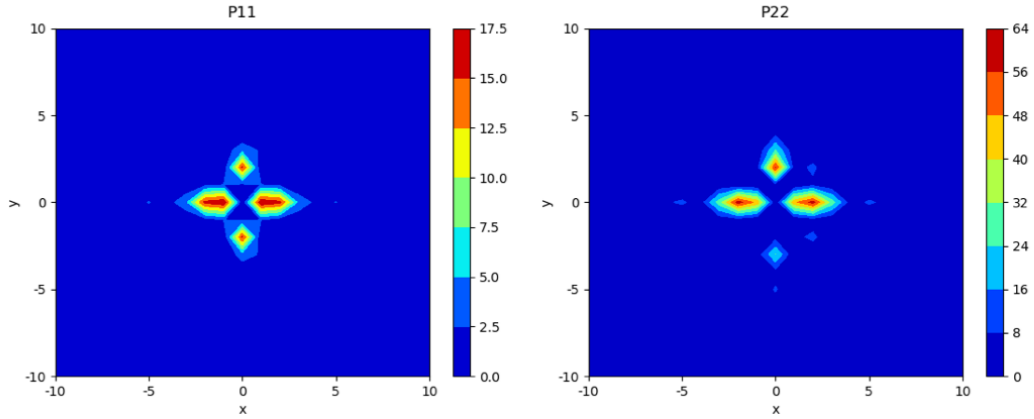

REFERENCES

[1] Wright, S. A., S. J. Plimpton, T. P. Swiler. "Potts-model Grain Growth Simulations: Parallel Algorithms and Applications". United States: N. p., 1997.

[2] Fanfoni, M., M. Tomellini. "The Johnson-Mehl-Avrami-Kolmogorov Model: A Brief Review". *Il Nuovo Cimento D* 20.7-8 (1998): 1171-1182.

[3] Molinari, A., G. R. Canova, S. Ahzi. "A Self-Consistent Approach of the Large Deformation Polycrystal Viscoplasticity". *Acta Metallurgica* 35.12 (1987): 2983-2994.

[4] Kalidindi, S. R., C. A. Bronkhorst, L. Anand. "Crystallographic Texture Evolution in Bulk Deformation Processing of FCC Metals". *Journal of Mechanics and Physics of Solids* 40.3 (1992): 537-569.

[5] Saito, Y. "Monte Carlo Simulation of Grain Growth in Three-Dimensions". *ISIJ International* 38.6 (1998): 559-566.

[6] Doherty, R. D., D. J. Srolovitz, A. D. Rollett, M. P. Anderson. "On the Volume Fraction Dependence of Particle Limited Grain Growth". United States: N. p., 1987.

[7] Zhang, J., F. Liou, W. Seutzer, K. Taminger. "A Coupled Finite Element Cellular Automaton Model to Predict Thermal History and Grain Morphology of Ti-6Al-4V During Direct Metal Deposition (DMD)". *Additive Manufacturing* 11 (2016): 32-39.

[8] Bunge, H. J. "Texture Analysis in Material Science: Mathematical Methods". *Elsevier*, 2013.

[9] Kocks, U. F. "A Symmetric Set of Euler Angles and Oblique Orientation Space Sections". No. LA-UR-88-5; CONF-8709172-4. Los Alamos National Lab, NM, 1987.

[10] Roe, R. J. "Description of Crystallite Orientation in Polycrystalline Materials. III. General Solution to Pole Figure Inversion" *Journal of Applied Physics* 36.6 (1965): 2024-2031.

[11] Torquato, S. “Random Heterogeneous Materials: Microstructure and Macroscopic Properties” *Springer-Verlag*, New York, NY, 2002.

[12] Corson, P. B. “Correlation Functions for Predicting Properties of Heterogeneous Materials. I. Experimental Measurement of Spatial Correlation Functions in Multiphase Solids”. *Journal of Applied Physics* 45.7 (1974): 3159-3164.

[13] Corson, P. B. “Correlation Functions for Predicting Properties of Heterogeneous Materials. II. Empirical Construction of Spatial Correlation Functions for Two-Phase Solids” *Journal of Applied Physics* 45.7 (1974): 3165-3170.

[14] Kristo, M. J., A. M. Gaffney, N. Marks, K. Knight, W. S. Cassata, I. D. Hutcheon. “Nuclear Forensic Science: Analysis of Nuclear Material Out of Regulatory Control” *Annual Review of Earth & Plenary Sciences* 44 (2016): 555-579.

[15] Nomura, N., Y. Tanaka, R. Kondo, H. Doi, Y. Tsutsumi, T. Hanawa. “Effects of Phase Constitution of ZrNb Alloys on their Magnetic Susceptibilities”. *Materials Transactions* 50.10 (2009): 2466-2472.

[16] Zhou, F. Y., B. L. Wang, K. J. Qiu, W. J. Lin, L. Li, Y. B. Wang, Y. F. Zheng. “Microstructure Corrosion Behavior and Cytotoxicity of Zr-Nb Alloys for Biomedical Application” *Materials Science and Engineering: C* 32.4 (2012): 851-857.

[17] Nie, L., Y. Zhan, T. Hu, X. Chen, C. Wang. “β-Type Zr-Nb-Ti Biomedical Materials with High Plasticity and Low Modulus for Hard Tissue Replacements”. *Journal of Mechanical Behavior of Biomedical Materials* 29 (2014): 1-6.

[18] Choo, K. N., Y. H. Kang, S. I. Pyun, V. F. Urbanic. “Effect of Composition and Heat Treatment on the Microstructure and Corrosion Behavior of ZrNb Alloys”. *Journal of Nuclear Materials* 209.3 (1994):226-235.

[19] Stukalov, A. I., V. M. Gritsina, T. P. Chernyaeva, D. A. Baturevich. “Mechanical and Corrosion Characteristics of Zr+2.5%Nb Zirconium Reactor Alloy”. *Materials Science* 36.5 (2000): 669-674.

[20] Nikulina, A. V. “Zirconium-Niobium Alloys for Core Elements of Pressurized Water Reactors”. *Metal Science and Heat Treatment* 45.7-8 (2003): 287-292.

[21] Abriata, J. P., J. C. Bolcich. "The Nb-Zr (niobium-zirconium) System". *Journal of Phase Equilibria* 3.1 (1982)L 34-44.

[22] Koike, J., M. E. Kassner, R. E. Tate, R. S. Rosen, "The Nb-U (niobium-uranium) System" *Journal of Phase Equilibria* 19.3 (1998): 253-260.

[23] Finlayson, M. J. "Isothermal Transformations in Eutectoid Zirconium-Niobium Alloy". *Dissertation.* University of British Columbia, 1957.

[24] Stewart, D., B. A. Hatt, J. A. Roberts. "High-speed Thermal Analysis of ZrNb Alloys". *British Journal of Applied Physics* 16.8 (1965): 1081.

[25] Sikka, S. K., Y. K. Vohra, R. Chidambaram. "Omega Phase in Materials". *Progress in Materials Science* 27.3-4 (1982): 245-310.

[26] Strumal, B. B., A. S. Gornakova, A. A. Mazilkin, O. B. Fabrichnaya, M. J. Kriegel, B. Baretzky, J. Z. Jiang, S. V. Dobatkin, "Phase-Transformations in the Severely Plastically Deformed Zr-Nb Alloys". *Materials Letters* 81 (2012): 225-228.

[27] Dave, T. "Effect of Hot Rolling and Intermittent Annealing on the Texture Evolution of Monotectoid BCC Zr-Nb". *Dissertation*. Georgia Institute of Technology, 2017.

[28] Bachmann, F., R. Hielscher, H. Schaeben. "Texture Analysis with MTEX-free and Open Source Software Toolbox". *Solid State Phenomena* Vol. 160, Trans Tech Publications Ltd, 2010.

[29] Clement, A., P. Coulomb. "Eulerian Simulation of Deformation Textures". *Scripta Metallurgica* 13.9 (1979): 899-901.

[30] Bunge, H. J., C. Elsing. "Texture Development by Plastic Deformation". *Scripta Metallurgica* 18.3 (1984): 191-195.

[31] Li, D. S., H. Garmestani, B. L. Adams. "A Texture Evolution Model in Cubic-Orthotropic Polycrystalline System". *International Journal of Plasticity* 21.8 (2005): 1591-1617.

[32] Li, D. S., H. Garmestani, S. Schoenfeld. "Evolution of Crystal Orientation Distribution Coefficients During Plastic Deformation". *Scripta Materialia* 49.9 (2003): 867-872.

[33] Li, D. S., J. Bouhattate, H. Garmestani. “Processing Path Model to Describe Texture Evolution During Mechanical Processing”. *Materials Science Forum* Vol. 495, Trans Tech Publications Ltd, 2005.

[34] Li, D. S., H. Garmestani, S. Ahzi. “Processing Path Optimization to Achieve Desired Texture in Polycrystalline Materials”. *Acta Materialia* 55.2 (2007): 647-654.

[35] Bouhattate, J., D. S. Li, G. A. C. Branco, C. M. Bacaltchuk, H. Garmestani. “Texture Prediction of Cold- and Hot-Rolled Titanium Using Processing Path Model”. *Journal of Materials Engineering and Performance* 20.2 (2011): 177-184.

[36] Tabei, A., D. S. Li, H. Garmestani, S. Y. Liang. “Derivation of Process Path Functions in Machining of Al Alloy 7075”. *Journal of Materials Engineering and Performance* 24.11 (2015): 4503-4509.

[37] Startt, J., T. Dave, E. Hoar, H. Garmestani, C. Deo. “Texture Evolution in BCC Zr-Nb at the Monotectoid Composition During Hot-Rolling and Annealing”. *Materialia*, 2020. Submitted.

[38] Matthies, S., H.-R. Wenk, G. W. Vinel. “Some Basic Concepts of Texture Analysis and Comparison of Three-Methods to Calculate Orientation Distributions from Pole Figures”. *Journal of Applied Crystallography* 21.4 (1998)L 285-304.

[39] Leyens, C., M. Peters. “Titanium and Titanium Alloys: Fundamentals and Applications”. *John Wiley & Sons*, 2003.

[40] Lütjering, G., J. C. Williams. “Titanium”. *Springer Science & Business Media*, 2007.

[41] Banerjee, D., J. C. Williams. “Perspectives on Titanium Science and Technology”. *Acta Materialia* 61.3 (2013): 844-879.

[42] Lütjering, G. “Influence of Processing on Microstructure and Mechanical Properties of (α+β) Titanium Alloys”. *Materials Science and Engineering A* 243.1-2 (1998): 32-45.

[43] Lütjering, G. “Property Optimization through Microstructural Control in Titanium and Aluminum Alloys”. *Materials Science and Engineering A* 263.2 (1999): 117-126.

[44] Roy, S., S. Suwas. "Microstructure and Texture Evolution During Sub-Transus Thermo-Mechanical Processing of Ti-6Al-4V-0.1B Alloy: Part I. Hot Rolling in (α+β) Phase Field". *Metallurgical and Materials Transactions A* 44.7 (2013): 3303-3321.

[45] Roy, S., S. Karanth, S. Suwas. "Microstructure and Texture Evolution During Sub-Transus Thermo-Mechanical Processing of Ti-6Al-4V-0.1B Alloy: Part II. Static Annealing in (α+β) Regime". *Metallurgical and Materials Transactions A* 44.7 (2013): 3332-3336.

[46] Roy, S., S. Suwas, S. Tamiriskandala, D. B. Miracle, R. Srinivasan. "Development of Solidification Microstructure in Boron-Modified Alloy Ti-6Al-4V-0.1B". *Acta Materialia* 59.14 (2011): 5494-5510.

[47] Roy, S., S. Suwas. "Crystallographic Texture and Microstructure Evolution During Hot Compression of Ti-6Al-4V-0.1B Alloy in the (α+β) Regime". *Philosophical Magazine* 94.4 (2014): 358-380.

[48] Roy, S., S. Suwas. "The Influence of Temperature and Strain Rate on the Deformation Response and Microstructure Evolution During Hot Compression of a Titanium Alloy Ti-6Al-4V-0.1B". *Journal of Alloys and Compounds* 548 (2013):110-125.

[49] Roy, S., A. Sakar, S. Suwas. "On Characterization of Deformation Microstructure in Boron Modified Ti-6Al-4V Alloy". *Materials Science and Engineering A* 528.1 (2010): 449-528.

[50] Roy, S., S. Suwas. "On the Absence of Shear Cracking and Grain Boundary Cavitation in Secondary Tensile Regions of Ti-6Al-4V-0.1B Alloy During Hot (α+β)-Compression". *Philosophical Magazine* 94.5 (2014): 447-463.

[51] Roy, S., S. Suwas, S. Tamirisakandala, R. Srinivasan, D. B. Miracle. "Processing Response of Boron Modified Ti-6Al-4V Alloy in (α+β) Working Regime". *TMS Annual Meeting*, San Francisco, CA (2009): 63-70.

[52] Garmestani, H., S. Lin, B. L. Adams. "Statistical Continuum Theory for Inelastic Behavior of a Two-Phase Medium". *International Journal of Plasticity* 14.8 (1998): 719-731.

[53] Hutchinson, J. W. “Bounds and Self-Consistent Estimates for Creep of Polycrystalline Materials”. *Proceedings of the Royal Society of London A. Mathematical and Physical Sciences* 348.1652 (1976): 101-127.

[54] Wheeler, D., D. Brough, T. Fast, S. Kalidindi. “PYMKS: Materials Knowledge System in Python”. *Figshare* 10 (2014): m9.

[55] Lin, S., H. Garmestani, B. Adams. “The Evolution of Probability Functions in an Inelasticly Deforming Two-Phase Medium”. *International Journal of Solids and Structures* 37.3 (2000): 423-434.

[56] Adams. B. L., A. Henrie, B. Henrie, M. Lyon, S. R. Kalidindi, H. Garmestani. “Microstructure-sensitive Design of a Compliant Beam”. *Journal of the Mechanics and Physics of Solids* 49.7 (2001): 1639-1663.

[57] Kalidindi, S. R., J. R. Houskamp, M. Lyons, B. L. Adams. “Microstructure Sensitive Design of an Orthotropic Plate Subjected to Tensile Load”. *International Journal of Plasticity* 20.8-9 (2011): 1561-1575.

[58] Fullwood, D. T., S. R. Niezgoda, B. L. Adams, S. R. Kalidindi. “Microstructure Sensitive Design for Performance Optimization”. *Progress in Materials Science* 55.6 (2010): 477-562.

[59] Seshacharyulu, T., S. C. Medeiros, W. G. Fraizer, Y. V. R. K. Prasad. “Hot Working of Commercial Ti-6Al-4V with and Equiaxed α-β Microstructure: Materials Modeling Considerations”. *Materials Science and Engineering A* 284.1-2 (2000): 184-194.